University of Southampton

Faculty of Engineering and Physical Sciences

Zepler Institute for Photonics and Nanoelectronics

Optoelectronics Research Centre

Fibre Raman Amplification of Bessel and Orbital Angular Momentum Higher Order Modes in Step Index Fibres

by

Sheng Zhu

ORCID ID 0000-0002-4256-6307

Thesis for the degree of Doctor of Philosophy

March 2021

University of Southampton

<u>Abstract</u>

Faculty of Engineering and Physical Sciences

Zepler Institute for Photonics and Nanoelectronics

Optoelectronics Research Centre

Thesis for the degree of <u>Doctor of Philosophy</u>

Fibre Raman Amplification of Bessel and Orbital Angular Momentum Higher Order

Modes in Step Index Fibres

by

Sheng Zhu

Large mode area (LMA) has been a cornerstone of high power fibre amplifiers and lasers thanks to the power scaling capability without exceeding the intensity threshold for nonlinear effects and optical damage. Many applications require single-mode operation, and conventionally, these fibres are designed to operate with the fundamental mode. Alternatively, a single higher order mode (HOM) with the intensity distribution of a zeroth order Bessel function LP_{0m} (usually $m \geq 4$) can propagate stably in a highly multimode step-index fibre. These HOMs are also reported to be more resistant to bending induced distortions and mode coupling than the fundamental mode. Fibre amplifiers for these modes may have higher mode area scaling capability and can then offer higher power threshold for nonlinearities. So far, rare-earth (RE) doped fibre amplifiers for these HOMs have been demonstrated, while fibre Raman amplifiers (FRAs) for such modes have not been reported prior to my thesis work. FRAs are unique in that they are wavelength agile. More importantly for my thesis work, they may preserve the target HOM better than a RE-doped fibre amplifier does thanks to not only better control of fibre perturbations, but also to the absence of local gain saturation. Additionally, FRAs for HOMs can be better than cladding pumped FRAs in that they fulfil the area ratio requirement for efficient first order Stokes conversion while allowing stable single mode operation.

This thesis is dedicated to the demonstration of the mode preservation and brightness enhancement capability of FRAs for HOMs. I start with investigations of signal mode purity degradation via numerical simulations and compare the performance of typical Yb-doped fibre amplifiers (YDFAs) and FRAs both with the same HOM. Results show that the mode purity is preserved better in the FRA than in the YDFA for incoherent signal and pump. My experimental demonstrations are restricted to FRAs and start with pulsed Raman amplification of a single HOM in large core step index fibres with lengths of ~10 m. The signal output sees 18 dB gain and is ~14 dB brighter in terms of maximum power in a single mode than the launched multimode pump, with good mode purity preservation and weighted conversion efficiency. Then a pulsed FRA in 335 m of large core step index fibre is demonstrated with over 23 dB amplification to the signal and ~16 dB brightness enhancement from the launched pump. The purity degradation is modest and is likely to be the result of the emergence of 2nd order Stokes. The low pump brightness also points towards direct diode laser pumping, which I attempted with an 877-m large core step index fibre and spectrally combined pumping from five diode lasers. A 6 dB Raman gain of the signal is achieved with quasi-CW pump with ~170 W combined peak power, which is expected to be improved with further optimizations. These results successfully demonstrate the capability and potential of power scaling and brightness enhancement of FRAs with HOMs.

The advantages of FRAs are also utilized with fibre modes carrying orbital angular momentum (OAM). These OAM modes (OAMM) can be viewed as pairs of spatially coherent degenerate modes, in which the angular momentum improves the stability to some perturbations. Although in this case, the saturation of RE-doped fibre amplifiers may aid in suppressing the growth of degenerate parasitic modes, notably those of conjugate charges, FRAs are still preserving the target OAMM well, which is evident by the experimental results presented in the thesis. I first describe a pulsed FRA for a charge-2 OAMM in a 5-m multimode step index fibre with 15 dB maximum gain with an amplified

signal mode purity of 83.2% dropping from 95.8% when unamplified. The purity degradation is attributed to coupling into the conjugate charge which I expect to decrease for higher charges. The subsequent experiment of Raman amplification of a charge-15 OAMM in a 30-m large core step index fibre confirms this. The signal gain reached 9.2 dB, with only modest purity degradation from 84.3% to 78.4% and negligible coupling into the conjugate charges.

The results of both HOMs and OAMMs have proven the feasibility of FRAs for power scaling of these modes with great signal mode preservation, making FRAs an attractive alternative to RE-doped fibre amplifiers.

Table of Contents

Table of Contents

Table of Tables

Table of Figures

Table of Figures

Table of Figures

List of Accompanying Materials

Data reported in this thesis are available from the University of Southampton at https://doi.org/10.5258/SOTON/D1912.

Research Thesis: Declaration of Authorship

Print name: Sheng Zhu

Title of thesis: Fibre Raman Amplification of Bessel and Orbital Angular Momentum Higher Order Modes in Step Index Fibres

I declare that this thesis and the work presented in it are my own and has been generated by me as the result of my own original research.

I confirm that:

1. This work was done wholly or mainly while in candidature for a research degree at this University;
2. Where any part of this thesis has previously been submitted for a degree or any other qualification at this University or any other institution, this has been clearly stated;
3. Where I have consulted the published work of others, this is always clearly attributed;
4. Where I have quoted from the work of others, the source is always given. With the exception of such quotations, this thesis is entirely my own work;
5. I have acknowledged all main sources of help;
6. Where the thesis is based on work done by myself jointly with others, I have made clear exactly what was done by others and what I have contributed myself;
7. Parts of this work have been published in the journal and conference publications listed in Appendix A.

Signature: ....Date:...........................

Acknowledgements

First and foremost, I would like to take this opportunity to thank my supervisor Prof. Johan Nilsson. I have learned a lot not only from his profound knowledge in fibre optics but also his diligence, rigorous scholarship, and most importantly critical thinking. This thesis would not have been possible without his continuous support both inside and outside the labs as well as his patience and confidence in me throughout my years here at Southampton.

I would also like to express my sincere gratitude to my co-supervisor, Dr. Jonathan Price, who is sadly no longer with us. He has been both a great tutor and kind friend to me back when I just started my postgraduate study. He will always be remembered for his gentle but inspiring words whenever I sought help from him.

I am also extremely grateful to meet my fellow colleagues in the High Power Fibre Lasers group, past and present. Special thanks to Dr. Yutong Feng for his help and support in my research as well as being a thoughtful friend. Thanks to Dr. Shankar Pidishety for his help and input in my various experiments. Thanks to Dr. Christophe Codemard for helpful discussions and generous component loans. Thanks to other group members Dr. Huaiqin Lin, Mr. Soonki Hong, Dr. Pablo Hernández, Dr. Yujun Feng, Ms. Dan Cheng, Dr. Zhimeng Huang, Dr. Betty Zhang and Dr. Harish Achar Vasant for their assistance and enlightening discussions.

Many thanks to the collaborators inside and outside the ORC. I am grateful to Dr. Pranabesh Barua from ORC, Dr. Raghuraman Sidharthan and Prof. Seongwoo Yoo from Nanyang Technological University for fabricating the fibres. Thanks to Dr. Jeff Demas and Prof. Siddharth Ramachandran from Boston University for teaching me their first-hand experience with the higher order modes. Thanks to Prof. Balaji Srinivasan and Dr. Srinivas Pachava from Indian Institute of Technology Madras for their indispensable help on the experiments.

My thanks also go to my friends here in Southampton for their care and accompany throughout my life as a postgraduate, to name a few, Qiang, Zijian, Hao, Zhengqi, Meijing, Meng, Shaoxiang and many more.

I would like to acknowledge the University of Southampton and the China Scholarship Council for their financial support. Thanks again to Prof. Nilsson for kindly sponsoring me for the last few months of my PhD candidature.

Finally, I would like to thank my parents for their endless love and care, for their faith in me that helped me through the most challenging time. Also, thanks to my dear Zhengli for patiently waiting for me and pressing me to become a better person. My life here as a PhD student is coming to an end, but what I have learnt here from the masterminds will continue to guide me for years to come.

Definitions and Abbreviations

AFG	Arbitrary function generator
AOM	Acousto-optic modulator
APC	Angled physical contact
AWG	Arbitrary waveform generator
BPM	Beam propagation method
BPP	Beam parameter product
CGH	Computer generated hologram
CLS	Cladding light stripper
CW	Continuous wave
DCRF	Double clad Raman fibre
DDG	Digital delay generator
DL	Diode laser
DM	Dichroic mirror
FBG	Fibre Bragg grating
FRA	Fibre Raman amplifier
FWHM	Full width at half maximum
GRIN	Graded-index
HOM	Higher order mode
HR	High reflection
HT	High transmission
HWP	Half-waveplate
LCOS	Liquid crystal on silicon
LG	Laguerre Gaussian (mode)
LMA	Large mode area
LP	Linearly polarized (mode)
LPG	Long period grating
MOPA	Master oscillator power amplifier
NA	Numerical aperture
NDF	Neodymium doped fibre
NDFA	Neodymium doped fibre amplifier

Definitions and Abbreviations

OAM	Orbital angular momentum
OAMM	Orbital angular momentum mode
ORC	Optoelectronics Research Centre
OSA	Optical spectrum analyser
PC	Polarization controller
PI	Polarization insensitive
QCW	Quasi-continuous-wave
QWP	Quarter-waveplate
RE	Rare earth
RGF	Raman gain fibre
SAM	Spin angular momentum
SLM	Spatial light modulator
SPM	Self-phase modulation
SOa	Spin-orbit aligned
SOaa	Spin-orbit anti-aligned
SRS	Stimulated Raman scattering
TE	Transverse electric (mode)
TFB	Tapered fibre bundle
TM	Transverse magnetic (mode)
TMI	Transverse mode instability
UV	Ultraviolet
WDM	Wavelength division multiplexer/multiplexing
YDF	Ytterbium doped fibre
YDFA	Ytterbium doped fibre amplifier
YDFL	Ytterbium doped fibre laser

Chapter 1   Introductions

In this chapter I motivate my research presented in this thesis and outline the contents. I start with a brief introduction of high power rare-earth doped fibre amplifiers and Raman amplifiers that primarily operate with the fundamental mode. Then I discuss the advantages of using higher-order modes and the unique attractions of fibre Raman amplifiers for these HOMs as well as the fibre modes carrying orbital angular momentum. Then, I outline the structure of this thesis in section 1.2. Finally, the contributions and acknowledgements are listed chapter by chapter in section 1.3.

1.1   Fibre amplifiers with large mode area

Fibre lasers and amplifiers see tremendous uses in material processing, defence, communications and many more applications [1]. The unique geometry of optical fibres with scalable length allows tight confinement of light which enables efficient conversion from a low brightness pump to a higher brightness signal output. Flexible and precise control of the signal can also be achieved with the master oscillator power amplifier (MOPA) configuration in both pulsed and continuous-wave (CW) regimes. Many of the latest high power fibre sources comprise a low or medium power master oscillator and one or more power amplifiers that boost the output by several orders of magnitudes. The tight confinement of light, however, can introduce detrimental effects at high power such as fibre damages and nonlinearities. These effects are proportional to the power density of light and in general, by increasing the mode area, it is possible to go to higher power without exceeding the threshold for nonlinearities and damages. Since many of the applications benefit from a single mode output where the brightness is maximized and conventionally the fundamental mode is used, a variety of LMA fibres have been proposed and demonstrated to allow for stable fundamental-mode operation in single-mode as well as multimode fibre waveguides. Some designs reduce the refractive index contrast between the core and cladding to minimize the number of modes supported in the fibre [2, 3]. Multimode fibres can also be used to stably propagate the fundamental mode over lengths of tens of meters for either ultrashort pulses [4] or by selective doping [5]. One can also selectively remove the higher order mode content in the fibre by using leakage channel fibres which leak out the HOMs through the air holes surrounding the core [6] or couple the HOMs into a leaky mode via resonant coupling in a trench fibre [7]. There are also microstructured fibres such as photonic crystal fibres where light is trapped in the core by a 2D photonic bandgap instead of total internal reflections [8]. These approaches are able to scale the mode area to 500~3000 μm^2. Recently, transverse mode instabilities (TMI) have shifted the interest from pursuing fibres with ultra-large mode area, notably in the regime of high average power where thermal effects lead to TMI [9]. Nevertheless, in other regimes, it is still attractive to explore options to scale the mode area to increase thresholds for nonlinearities while maintaining a single mode output.

A single HOM, counterintuitive as it may seem, can propagate stably in a multimode step-index fibre, and serves as a novel alternative for scaling of the core size and thus the mode area. Generally, a LP_{0m} mode with high radial order (usually $m \geq 4$), is reported to be more resistant to mode coupling and distortions induced by bending or microbends in the fibre than the fundamental mode, with the resistance scaling with the radial order m [10, 11]. This is due to the increased effective index separation of the HOM from its nearest neighbour antisymmetric LP_{1m} mode compared to the fundamental mode in a large mode area fibre. The simple step-index design allows significant mode area scaling potential without sophisticated and perturbation-prone fibre fabrication, and fibre amplifiers for HOMs with mode area of 6000 μm^2 have already been demonstrated [12]. These HOMs can be readily excited in fibre with free-space Bessel beams generated by optics such as axicons [13] or a spatial light modulator (SLM) [14], or converted in fibre from the fundamental mode with long period gratings (LPGs) [15]. The reciprocity of the devices allow conversion from the HOM or output Bessel beam back to the fundamental mode. The Bessel beam itself also can also be applied in fields like material processing [16], imaging [17] and nanoparticle manipulations [18].

Rare-earth (RE) doped fibre amplifiers for these HOMs with either cladding pumping [19] or core pumping [20] have been demonstrated. For cladding pumping, conventional multimode pump sources such as diode lasers (DLs) can be used, allowing brightness enhancement from the pump to the signal. For core pumping, in the reported demonstrations, the pump beam was converted to the same HOM as the signal mode which ensures high pump-signal overlap and conversion efficiency. In both cases, the gain fibres were designed to have a smaller inner core where the central peak of the higher order LP_{0m} resides and a large outer core where the entire HOM is guided. Both the inner and outer core were doped. The pump beam was guided in the round outer core which had a diameter of 80 to 100 μm. This allowed efficient conversion from the fundamental mode which was guided in the core to the HOM by the LPG. Later, an Yb-doped fibre amplifier (YDFA) for a HOM with the pump guided in the octagonal outer cladding was reported [21]. This provides higher potential for brightness enhancement.

The use of RE gain for HOM amplification is not without challenges and limitations. One is that if the core is doped throughout, the region with dopants spans across 50~100 μm in diameter, and the refractive index profile, if not controlled precisely, can be easily perturbed, introducing distortions to the target HOM and extra mode coupling. The spontaneous emission in the large number of supported modes can also reduce the efficiency and the signal mode purity if not suppressed [21]. Another concern is the mode selective gain saturation, where the parasitic modes need to be weak and thus suffer less from the compression of the gain by the target mode, which carries more power. Therefore, the parasitic modes can have much higher gain than the target signal mode, leading to degraded mode purity. This happens even without pump depletion. In comparison, fibre Raman amplifiers (FRAs) offer important attractions over RE-doped fibre amplifiers both practically and conceptually. A practical advantage is the ubiquitous gain media with low cost and simple and precise

control of refractive index profile that introduces less distortions and scattering, e.g., to a targeted HOM in a multimode step-index fibre. The conceptual advantage is that the local gain in Raman amplifiers is independent from the local signal intensity and therefore the gain saturation is not mode selective unless the pump intensity distribution has been significantly altered due to depletion. The unsaturated gain for non-degenerate parasitic modes is also less prominent in the Raman amplifier. As it comes to degenerate modes, it is in many cases possible to avoid having parasitic modes degenerate with the target mode (the conjugate mode of a targeted OAMM is an important exception). Hence, the gain saturation may degrade the signal mode purity much less than in RE-doped fibre amplifiers. Furthermore, the Raman gain, being wavelength agile, can utilize pump from not only high-power diode lasers but also other fibre lasers and amplifiers, allowing power scaling in a much broader spectral range.

A FRA for a HOM also offers advantages over conventional cladding pumped FRAs. The cladding/core area ratio is limited to ~8 for the double cladding Raman fibres (DCRFs) to suppress Raman conversion into 2nd order Stokes and thus enable efficient conversion to the 1st Stokes [22]. The core normally needs to be much smaller than typical cladding sizes to maintain stable fundamental mode propagation. This limits the cladding to smaller sizes than normal and puts an upper limit to the degree of brightness enhancement achievable with DCRFs. In 2020, a cladding pumped FRA reached ~763 W CW output power with brightness enhancement [23]. The instantaneous power is also limited to a narrow range to allow efficient conversion into first order Stokes when the area ratio is close to the limit of ~8 [22]. This is a problem for pulsed FRAs because of significant variations in instantaneous power during a pulse. To the best of my knowledge, the record output peak power from a nanosecond pulsed double-clad FRA with brightness enhancement is ~2.8 kW reported in 2009 [24]. Instead, the cladding to core area ratio for the core pumped FRA is effectively the ratio of mode area between pump and signal beam, which is less than four for the experimental configurations presented in this thesis. Therefore, the area ratio requirement is readily fulfilled with FRAs for HOM, which allows for brightness enhancement with efficient conversion into the 1st Stokes order with simple and low-cost fibres. Still, cladding-pumping of FRAs for HOMs is possible, but the potential seems quite limited and it has not been pursued by me.

Recently, fibre Raman lasers and amplifiers based on graded index (GRIN) fibres have achieved great success producing high power and high beam quality output at around 1 μm wavelength with pumping from diode lasers or Yb-doped fibre lasers (YDFLs) [25-27]. Chen *et al*. reported a record high 3-kW CW output power with brightness enhancement at 1130 nm from a GRIN fibre with metalized coating [28]. In GRIN fibres, a beam clean-up effect arises from the mode competition of stimulated Raman scattering (SRS) [29]. This effect, which is absent in step-index fibres, favours the lower order Stokes modes, especially the fundamental mode over the HOMs in that the lower order modes generally have better overlap with the pump modes and hence see higher gain in most of the simulated uniformly random pump mode distributions [30]. However, the margin in gain is relatively

small, especially between the fundamental mode and its nearest HOMs. Therefore, the Stokes beam need to have sufficient interaction with the pump beam to reach a high fraction of power in the fundamental mode. This is usually achieved in laser cavities where the signal propagates for multiple roundtrips. In single pass amplifiers, the beam clean-up effect performs less well. On top of that, the reported fibre output is not truly single mode. In comparison, FRAs for HOM allow for single mode amplification with low mode coupling even in long fibres.

In addition to the Bessel-like LP_{0m} modes (and the equivalent HE_{1m} modes), the hybrid vector modes with donut shaped intensity distributions can form optical vortices in fibre carrying orbital angular momentum (OAM). These vortex beams draw massive interests in research for their applications in imaging [31], classical [32] or quantum [33] communications, nanoparticle manipulation [34], etc. In analogy to the Bessel-like LP_{0m} modes, fibre modes carrying OAM (OAMMs) may also benefit from the advantages of FRAs such as the easier control of fibre perturbations, the non-local gain saturation, and the wavelength agility. The Raman gain fibre can be as simple as a multimode step index fibre or a slightly more complex fibre with a ring-shaped or air core. Also note that in the approximation of LP-modes, they too can form OAMMs. Thus, for example, the two LP_{11}-modes can form a charge-1 OAMM. However, as LP_{11} is in fact a superposition of weakly non-degenerate vector modes, neither LP_{11} nor the corresponding OAMMs are true modes. Therefore, in sufficiently long fibres, they will not be maintained even in the absence of mode-coupling. Nevertheless, in a short fibre, they can still be considered true modes, even though they are constructed from quasi-degenerate rather than degenerate modes.

Given all the benefits and advantages of HOMs in LMA fibres and their usage in FRAs, combined with the flexibility of fibre MOPAs, we believe FRAs are excellent for power scaling and brightness enhancement with HOMs, be it the LP_{0m} modes or the OAMMs, with high preservation of the signal mode purity. In my PhD studies I have built FRAs for both Bessel HOMs and OAMMs in multimode step-index fibres with multimode pumping and demonstrated their capabilities of power scaling and mode preservation. For the HOMs, I start with a pulsed FRA and explore in two directions: one is to achieve high peak power and high gain with high pump power depletion, the other is to lower the brightness requirement of the pump beam and attempt direct diode laser pumping of the FRA. For the OAMMs, the Raman gain was firstly applied to a low charge circularly polarized OAMM, whose properties have been relatively well examined by others, in a commercial step index fibre. Then I amplified a high charge linearly polarized OAMM in a large core step index fibre to explore the capability of the FRA in terms of mode preservation, especially considering the reduced coupling expected between the conjugate charges as the charge number increases.

1.2   Thesis Outline

This thesis is arranged in chapters as follows:

Chapter 1 introduces the motivations for my PhD research.

Chapter 2 presents a brief introduction to the higher order fibre modes including the Bessel HOMs as well as the hybrid vector modes that form the OAM modes. The factors that govern the coupling between modes under minor perturbations are briefly covered. I also present the background knowledge of stimulated Raman scattering in optical fibres and discuss the gain saturation effects in FRAs and briefly compare them with the YDFAs.

The simulation results aiming to investigate the difference in the gain saturation induced mode purity degradation between a typical FRA and a YDFA are described in Chapter 3. Two approaches covering the coherent and incoherent fibre amplifiers are used and the differences are discussed.

Chapter 4 details the experiments on Raman amplification of Bessel HOMs in a variety of configurations. I start with the first experimental setup utilizing a pulsed commercial YDFL as the master oscillator and discuss the experimental results. After that, two experiments based on FRAs with MOPA based pump and seed sources are described. The first one focuses on high Raman gain with high pump depletion while the second one verifies the possibility of stable HOM propagation in long fibres. Finally, a quasi- continuous-wave (QCW) FRA for HOM with spectrally combined diode laser pumping and its preliminary performance are discussed.

Chapter 5 presents the two experiments of Raman amplification of OAMMs in step-index fibres. The first one is with a charge 2 OAMM in a commercial step-index multimode fibre. The second one is with a charge 15 OAMM in a 70 μm diameter core step-index fibre. The modal contents of the transmitted and amplified signal are quantified with modal decomposition.

The conclusions and prospects of future work are discussed in Chapter 6.

1.3   Contributions and acknowledgements

The author is responsible for the work presented in this thesis under the supervision of Prof. Johan Nilsson and Dr. Jonathan Price.

The MATLAB code for incoherent simulations of FRA used in Chapter 2 was modified from the work of Mr. Soonki Hong. The code for coherent simulation with beam propagation method (BPM) in RP Fiber Power used in Chapter 2 was developed with the help of Dr. Yutong Feng.

The Yb-doped double-clad fibre in section 4.2 was designed and fabricated by Dr. Raghuraman Sidharthan and Prof. Seongwoo Yoo at the Nanyang Technological University.

The experimental setup of fibre Raman amplifiers in section 4.2 and section 5.2 is built with the help of Dr. Shankar Pidishety, Dr. Yutong Feng and Prof. Balaji Srinivasan. The techniques for alignment of optics for the excitation of HOMs is provided by Dr. Jeff Demas and Prof. Siddharth

Ramachandran from Boston University. The experimental setup in section 5.3 is built with the help of Dr. Srinivas Pachava who also provided codes for generating the holograms for the work.

The pump MOPA used in section 4.3, 4.4 and 5.2 is modified from the work of Dr. Yutong Feng.

The Raman gain fibres used in section 4.3, 4.4, 4.5 and 5.2 are pulled from a commercial preform (Fluosil Preform SWS6.95/SWU1.4, Heraeus) by Dr. Pranabesh Barua.

The multi-wavelength pump source in section 4.5 is the work of Mr. Soonki Hong.

1.4   References

[1]   D. J. Richardson, J. Nilsson, and W. A. Clarkson, "High power fiber lasers: current status and future perspectives [Invited]," J. Opt. Soc. Am. B **27**, B63 (2010).

[2]   Y. Jeong, J. K. Sahu, D. N. Payne, and J. Nilsson, "Ytterbium-doped large-core fiber laser with 1.36 kW continuous-wave output power," Opt. Express **12**, 6088 (2004).

[3]   D. Jain, Y. Jung, P. Barua, S. Alam, and J. K. Sahu, "Demonstration of ultra-low NA rare-earth doped step index fiber for applications in high power fiber lasers," Opt. Express **23**, 7407 (2015).

[4]   M. E. Fermann, "Single-mode excitation of multimode fibers with ultrashort pulses," Opt. Lett. **23**, 52 (1998).

[5]   N. G. R. Broderick, H. L. Offerhaus, D. J. Richardson, R. A. Sammut, J. Caplen, and L. Dong, "Large mode area fibers for high power applications," Opt. Fiber Technol. **5**, 185 (1999).

[6]   L. Dong, X. Peng, and J. Li, "Leakage channel optical fibers with large effective area," J. Opt. Soc. Am. B **24**, 1689 (2007).

[7]   D. Jain, Y. Jung, M. Nunez-Velazquez, and J. K. Sahu, "Extending single mode performance of all-solid large-mode-area single trench fiber," Opt. Express **22**, 31078 (2014).

[8]   R. F. Cregan, B. J. Mangan, J. C. Knight, T. A. Birks, P. S. J. Russell, P. J. Roberts, and D. C. Allan, "Single-mode photonic band gap guidance of light in air," Science **285**, 1537 (1999).

[9]   M. N. Zervas, "Transverse mode instability, thermal lensing and power scaling in Yb^{3+}-doped high-power fiber amplifiers," Opt. Express **27**, 19019 (2019).

[10]   S. Ramachandran, J. W. Nicholson, S. Ghalmi, M. F. Yan, P. Wisk, E. Monberg, and F. V. Dimarcello, "Light propagation with ultralarge modal areas in optical fibers," Opt. Lett. **31**, 1797 (2006).

[11]   J. M. Fini, and S. Ramachandran, "Natural bend-distortion immunity of higher-order-mode large-mode-area fibers," Opt. Lett. **32**, 748 (2007).

[12]   J. W. Nicholson, J. M. Fini, A. M. DeSantolo, X. Liu, K. Feder, P. S. Westbrook, V. R. Supradeepa, E. Monberg, F. DiMarcello, R. Ortiz, C. Headley, and D. J. DiGiovanni, "Scaling the effective area of higher-order-mode erbium-doped fiber amplifiers," Opt. Express **20**, 24575 (2012).

[13]   R. M. Herman, and T. A. Wiggins, "Production and uses of diffractionless beams," J. Opt. Soc. Am. A **8**, 932 (1991).

[14]   J. Demas, L. Rishøj, and S. Ramachandran, "Free-space beam shaping for precise control and conversion of modes in optical fiber," Opt. Express **23**, 28531 (2015).

[15]   S. Ramachandran, "Dispersion-tailored few-mode fibers: a versatile platform for in-fiber photonic devices," J. Lightwave Technol. **23**, 3426 (2005).

[16]   M. Duocastella, and C. B. Arnold, "Bessel and annular beams for materials processing," Laser & Photon. Rev. **6**, 607 (2012).

[17]   T. A. Planchon, L. Gao, D. E. Milkie, M. W. Davidson, J. A. Galbraith, C. G. Galbraith, and E. Betzig, "Rapid three-dimensional isotropic imaging of living cells using Bessel beam plane illumination," Nat. Methods **8**, 417 (2011).

[18]   K. Dholakia, and T. Čižmár, "Shaping the future of manipulation," Nat. Photonics **5**, 335 (2011).

[19]   S. Ramachandran, K. Brar, S. Ghalmi, K. Aiso, M. Yan, D. Trevor, J. Fleming, C. Headley, P. Wisk, and G. Zydzik, "High-power amplification in a 2040-μm^2 higher order mode," in *SPIE Photonics West* (2007).

[20]   J. W. Nicholson, J. M. Fini, A. M. DeSantolo, E. Monberg, F. DiMarcello, J. Fleming, C. Headley, D. J. DiGiovanni, S. Ghalmi, and S. Ramachandran, "A higher-order-mode Erbium-doped-fiber amplifier," Opt. Express **18**, 17651 (2010).

[21]   K. S. Abedin, R. Ahmad, A. M. DeSantolo, and D. J. DiGiovanni, "Reconversion of higher-order-mode (HOM) output from cladding-pumped hybrid Yb:HOM fiber amplifier," Opt. Express **27**, 8585 (2019).

[22]   J. Ji, C. A. Codemard, M. Ibsen, J. K. Sahu, and J. Nilsson, "Analysis of the conversion to the first Stokes in cladding-pumped fiber Raman amplifiers," IEEE J. Sel. Top. Quantum Electron. **15**, 129 (2009).

[23]   Y. Chen, T. Yao, H. Xiao, J. Leng, and P. Zhou, "High-power cladding pumped Raman fiber amplifier with a record beam quality," Opt. Lett. **45**, 2367 (2020).

[24]   A. K. Sridharan, J. E. Heebner, M. J. Messerly, J. W. Dawson, R. J. Beach, and C. P. J. Barty, "Brightness enhancement in a high-peak-power cladding-pumped Raman fiber amplifier," Opt. Lett. **34**, 2234 (2009).

[25]   Y. Glick, V. Fromzel, J. Zhang, N. Ter-Gabrielyan, and M. Dubinskii, "High-efficiency, 154 W CW, diode-pumped Raman fiber laser with brightness enhancement," Appl. Opt. **56**, B97 (2017).

[26]   S. I. Kablukov, E. I. Dontsova, E. A. Zlobina, I. N. Nemov, A. A. Vlasov, and S. A. Babin, "An LD-pumped Raman fiber laser operating below 1 μm," Laser Phys. Lett. **10**, 085103 (2013).

[27]   Y. Chen, J. Leng, H. Xiao, T. Yao, and P. Zhou, "Pure passive fiber enabled highly efficient Raman fiber amplifier with record kilowatt power," IEEE Access **7**, 28334 (2019).

[28]   Y. Chen, T. Yao, H. Xiao, J. Leng, and P. Zhou, "3 kW passive-gain-enabled metalized Raman fiber amplifier with brightness enhancement," J. Lightwave Technol. **39**, 1785 (2021).

[29]   K. S. Chiang, "Stimulated Raman scattering in a multimode optical fiber: evolution of modes in Stokes waves," Opt. Lett. **17**, 352 (1992).

[30]   N. B. Terry, T. G. Alley, and T. H. Russell, "An explanation of SRS beam cleanup in graded-index fibers and the absence of SRS beam cleanup in step-index fibers," Opt. Express **15**, 17509 (2007).

[31]   L. Yan, P. Gregg, E. Karimi, A. Rubano, L. Marrucci, R. Boyd, and S. Ramachandran, "Q-plate enabled spectrally diverse orbital-angular-momentum conversion for stimulated emission depletion microscopy," Optica **2**, 900 (2015).

[32]   A. E. Willner, H. Huang, Y. Yan, Y. Ren, N. Ahmed, G. Xie, C. Bao, L. Li, Y. Cao, Z. Zhao, J. Wang, M. P. J. Lavery, M. Tur, S. Ramachandran, A. F. Molisch, N. Ashrafi, and S. Ashrafi, "Optical communications using orbital angular momentum beams," Adv. Opt. Photon. **7**, 66 (2015).

[33]   M. Erhard, R. Fickler, M. Krenn, and A. Zeilinger, "Twisted photons: new quantum perspectives in high dimensions," Light Sci. Appl. **7**, 17146 (2018).

[34]   M. Padgett, and R. Bowman, "Tweezers with a twist," Nat. Photonics **5**, 343 (2011).

Chapter 2   Background

2.1   Introduction

In this chapter I briefly cover some of the background concepts related to fibre Raman amplification of higher order modes and orbital angular momentum modes. I first revisit the basics of light propagation in optical fibres and the characteristics of HOMs and OAMMs in terms of their formation, stability, and generation in section 2.2. Then I introduce stimulated Raman scattering and gain saturation in section 2.3.

2.2   Higher order modes in step-index fibres

2.2.1   Modes in step-index fibres
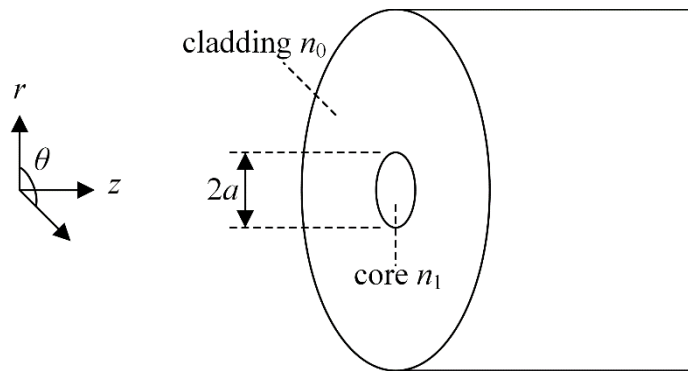
Figure 2.1: Illustration of the cross-section of a step-index fibre. The core diameter is $2a$. The refractive indices of the core and cladding are n_1 and n_0, respectively.

Light propagating in an optical fibre is described by Maxwell's equations with associated boundary conditions and can be expressed as a superposition of different transverse modes. These modes are the solutions of the wave equations with discrete propagation constants and are repeated after one wavelength. The detailed derivations of the solutions for the equations have already been covered in many textbooks [1-3] and are only briefly introduced here. The electric field in optical fibres (similar for the magnetic field **H**) which are longitudinally invariant are expressed in cylindrical coordinates as [1]:

$$\tilde{\mathbf{E}} = \mathbf{E}(r,\phi)e^{j(\omega t - \beta z)}.$$
$$(2.1)$$

Here r and ϕ denote the radial and azimuthal coordinates, ω is the angular optical frequency, and β is the propagation constant. In the cases I consider where there is no currents and charges in a homogeneous medium, any component of E, the transverse E_r, E_ϕ and the longitudinal E_z, satisfies the well-known Helmholtz equation:

$$\left(\nabla^2 + k^2 n^2\right)E = 0, \tag{2.2}$$

where k is the wave number in vacuum given by $k = 2\pi/\lambda$ and n is the refractive index of the fibre. In step-index fibres, n is everywhere constant, with different values in the core and in the cladding, as shown in Figure 2.1. We can then solve for the longitudinal component of the electric field E_z given by the wave equation:

$$\frac{\partial^2 E_z}{\partial r^2} + \frac{1}{r}\frac{\partial E_z}{\partial r} + \frac{1}{r^2}\frac{\partial^2 E_z}{\partial \phi^2} + \left(k^2 n_1^2 - \beta^2\right)E_z = 0 \text{ for } r \le a \text{, and} \tag{2.3}$$

$$\frac{\partial^2 E_z}{\partial r^2} + \frac{1}{r}\frac{\partial E_z}{\partial r} + \frac{1}{r^2}\frac{\partial^2 E_z}{\partial \phi^2} + \left(k^2 n_0^2 - \beta^2\right)E_z = 0 \text{ for } r > a. \tag{2.4}$$

By defining the normalized transverse wave numbers:

$$u = a\sqrt{k^2 n_1^2 - \beta^2}, \tag{2.5}$$

$$w = a\sqrt{\beta^2 - k^2 n_0^2}, \tag{2.6}$$

the solutions for the wave equations can be written as

$$E_z = AJ_q\left(ur/a\right)\sin\left(q\theta\right) \text{ for } r \le a \text{, and} \tag{2.7}$$

$$E_z = CK_q\left(wr/a\right)\sin\left(q\theta\right) \text{ for } r \ge a. \tag{2.8}$$

Here J_q and K_q are Bessel functions of the first and second kind, respectively. The other five components of the electromagnetic wave E_r, E_ϕ, H_z, H_r, H_ϕ can be derived from E_z using Maxwell's equations (this also requires knowledge of the relative magnetic permeability, which is normally assumed equal to unity). The integer q here takes a value of 0, 1, 2 and so on and denotes the azimuthal order. Another integer m denotes the different unique sets of u, w and β of the qth function as well as the radial mode order and takes a value of 1, 2, 3 and so on. The modes that correspond to the solutions with $E_z = 0$ or $H_z = 0$ are called the transverse electric (TE) modes (TE$_{0m}$) and transverse magnetic (TM) modes (TM$_{0m}$). Modes with non-zero E_z are labelled EH$_{qm}$ or HE$_{qm}$ and are referred to as the hybrid modes. The hybrid modes, together with the transverse modes that are derived from equations (2.3) and (2.4) are the so called vector modes.

The typical refractive index difference Δn between the core and cladding is rather small, of the order of ~1%. Therefore, it is often practical to assume $n_1/n_0 \approx 1$ in some of the expressions and simplify the solutions of the wave equations. Under this weakly guiding approximation, the electric and magnetic fields have negligible longitudinal components and are linearly polarized in the transverse plane. This set of solutions are designated as scalar modes or linearly polarized (LP) modes [4]. These LP modes are good approximations to the solutions of the vector wave equations (2.2) and their fields can be constructed with reasonable accuracy from linear combinations of vector modes.

Relations between the LP modes and the vector modes are presented in Table 2.1 [1] where l and m denote the azimuthal and radial order, respectively. Each of the LP modes with $l \geq 1$ is quadruply degenerate while each vector mode is doubly degenerate except for the TE and TM modes. Note that the intensity distributions of the LP_{1m} modes can be approximately constructed from combinations of either HE_{2m} and TE_{0m} or HE_{2m} and TM_{0m} depending on the polarization of the LP_{1m} mode.

Table 2.1: Comparison of linearly polarized modes and vector modes.

LP mode	Vector mode
LP_{0m} mode ($l = 0$)	HE_{1m} mode
LP_{1m} mode ($l = 1$)	TE_{0m} mode TM_{0m} mode HE_{2m} mode
LP_{lm} mode ($l \geq 2$)	$EH_{l-1,m}$ mode $HE_{l+1,m}$ mode

The lowest order mode HE_{11} (or the LP_{01} mode under the weakly guiding approximation) is referred to as the fundamental mode. In a multimode fibre, any mode other than the fundamental mode is then referred to as a higher order mode (HOM). The propagation constants β and effective indices n_{eff} of the HOMs, given by $n_{eff} = \beta/k$, are lower than for the fundamental mode. From a ray optics perspective, HOMs propagate with a larger angle to the fibre axis. In this thesis I focus on two particular types of HOMs, one is the LP_{0m} or HE_{1m} modes, specifically those with $m \geq 4$. These have transverse electric fields described by the zeroth order first kind Bessel function (J_0) and resemble truncated free-space Bessel beams. Unless specified, "HOM" in this thesis refers to these Bessel LP_{0m} modes. The other type is the hybrid modes $HE_{l+1,m}$ and $EH_{l-1,m}$ with $l \geq 1$ and $m = 1$ (thus corresponding to LP_{l1} in the weakly guiding linearly polarized approximation). These modes can form beams carrying orbital angular momentum (OAM) in optical fibres.

2.2.2   Mode coupling in fibres

In an unperturbed fibre, modes are orthogonal and do not exchange power with each other. In practice, there are always intrinsic fabrication imperfections such as fluctuations in the fibre refractive index or dimensions and external perturbations such as stress, strain or bending that cause fibre modes to couple. Practical fibres under minor perturbations are usually treated with coupled-mode theory, as introduced decades ago in many sources [2, 5]. In one of the approaches, under minor perturbations, the field of a perturbed fibre with arbitrary refractive index distribution $n = n(x, y, z)$ is described by a superposition of the modes from the ideal unperturbed fibre [6, 7]:

$$\mathbf{E} = \sum_{\mu=1}^{N} c_{\mu}(z)\mathbf{E}_{\mu}e^{i\beta_{\mu}z} \,, \tag{2.9}$$

where μ is the mode index, N is the total number of modes supported in the fibre and c_{μ} is the complex weight of the mode μ, $\mathbf{E}_{\mu}$ is the mode of an ideal fibre without perturbations. A deformation function $f(z)$ describes the perturbation, which is assumed to be separable, along the z direction. Then, the coupling coefficient between mode μ and v is given by:

$$\kappa_{\mu v} = \frac{\omega\varepsilon_0}{4i}\iint\left(n^2 - n_0^2\right)\mathbf{E}_{\mu}^{*}\cdot\mathbf{E}_{v}dA \tag{2.10}$$

and the evolution of mode weight c_{μ} for each of the N modes is

$$\frac{dc_{\mu}}{dz} = \sum_{v=1}^{N}\kappa_{\mu v}f(z)c_{v}(z)e^{i(\beta_{\mu}-\beta_{v})z} \tag{2.11}$$

Here ε_0 is the vacuum permittivity, and β_{μ} and β_{v} are mode propagation constants. In equation (2.11) for the evolution of mode weights, the oscillating factor $\exp\left(i\left(\beta_{\mu}-\beta_{v}\right)z\right)$ generally reduces the coupling between modes with large separation between the propagation constants. Note that the coupling is also related to the type of perturbation $f(z)$ in the fibre. One of the most common perturbations in fibres are bends which introduce phase perturbations [8]. Such a perturbation is odd in azimuthal phase and is able to couple modes of the same radial order but with neighbouring azimuthal order, such as $l = 0$ and $l = 1$ [7]. Stronger bends can also induce birefringence in the fibre via stress effects [9]. Other common perturbations include microbends leading to deformations of the refractive index profile and fluctuations in fibre dimensions, twists and so on. The microbends not only induce coupling between guided modes but also between guided and radiation modes, causing extra loss in the fibre [10].

2.2.3   Bessel-like higher order modes in multimode fibres

In this section, we focus on the Bessel HOMs LP$_{0m}$, specifically those with $m \geq 4$. These modes have field distributions resembling the Bessel-Gauss beam in free space given by [11]:

$$E(r,\theta,z) = A_0 J_0\left(k_t r\right)\exp\left(-r^2/w_0^2\right), \tag{2.12}$$

where A_0 is a complex amplitude factor, w_0 is the width of the Gaussian term and r is the radial coordinate. k_t is the transverse wave vector of the beam. Ideal free-space Bessel beams have a central peak that diffracts much slower than the Gaussian beam [12]. However, they carry infinite power and the fractional power within any finite cross-sectional area is zero. A Bessel-Gauss beam is a practical approximation to the ideal Bessel beam by multiplying a Gaussian profile to it. The recent use of such practical Bessel beams in applications such as optical trapping [13, 14], imaging [15] and

material processing [16] makes power scalable fibre sources operating with a Bessel-like HOM attractive.

However, what really makes these HOMs a promising alternative to the fundamental mode is their increased stability in multimode fibres. As mentioned in the preceding section, practical fibres usually suffer from microbends induced by fabrication imperfections and bending induced perturbations. Bessel HOMs have been demonstrated to be more resistant to such distortions and less susceptible to coupling. It is reported that in simulations a transverse ripple in the refractive index profile of the fibre due to fabrication errors, although do not couple modes, causes less distortions in the intensity distribution of the LP_{0m} modes as the mode order m increases [17]. In a bent fibre, Bessel HOMs also suffer less from the distortion and reduction in effective area induced by the effectively "tilted" refractive index profile [8] than the fundamental mode in LMA fibres [18]. This "tilt" arises from a conformal mapping of the bent fibre into an equivalent straight fibre. Thus, the actual refractive index is essentially unaffected, except for a much smaller (and normally counteracting) change induced by stress change. As depicted in Figure 2.2, when a fibre is bent and the refractive index as mapped is "tilted", there are regions in the core with local index lower than the effective index of some modes. In those regions, the perturbed field of those modes becomes evanescent and thus largely negligible. In other words, some modes with higher effective index are "pushed out" of these forbidden regions. The fundamental mode has the highest effective index and is most susceptible to this effect whereas HOMs have lower indices and are less affected. Under the bent perturbation, mode coupling is also less likely to happen for LP_{0m} modes with larger m. As introduced in the previous section, fibre bends mostly couple modes between LP_{0m} with its nearest neighbour antisymmetric mode LP_{1m}. Therefore, the effective separation between the two modes $\Delta n_{eff} = n_{0m} - n_{1m}$ becomes a good indicator of the stability of the LP_{0m} modes under bending. In a multimode fibre where LP_{0m} modes with different m are supported, this index separation increases with m, and can be more than one order of magnitude higher than the separation between LP_{01} and LP_{11} [19].
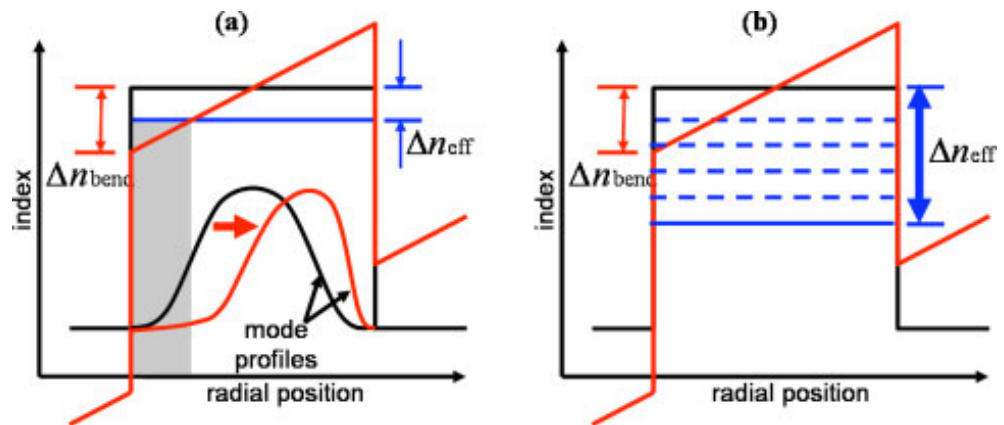
Figure 2.2: (a) Bend induced refractive index change, causing distortion with a "forbidden" grey-shaded region, and possibly leakage of the fundamental mode into the cladding. (b) For HOMs, the

effective indices are lower and less likely to fall into the "forbidden" region. Figures are from [17] with permission from WILEY©.

The improved stability of HOMs allows for single mode operation in fibres with significantly larger core and huge potential for effective area scaling compared with the fundamental mode. This can be attractive to applications where large effective area is needed to suppress nonlinear effects. For instance, recent demonstrations of fibre amplifiers operating with HOMs have mode area of around $3000\ \mu m^2$ and higher with the record of $6000\ \mu m^2$ in double-clad step-index fibres [20-22]. In comparison, LMA fibre amplifiers for the fundamental mode based on ultra-low NA solid core fibres have typical mode area of $500 - 1000\ \mu m^2$ [23], but has limited mode area scalability. Higher mode area with $\sim3000\ \mu m^2$ can be achieved with microstructured fibres [24], which however can be complicated to fabricate.

HOMs can be generated using a LPG that converts the fundamental mode in the inner core to the desired LP_{0m} mode in the outer core of a matching fibre with conversion efficiency exceeding 99% [17]. Alternatively, they can be excited from free-space Bessel beams with amplitude and phase structures matching the target HOM in the fibre. These Bessel beams can be converted from a Gaussian beam by axicons [25], annular slits [12] or computer-generated holograms (CGHs) displayed on a SLM [26]. The converted Bessel beam is then imaged onto the launching end of the fibre. With appropriate combination of optics, a target HOM can be excited with power over 15 dB higher than the strongest parasitic mode [26].

HOMs can also be converted back to the fundamental mode if desired. Conversion with linear optical elements from a single (fundamental) mode to another single (higher order) mode has the same conversion efficiency in both directions. Thus, for example, HOMs generated by LPGs can be readily converted back by adding the same type of LPG at the fibre output [17]. Alternatively, one can convert the output Bessel beam into a Gaussian beam with axicons or CGHs [22, 26]. Here, spatial filtering such as apertures is required to improve the beam quality of the converted beam, insofar as the efficiency of the conversion to the desired mode is limited to the point where significant power ends up in undesired modes.

2.2.4 Fibre modes with orbital angular momentum

In 1992, Allen *et al*. recognized that optical beams with a phase front characterized by $\exp(il\varphi)$ carries an OAM of $l\hbar$ per photon [27]. The number l denotes the number of intertwined helices and is a positive or negative integer depending on the handedness of the helices. It is also usually referred to as the topological charge number. For instance, charge 1 corresponds to a single helix, and charge 2 corresponds to two intertwined helices with a change in longitudinal phase of 4π along a circle around the centre in a plane orthogonal to the direction of propagation. In fibres, optical vortices carrying OAM were first observed in a stressed fibre [28]. Their formation and representation in

fibres were subsequently described [29, 30]. In a circularly symmetric fibre, beams carrying OAM can be expressed as a linear combination of the degenerate even and odd variants of a hybrid mode such as HE$_{l+1,m}$ or EH$_{l-1,m}$ with $l > 0$ that have $\pi/2$ longitudinal phase shift between them. In general, one can write the transverse electric field of OAM modes (OAMM) with azimuthal order l and radial order m as:

$$\text{OAMM}_{\pm l,m}^{\pm} = \text{HE}_{l+1,m}^{e} \pm i\text{HE}_{l+1,m}^{o} = F_{l,m}(r)\sigma^{\pm}\exp(\pm il\varphi)\exp(i\beta_{l+1,m}^{\text{HE}}z), \qquad (2.13)$$

$$\text{OAMM}_{\pm l,m}^{\mp} = \text{EH}_{l-1,m}^{e} \pm i\text{EH}_{l-1,m}^{o} = F_{l,m}(r)\sigma^{\mp}\exp(\pm il\varphi)\exp(i\beta_{l-1,m}^{\text{EH}}z). \qquad (2.14)$$

Here, $F_{l,m}(r)$ is the radial field distribution of the corresponding LP$_{lm}$ mode, $\beta_{l+1,m}^{\text{HE}}$ and $\beta_{l-1,m}^{\text{EH}}$ are the propagation constants corresponding to the HE or EH modes that form the OAMM, ϕ is the azimuthal coordinate and $\sigma^{\pm} = \hat{x} \pm i\hat{y}$ represents left or right-handed circular polarization that also leads to spin angular momentum (SAM) with $s = \pm 1$. From the equations it is evident that these OAM modes with azimuthal order l carry OAM of $l\hbar$ per photon. The handedness of the circular polarization and the OAMM distinguish the type of modes that form the OAMM. The OAMMs formed with pairs of HE modes have the same sign of the charge number and the SAM and are hence denoted as spin-orbit aligned (SOa) OAMMs, while those formed with pairs of EH modes have opposite sign for the charge and the SAM and are thus spin-orbit anti-aligned (SOaa) OAMMs.

OAMMs are linear combination of the hybrid modes, but it is also possible to express the hybrid modes as a linear combination of OAMMs. This is expected from equations (2.13) and (2.14). For instance, the linearly polarized fundamental mode and the Bessel HOMs that do not carry OAM can be written as a combination of circularly polarized OAMMs with $l = 0$. Generally, the OAMMs and hybrid modes can be viewed as belonging to alternative modal bases. Thus, for example, even though an OAMM can couple to its conjugate and the superposition of the two OAMMs can form a hybrid mode, it is inappropriate to say that the OAMM couples to the hybrid mode, even if the simplest representation of the optical field changes from an OAMM to a hybrid mode. Note also that the OAMM set is attractive for fibres since it does not require the orientation of transverse axes to be defined.

OAMMs in fibre with $l > 1$ can be either SOa or SOaa while for $l = 1$ there is only SOa OAMM since only the corresponding HE$_{2m}$ mode pairs exist. Also, unlike the $l > 1$ case, the transverse modes TM$_{0m}$ and TE$_{0m}$ that are in the same LP mode group with the HE$_{21}$ mode cannot form OAMMs with their linear combinations like the EH modes, despite their similarity in the transverse electric field distributions. This is because TM and TE modes, which can be expressed as follows [31], are not degenerate:

$$\text{TM}_{0m} = \frac{F_{1m}(r)}{2}\left(\sigma^{-}\exp(i\phi) + \sigma^{+}\exp(-i\phi)\right)\exp(i\beta_{0,m}^{\text{TM}}z), \qquad (2.15)$$

$$\mathrm{TE}_{0m} = \frac{-iF_{1m}(r)}{2}\left(\sigma^- \exp(i\phi) - \sigma^+ \exp(-i\phi)\right)\exp\left(i\beta_{0,m}^{\mathrm{TE}}z\right). \tag{2.16}$$

Here $\beta_{0,m}^{\mathrm{TM}}$ and $\beta_{0,m}^{\mathrm{TE}}$ are the propagation constants of the TM and TE modes, respectively, which are similar but not equal. Therefore, it is usually necessary to increase the index separation between the HE_{21} modes and the transverse modes to ensure robust guidance of the $l = 1$ OAMM in fibre [32].

Under the weakly guiding approximation, the (quasi-) degenerate vector modes that have (almost) the same propagation constants are grouped into one LP mode (group) that is four-fold quasi-degenerate. The modes in the group are either cosine or sine depending on the azimuthal angle, and even or odd depending on the polarization direction. In analogy to the vector modes, OAMMs can also be formed by combining two degenerate LP modes that are cosine and sine or even and odd with 90-degree longitudinal phase difference between them. Contrary to the circularly polarized OAMMs formed by the vector modes, these OAMMs formed by the LP modes are linearly polarized. For example, the sine and cosine version of LP_{21}, with a 45-degree azimuthal phase difference, can be combined with a 90-degree longitudinal phase difference to form a charge-2 linearly polarized OAMM of the first radial order. From a vector mode picture, this OAMM can be regarded as the superposition of SOa and SOaa OAMMs formed by pairs of HE_{31} and pairs of EH_{11}. Note that the OAMMs formed by LP modes are approximations to the true OAMMs formed by the vector modes. However, in short weakly guiding step-index fibres such approximation is adequate. In this thesis, I present two FRAs for OAMMs. The first one operates with a charge 2 circularly polarized OAMM and the other with a charge 15 linearly polarized OAMM. Although we used modal decomposition to measure the purity of the target OAMM in both cases, the purity measurement for linearly polarized OAMMs can be done with a much easier scalar intensity analysis method [33].

It has been reported that OAMMs have some unique features compared with the conventional modes in terms of stability under perturbations such as bends. For the non-OAM modes, coupling between the degenerate counterparts are especially likely as they have identical effective indices. Bending or other geometry-induced birefringence can cause polarization-mode dispersion, causing degenerate modes with different polarizations to mix, which is usually the case with LP_{0m} modes in a bent circular fibre. However, for OAMMs with non-zero charge l, coupling between their degenerate counterparts involves changing the OAM by $|2l|$. Therefore, such mode mixing becomes more difficult for OAMMs with high l [34]. In addition, OAMMs show greater resistance to 3D geometric perturbations which is not seen with a vector mode [35]. The coupling between OAMMs with neighbouring charges are still affected by the effective index separation, which also becomes less likely for OAMMs with high l, as is the case for the Bessel HOMs.

Recent research mostly focuses on OAMMs in optical fibres with an air core or ring-shaped refractive index profile. Broadly speaking, these designs introduce high field intensity and field gradient at the refractive index steps, which in combination with a large core-cladding index difference, yields large

effective index separation between the quasi-degenerate modes such as HE and EH modes for $l > 1$ OAMMs or HE and TE, TM modes for $l = 1$ OAMMs, suppressing mode coupling [31, 36]. The index profile can also be tailored to suppress OAMMs with higher radial order that may be close to the target mode in effective index. Such designs enable stable propagation of a single or multiple OAMMs over long fibres, which is beneficial for applications like mode-division multiplexing in fibre-optic communications [37, 38]. Inline rare-earth doped amplifiers with ring-core fibres have been demonstrated for a single charge 1 OAMM [32, 39] and proposed for multiple OAMMs with optimized differential modal gain [40, 41]. Raman amplification of OAMMs in ring-core fibres have also been demonstrated [42]. It is also possible to amplify a single or multiple OAMMs in regular step-index fibres with solid core, especially for high-power applications such as material processing [43] and long distance free-space optical communication [44]. Step-index fibres can support multiple OAMMs with different radial orders that are higher than one. Their simple geometry also makes them readily compatible with current high power multimode pump sources.

Similar to Bessel HOMs, OAMMs can either be converted from the fundamental mode in fibres, for instance by stress induced gratings [45] or fused fibre couplers [46], or free-space excited from donut-shaped Laguerre-Gaussian (LG) beams. These LG beams can be generated from a Gaussian beam via spiral phase plates (SPPs) [47], nanostructured vortex converter [48] and CGHs on SLMs [49]. For the free-space excitation, the converted OAM beam needs to be matched to the fields in fibre in three components: polarization, OAM, and radial field structure, which can be optimized in free space with conventional polarization controlling, adjustments to the beam converters and the tailoring of the field distributions incident to the converter [7].

2.3 Stimulated Raman scattering in silica optical fibres

2.3.1 Raman scattering in single mode and multimode fibres

Raman scattering in its spontaneous form was first observed in 1928 by C. V. Raman [50]. It can be described as the scattering of a photon by a molecule, in which the molecule is excited to a vibrational state from the ground state and the photon is downshifted to lower frequency [51]. The process is inelastic, and the frequency shift of the photon is decided by the energy difference between the vibration state and the ground state of the molecule. The incident light is referred to as the pump and the frequency shifted light is the Stokes wave. For spontaneous scattering, the power of the Stokes is proportional to the pump power and generally quite weak. Stimulated Raman scattering (SRS) was observed in 1962 by Woodbury [52] and can lead to a Stokes wave that grows rapidly and depletes a significant fraction of the pump wave. In SRS, the beating between the pump and Stokes wave drives the vibrations. There is thus a positive feedback to the Raman scattering. Insofar as SRS dominates over spontaneous Raman scattering, the Stokes wave grows exponentially until pump depletion becomes significant. Strictly, SRS occurs for any pump power. Thus, there is no definite

threshold (unless there is a laser cavity), but nevertheless, a somewhat arbitrary threshold or critical power is often defined. Famously, SRS was reported in silica fibres in 1972 by R. H. Stolen [53]. In the continuous wave regime, the intensity of the copropagating Stokes wave and the pump wave is related with two coupled equations [51]

$$\frac{dI_S}{dz} = g_R I_p I_S - \alpha_S I_S,$$
(2.17)

$$\frac{dI_p}{dz} = -\frac{\omega_p}{\omega_S} g_R I_p I_S - \alpha_p I_p,$$
(2.18)

where g_R is the Raman gain coefficient, α_p and α_S are the fibre background loss at the pump and Stokes frequencies ω_p and ω_S, respectively. From the equations we can see that in the absence of loss, each Stokes photon corresponds to a pump photon, i.e., the total number of photons is conserved. The Raman gain coefficient is dependent on the frequency shift between the pump and Stokes wave as well as the composition of the medium. In silica glass fibres, due to the amorphous nature of the gain medium, the gain spectrum is a continuum that spans over 40 THz, with a broad peak at ~13 THz, as shown in Figure 2.3. The gain coefficient also depends on the polarizations of the pump and signal. For completely scrambled polarization g_R is reduced by a factor of two from the value of the co-polarized pump and Stokes, if the much smaller contribution of SRS between orthogonally polarized waves is neglected. In addition, although the Raman gain spectrum in Figure 2.3 applies at least approximately for any pump wavelength, the peak value is at least approximately inversely proportional to the pump wavelength [51]. In fused silica, the gain coefficient is ~1×10⁻¹³ m/W for pumping at 1 μm wavelength when the signal is co-polarized with the pump [51].
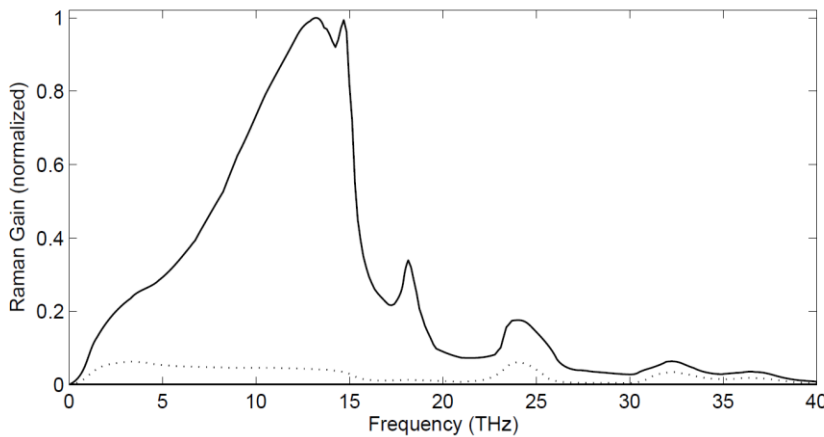
Figure 2.3: Normalized Raman gain coefficient versus the frequency shift between pump and Stokes in silica. Solid curve: pump and Stokes in the same polarization; Dashed curve: pump and Stokes in the orthogonal polarization. Plot from [51].

In the absence of pump depletion, the small signal Raman gain in a single mode fibre with input pump power $P_p(0)$ is given by

$$G = \frac{g_R P_p(0) L_{eff}}{A_{eff}}. \tag{2.19}$$

The Stokes at the output of the fibre with length L is given by

$$P_S(z) = P_S(0) \exp(G - \alpha_S L). \tag{2.20}$$

Here, the Raman gain is in nepers and can be converted to the gain in dB with $G_{dB} \approx 4.343G$. L_{eff} is the effective fibre length given by:

$$L_{eff}(z) = \frac{1 - \exp(-\alpha_p L)}{\alpha_p}. \tag{2.21}$$

The effective area which describes how the pump and Stokes beam overlaps is given by

$$A_{eff} = \frac{\left(\iint |F(x,y)|^2 \, dxdy\right)^2}{\iint |F(x,y)|^4 \, dxdy}, \tag{2.22}$$

where $F(x,y)$ is the field distribution for the fundamental mode. Also note that $|F(x,y)|^2$ is proportional to the modal intensity.

In equation (2.22), the modal distribution is assumed to be the same for the pump and Stokes wave. This is reasonable for typical single-mode fibres. If the modes are different, one can instead use

$$A_{eff} = \frac{\left(\iint I_p(x,y)dxdy\right)\left(\iint I_S(x,y)dxdy\right)}{\iint I_p(x,y)I_S(x,y)dxdy}, \tag{2.23}$$

where I_p and I_S are the intensities of the pump and the Stokes modes, respectively.

This expression for the effective area can be used also in case of multimode pump and Stokes waves if the I_p and I_S are the total intensities of the power in all pump and the Stokes modes [54]. Then, the Stokes power can still be roughly evaluated using the coupled equations (2.17) and (2.18). However, mode-coupling and mode-selective gain and depletion can then cause the intensity distributions to change along the fibre. If the mode coupling in the pump and Stokes wave is weak, the evolution of Stokes power can then be accurately evaluated separately for each mode, with coupled equations in which the modal power of each mode at Stokes wavelength receives contribution from each of the pump modes [55]. In this case, the spatial and temporal evolution of the pump and Stokes beam is given by:

$$\frac{\partial P_i^p(z,t)}{\partial z} + \frac{1}{v_i^p}\frac{\partial P_i^p(z,t)}{dt} = -\alpha_i^p P_i^p(z,t) - \frac{\lambda_S}{\lambda_p}\sum_{k=1}^{N_S}\frac{g_R P_k^S(z,t)}{A_{i,i,k,k}^{eff}} P_i^p(z,t), \tag{2.24}$$

$$\frac{\partial P_j^S(z,t)}{\partial z} + \frac{1}{v_j^S}\frac{\partial P_j^S(z,t)}{dt} = -\alpha_j^S P_j^S(z,t) + \sum_{k=1}^{N_P}\frac{g_R P_k^p(z,t)}{A_{j,j,k,k}^{eff}}P_j^S(z,t). \tag{2.25}$$

This is a simplification from [56], retaining only 1st-order SRS, and can of course also be used for SRS between single-mode pump and Stokes waves. $P_{i,j}^{p,S}$ is the power in a specific mode i or j of the pump (p) or the Stokes wave (S), $v_{i,j}^{p,S}$ is the group velocity of the corresponding modes and $\alpha_{i,j}^{p,S}$ is the background loss of the corresponding mode at the pump or Stokes wavelength λ_p or λ_S.

The effective input power in each signal mode can either be seeded externally or by spontaneous Raman scattering which is equivalent to injecting one fictitious photon at the input [57]. This also assumes that the gain is high and the background loss is negligible compared to the gain in the signal input end of the fibre. The effective area is now defined between each of the modes of the pump and Stokes by replacing the intensities in equation (2.23) with the squared modulus of the electric field ψ_i or ψ_j [58]:

$$A_{i,i,j,j}^{eff} = \frac{\int_0^{2\pi}\int_0^{\infty}|\psi_i(r,\theta)|^2 rdrd\theta \int_0^{2\pi}\int_0^{\infty}|\psi_j(r,\theta)|^2 rdrd\theta}{\int_0^{2\pi}\int_0^{\infty}|\psi_i(r,\theta)|^2 |\psi_i(r,\theta)|^2 rdrd\theta}. \tag{2.26}$$

In a multimode CW or quasi-CW fibre Raman amplifier, the time-derivatives disappear, so the steady state coupled equations for the power in each of the pump or signal mode P_i^p and P_j^s can be written as

$$\frac{dP_i^p(z)}{dz} = \left(-\alpha_i^p - \frac{\lambda_S}{\lambda_p}\sum_{k=1}^{N_S}\frac{g_R P_k^S(z)}{A_{i,i,k,k}^{eff}}\right)P_i^p(z), \tag{2.27}$$

$$\frac{dP_j^S(z)}{dz} = \left(-\alpha_i^S + \sum_{k=1}^{N_P}\frac{g_R P_k^p(z)}{A_{j,j,k,k}^{eff}}\right)P_j^S(z). \tag{2.28}$$

This can be solved with ordinary differential equations solver in numeric computing software such as MATLAB. In our approach, I only consider the pump and the first order Stokes whose linewidths are ignored. For N_{pump} number of pump modes and N_{signal} number of signal modes, the total number of coupled equations is therefore $N_{total} = N_{pump} + N_{signal}$. Each equation is in the following form and corresponds to the power evolution along the fibre for mode q which can be either a pump or signal mode:

$$\frac{dP_q}{dz} = \sum_{k=1}^{N_{total}} G_k P_k P_q. \tag{2.29}$$

Here, the background loss is ignored as the fibre length I use in most of the presented amplifiers are short. G_k is the pairwise gain between mode q and k, which is given by $g_R^{q,k}/A_{eff}^{q,k}$. $A_{eff}^{q,k}$ is the

effective area between the two modes. $g_R^{q,k}$ is the Raman gain coefficient and takes the value from 0, g_R, or $-\lambda_S g_R / \lambda_p$ depending on the wavelengths of the interacting modes. In MATLAB, equation (2.29) can be written as the multiplication between $\boldsymbol{G}$ and $\boldsymbol{P}$, where $\boldsymbol{G}$ is a $N_{total} \times N_{total}$ matrix corresponding to the gain between the interacting modes, and $\boldsymbol{P}$ is a $N_{step} \times N_{total}$ matrix storing the power in each mode at different longitudinal locations with a total of N_{step} points. This method is used in the incoherent simulations for Raman amplification of HOMs presented in the next chapter. It can also be applied to multi-wavelength pumped Raman scattering by including multiple pump wavelengths [59].

If the coupling between modes in the core is sufficiently strong for them to reach an equilibrium before there has been significant Raman amplification, we can assume already that the initial power in both pump and signal is evenly distributed among all the supported modes. The output Stokes power in each mode is then also almost the same, with the total gain equal to the average gain for each signal mode in the absence of mode coupling [55]. In a step-index fibre Raman amplifier with single-mode signal and low-brightness multimode pump, one can assume strong mode coupling for the pump so that the pump has a flat transverse intensity distribution along the fibre. This simplifies the analysis of double clad Raman fibres where the multimode pump is guided in the inner cladding and the signal is in the single mode core [60]. For HOM Raman amplifiers, the primary signal mode is expected to be dominant and resistant to coupling into parasitic modes. Although the other modes may still couple with each other, their overall power is much lower than the primary mode. Hence, the single mode assumption may also apply.

2.3.2 Saturated Raman gain and comparison with ytterbium gain

In Raman scattering, each Stokes photon is converted from a pump photon. As the Stokes power builds up, the pump is depleted, which makes the Raman gain less than the small signal gain (without depletion). For single mode fibre Raman amplifiers, assuming the same background loss at pump and signal wavelengths, from the rule of conserved photons between the pump and Stokes, the saturated Raman gain with pump depletion considered can be derived and is given by [51]:

$$G_S = \frac{(1+r_0)e^{-\alpha L}}{r_0 + G_A^{-(1+r_0)}}, \tag{2.30}$$

where r_0 is related to the signal-to-pump power ratio at the fibre input

$$r_0 = \frac{\lambda_S}{\lambda_p} \frac{P_S(0)}{P_p(0)}. \tag{2.31}$$

and G_A is the small signal linear Raman gain $G_A = \exp(G)$ from equation (2.19). This is useful to quickly evaluate the signal gain when the pump is depleted. By defining a normalized signal output power $r_0 G_A$ that is independent of input pump power, the saturation characteristics can be acquired by plotting the ratio of the saturated gain to the unsaturated gain against $r_0 G_A$ (Figure 2.4). The background loss is ignored. From the plot it is apparent that for a given small signal gain, the gain compression becomes stronger when the normalized output is high. However, such reduction in gain does not get much worse as the small signal gain increases. For instance, for a Raman amplifier with a small signal gain of 10^3, the saturated gain becomes almost 10% of the unsaturated gain if the input signal-to-pump ratio is ~1%. If the small signal gain is increased to 10^4, the gain compression is barely changed for the same normalized output.
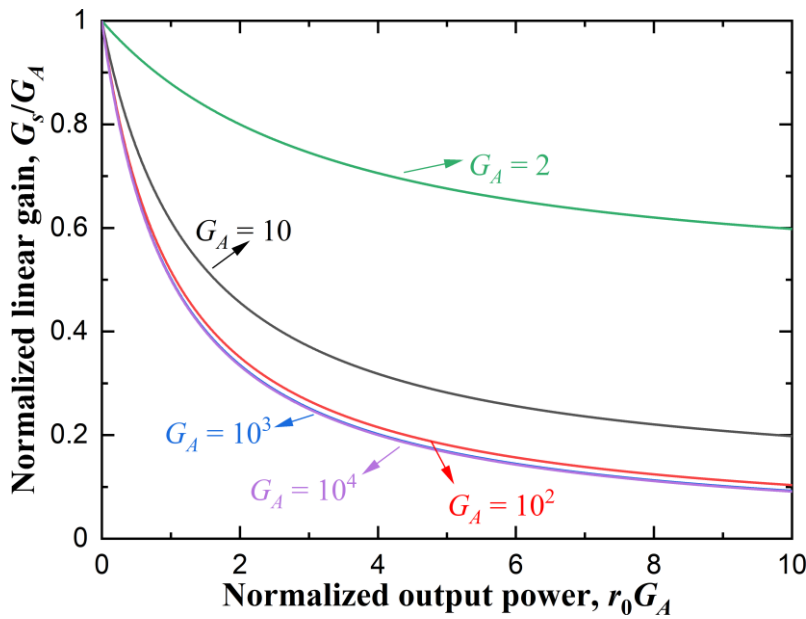
Figure 2.4: The ratio between saturated and small signal linear gain versus the normalized output $r_0 G_A$. Curves with different colours correspond to different small signal Raman gain. The curves for $G_A = 10^3$ and $G_A = 10^4$ are almost overlapping. Plotted after [51].

For multimode FRAs, the analysis can be much more complicated. In the simplest cases when the coupling between the modes for both signal and pump is strong, or when the signal is single mode and the coupling between pump modes is strong, equation (2.30) still applies if the relevant intensities are modified accordingly. The small signal gain can be calculated from the average pump intensity. If the signal power is mostly in a target mode and the parasitic modes combined take only a very small portion of the total power, it is within reasonable approximation that the portion of pump photons going into the parasitic signal modes is negligible, and equation (2.30) can be used to roughly estimate the saturated gain of the target mode. The gain of the parasitic modes can also be estimated by changing r_0 to the ratio of initial power in the parasitic mode and the pump. Therefore, for a typical double-clad FRA or FRA for HOM with almost all the signal power in a single mode, the Raman

gain in the unwanted mode is only roughly 10 times the saturated gain for the target mode, if the input signal-to-pump power ratio is 1% and the small signal gain is 10^3.

If the power in the parasitic signal modes is not negligible, their consumption of pump power cannot be ignored. We can evaluate the local gain of each signal mode $g_i^S(z)$ from the coupled equations (2.27) and (2.28). Assuming weak coupling between the signal modes, the local gain for signal mode i at longitudinal location z, can be written as

$$g_i^S(z) = g_R \sum_{k=1}^{N} \frac{1}{A_{i,k}^{eff}} P_k^p(z).$$ (2.32)

$P_k^p(z)$ is the power in pump mode k at location z. For a fully coupled pump beam, P_k^p is the same for all the modes. Therefore, from equation (2.32), the local gain of mode i is determined by the average of its effective area with each of the pump modes. Although the overlap between modes can vary, for example by a few times in a few-mode step-index fibre, as shown in Table 2.2, making the signal gain from each pump mode quite different, the averaged overlap for a signal mode with all the pump modes is quite similar. The local gain of each signal mode is hence roughly the same. This is usually not the case for GRIN fibres. If the coupling between the pump modes is also weak, for an input pump with its power evenly distributed among all the modes, which is usually assumed for a low-brightness multimode pump source, the gain for different signal modes still does not vary too much if the depletion in each pump mode is relatively uniform. This is the case when the transverse distribution of the pump is not significantly altered due to depletion. For stronger pump depletion, there can be a significant difference in the depletion of different pump modes. The gain saturation can then become mode-selective, as a result of mode-selective pump depletion.

Table 2.2: Calculated overlap integrals between all the supported LP modes in a step index fibre with a core of 20 μm diameter and 0.1 NA.

Overlap integrals $\left(A_{i,j}^{eff}\right)^{-1}$ in 1×10^9 m^{-2}							
Mode	LP$_{01}$	LP$_{11}$	LP$_{21}$	LP$_{02}$	LP$_{31}$	LP$_{12}$	**Average**
LP$_{01}$	4.81	3.23	2.34	3.89	1.72	3.20	**3.20**
LP$_{11}$	3.23	5.18	3.14	1.99	2.66	3.21	**3.23**
LP$_{21}$	2.34	3.14	4.92	1.85	3.08	1.62	**2.82**
LP$_{02}$	3.89	1.99	1.85	5.60	1.91	2.78	**3.00**
LP$_{31}$	1.72	2.66	3.08	1.91	4.69	1.48	**2.59**
LP$_{12}$	3.20	3.21	1.62	2.78	1.48	4.93	**2.87**

Chapter 2

Compared to the FRAs, the mode-selective gain saturation can be more significant in RE-doped fibre amplifiers as the local gain is affected by the local signal intensity. In an YDFA, the local gain of a signal mode with a transverse intensity distribution $\psi_i^s(x,y)$ at wavelength λ_s can be written as [61]

$$g_i(z) = \iint \left[\left(\sigma_a(\lambda_s) + \sigma_e(\lambda_s) \right) n_2(x,y,z) - \sigma_a(\lambda_s) \right] N_0(x,y) \psi_i^s(x,y) \, dxdy , \qquad (2.33)$$

where N_0 is the distribution of Yb ions, $\sigma_a(\lambda)$ and $\sigma_e(\lambda)$ are the cross-sections of absorption and emission at wavelength λ, and n_2 is the local fractional excitation of Yb-ions. At steady state, the fractional excitation is given by:

$$n_2(x,y,z) = \frac{\displaystyle\sum_{k=p,s} \frac{P_k(z)\psi^k(x,y)\sigma_a(\lambda_k)}{hc/\lambda_k}}{\tau^{-1} + \displaystyle\sum_{k=p,s} \frac{P_k(z)\psi^k(x,y)\left[\sigma_a(\lambda_k) + \sigma_e(\lambda_k)\right]}{hc/\lambda_k}} \qquad (2.34)$$

Here, τ is the spontaneous lifetime of the upper state that determines the rate of spontaneous emission. P_p, P_s and ψ^p, ψ^s are the total power and normalized intensity distributions of pump and signal, respectively. The local intensity is given by the product of the power and the intensity distribution. Since the Yb-ions are de-excited when the signal is amplified, the local fractional excitation becomes smaller at higher local signal intensity. This leads to gain saturation. In case the signal power is primarily in a single signal mode, the reduction in the fractional excitation follows the intensity distribution of that mode. Therefore, the local gain for competing modes, which is much lower in power than the seeded mode at launch, can have higher gain. In contrast to an FRA, this can happen even in the absence of pump depletion, although mode-selective pump depletion can add to the mode-selective gain saturation also in an YDFA. The difference between the saturated and unsaturated gain in the YDFA can also be much higher than in the FRA. For instance, in an unoptimized cladding pumped YDFA, the unsaturated gain for the HOMs can be significantly higher than the saturated signal gain for the target fundamental mode (e.g. 90 dB *vs.* 15 dB) [61]. Such high gain will lead to substantial build-up of power in unwanted modes which can either originate from external seeding, mode-coupling, or in the form of ASE. The signal mode purity can therefore see significant degradation.

2.4   References

[1]   K. Okamoto, *Fundamentals of Optical Waveguides* (Elsevier Science & Technology, 2006).

[2]   A. W. Snyder, and J. Love, *Optical Waveguide Theory* (Springer US, 1983).

[3]   A. Mendez, T. F. Morse, and T. F. Morse, *Specialty Optical Fibers Handbook* (Elsevier Science & Technology, 2007).

[4]   D. Gloge, "Weakly guiding fibers," Appl. Opt. **10**, 2252 (1971).

[5]   A. W. Snyder, "Coupled-mode theory for optical fibers," J. Opt. Soc. Am. **62**, 1267 (1972).

[6]   D. Marcuse, *Theory of Dielectric Optical Waveguides* (Elsevier Science, 2013).

[7]   P. C. Gregg, "*Optical angular momentum in air core fibers*," PhD dissertation (Boston University, 2017).

[8]   H. Taylor, "Bending effects in optical fibers," J. Lightwave Technol. **2**, 617 (1984).

[9]   R. Ulrich, S. C. Rashleigh, and W. Eickhoff, "Bending-induced birefringence in single-mode fibers," Opt. Lett. **5**, 273 (1980).

[10]   A. Bjarklev, "Microdeformation losses of single-mode fibers with step-index profiles," J. Lightwave Technol. **4**, 341 (1986).

[11]   F. Gori, G. Guattari, and C. Padovani, "Bessel-Gauss beams," Opt. Commun. **64**, 491 (1987).

[12]   J. Durnin, J. J. Miceli, and J. H. Eberly, "Diffraction-free beams," Phys. Rev. Lett. **58**, 1499 (1987).

[13]   K. Dholakia, and T. Čižmár, "Shaping the future of manipulation," Nat. Photonics **5**, 335 (2011).

[14]   O. M. Maragò, P. H. Jones, P. G. Gucciardi, G. Volpe, and A. C. Ferrari, "Optical trapping and manipulation of nanostructures," Nat. Nanotechnol. **8**, 807 (2013).

[15]   T. A. Planchon, L. Gao, D. E. Milkie, M. W. Davidson, J. A. Galbraith, C. G. Galbraith, and E. Betzig, "Rapid three-dimensional isotropic imaging of living cells using Bessel beam plane illumination," Nat. Methods **8**, 417 (2011).

[16]   M. Duocastella, and C. B. Arnold, "Bessel and annular beams for materials processing," Laser & Photon. Rev. **6**, 607 (2012).

[17]   S. Ramachandran, J. M. Fini, M. Mermelstein, J. W. Nicholson, S. Ghalmi, and M. F. Yan, "Ultra-large effective-area, higher-order mode fibers: a new strategy for high-power lasers," Laser & Photon. Rev. **2**, 429 (2008).

[18]   J. M. Fini, and S. Ramachandran, "Natural bend-distortion immunity of higher-order-mode large-mode-area fibers," Opt. Lett. **32**, 748 (2007).

[19]   S. Ramachandran, J. W. Nicholson, S. Ghalmi, M. F. Yan, P. Wisk, E. Monberg, and F. V. Dimarcello, "Light propagation with ultralarge modal areas in optical fibers," Opt. Lett. **31**, 1797 (2006).

[20]   J. W. Nicholson, J. M. Fini, A. M. DeSantolo, E. Monberg, F. DiMarcello, J. Fleming, C. Headley, D. J. DiGiovanni, S. Ghalmi, and S. Ramachandran, "A higher-order-mode Erbium-doped-fiber amplifier," Opt. Express **18**, 17651 (2010).

[21]   J. W. Nicholson, J. M. Fini, A. M. DeSantolo, X. Liu, K. Feder, P. S. Westbrook, V. R. Supradeepa, E. Monberg, F. DiMarcello, R. Ortiz, C. Headley, and D. J. DiGiovanni, "Scaling the effective area of higher-order-mode erbium-doped fiber amplifiers," Opt. Express **20**, 24575 (2012).

[22]   K. S. Abedin, R. Ahmad, A. M. DeSantolo, and D. J. DiGiovanni, "Reconversion of higher-order-mode (HOM) output from cladding-pumped hybrid Yb:HOM fiber amplifier," Opt. Express **27**, 8585 (2019).

[23]   D. Jain, Y. Jung, P. Barua, S. Alam, and J. K. Sahu, "Demonstration of ultra-low NA rare-earth doped step index fiber for applications in high power fiber lasers," Opt. Express **23**, 7407 (2015).

[24]   F. Stutzki, F. Jansen, T. Eidam, A. Steinmetz, C. Jauregui, J. Limpert, and A. Tünnermann, "High average power large-pitch fiber amplifier with robust single-mode operation," Opt. Lett. **36**, 689 (2011).

[25]   J. H. McLeod, "The axicon: a new type of optical element," J. Opt. Soc. Am. **44**, 592 (1954).

[26]   J. Demas, L. Rishøj, and S. Ramachandran, "Free-space beam shaping for precise control and conversion of modes in optical fiber," Opt. Express **23**, 28531 (2015).

[27]   L. Allen, M. W. Beijersbergen, R. J. C. Spreeuw, and J. P. Woerdman, "Orbital angular momentum of light and the transformation of Laguerre-Gaussian laser modes," Phys. Rev. A **45**, 8185 (1992).

[28]   D. McGloin, N. B. Simpson, and M. J. Padgett, "Transfer of orbital angular momentum from a stressed fiber-optic waveguide to a light beam," Appl. Opt. **37**, 469 (1998).

[29]   A. N. Alexeyev, T. A. Fadeyeva, A. V. Volyar, and M. S. Soskin, "Optical vortices and the flow of their angular momentum in a multimode fiber," Semiconductor Physics, Quantum Electronics & Optoelectronics **1**, 82 (1998).

[30]   P. Z. Dashti, F. Alhassen, and H. P. Lee, "Observation of orbital angular momentum transfer between acoustic and optical vortices in optical fiber," Phys. Rev. Lett. **96**, 043604 (2006).

[31]   S. Ramachandran, and P. Kristensen, "Optical vortices in fiber," Nanophotonics **2**, 455 (2013).

[32]   Y. Jung, Q. Kang, R. Sidharthan, D. Ho, S. Yoo, P. Gregg, S. Ramachandran, S. Alam, and D. J. Richardson, "Optical orbital angular momentum amplifier based on an air-hole erbium-doped fiber," J. Lightwave Technol. **35**, 430 (2017).

[33] Y. Jiang, G. Ren, H. Li, M. Tang, Y. Liu, Y. Wu, W. Jian, and S. Jian, "Linearly polarized orbital angular momentum mode purity measurement in optical fibers," Appl. Opt. **56**, 1990 (2017).

[34] P. Gregg, P. Kristensen, and S. Ramachandran, "Conservation of orbital angular momentum in air-core optical fibers," Optica **2**, 267 (2015).

[35] Z. Ma, G. Prabhakar, P. Gregg, and S. Ramachandran, "Robustness of OAM fiber modes to geometric perturbations," in *Conference on Lasers and Electro-Optics*(Optical Society of America, San Jose, California, 2018), p. SW3K.1.

[36] S. Ramachandran, P. Gregg, P. Kristensen, and S. E. Golowich, "On the scalability of ring fiber designs for OAM multiplexing," Opt. Express **23**, 3721 (2015).

[37] C. Brunet, P. Vaity, Y. Messaddeq, S. LaRochelle, and L. A. Rusch, "Design, fabrication and validation of an OAM fiber supporting 36 states," Opt. Express **22**, 26117 (2014).

[38] C. Brunet, B. Ung, L. Wang, Y. Messaddeq, S. LaRochelle, and L. A. Rusch, "Design of a family of ring-core fibers for OAM transmission studies," Opt. Express **23**, 10553 (2015).

[39] L. Xu, Y. Shang, J. Yang, Z. Chen, F. Pang, H. Liu, Y. Dong, N. Chen, J. Wen, and T. Wang, "Orbital angular momentum optical amplifier based on PbS-doped ring-core fiber," Front. Phys. **8** (2020).

[40] Q. Kang, P. Gregg, Y. Jung, E. L. Lim, S.-u. Alam, S. Ramachandran, and D. J. Richardson, "Amplification of 12 OAM Modes in an air-core erbium doped fiber," Opt. Express **23**, 28341 (2015).

[41] J. Ma, F. Xia, S. Chen, S. Li, and J. Wang, "Amplification of 18 OAM modes in a ring-core erbium-doped fiber with low differential modal gain," Opt. Express **27**, 38087 (2019).

[42] L. Zhu, J. Li, G. Zhu, L. Wang, C. Cai, A. Wang, S. Li, M. Tang, Z. He, S. Yu, C. Du, W. Luo, J. Liu, J. Du, and J. Wang, "First demonstration of orbital angular momentum (OAM) distributed Raman amplifier over 18-km OAM fiber with data-carrying OAM multiplexing and wavelength-division multiplexing," in *Optical Fiber Communication Conference*(Optical Society of America, San Diego, California, 2018), p. W4C.4.

[43] J. Hamazaki, R. Morita, K. Chujo, Y. Kobayashi, S. Tanda, and T. Omatsu, "Optical-vortex laser ablation," Opt. Express **18**, 2144 (2010).

[44] G. Xie, L. Li, Y. Ren, H. Huang, Y. Yan, N. Ahmed, Z. Zhao, M. P. J. Lavery, N. Ashrafi, S. Ashrafi, R. Bock, M. Tur, A. F. Molisch, and A. E. Willner, "Performance metrics and design considerations for a free-space optical orbital-angular-momentum-multiplexed communication link," Optica **2**, 357 (2015).

[45]   N. Bozinovic, S. Golowich, P. Kristensen, and S. Ramachandran, "Control of orbital angular momentum of light with optical fibers," Opt. Lett. **37**, 2451 (2012).

[46]   S. Pidishety, S. Pachava, P. Gregg, S. Ramachandran, G. Brambilla, and B. Srinivasan, "Orbital angular momentum beam excitation using an all-fiber weakly fused mode selective coupler," Opt. Lett. **42**, 4347 (2017).

[47]   M. W. Beijersbergen, R. P. C. Coerwinkel, M. Kristensen, and J. P. Woerdman, "Helical-wavefront laser beams produced with a spiral phaseplate," Opt. Commun. **112**, 321 (1994).

[48]   M. Beresna, M. Gecevičius, P. G. Kazansky, and T. Gertus, "Radially polarized optical vortex converter created by femtosecond laser nanostructuring of glass," Appl. Phys. Lett. **98**, 201101 (2011).

[49]   N. Matsumoto, T. Ando, T. Inoue, Y. Ohtake, N. Fukuchi, and T. Hara, "Generation of high-quality higher-order Laguerre-Gaussian beams using liquid-crystal-on-silicon spatial light modulators," J. Opt. Soc. Am. A **25**, 1642 (2008).

[50]   C. V. Raman, "A new radiation," Proc. Indian Acad. Sci. - Sect. A **37**, 333 (1953).

[51]   G. P. Agrawal, *Nonlinear Fiber Optics* (Elsevier Science & Technology, 2006).

[52]   G. Eckhardt, R. W. Hellwarth, F. J. McClung, S. E. Schwarz, D. Weiner, and E. J. Woodbury, "Stimulated Raman scattering from organic liquids," Phys. Rev. Lett. **9**, 455 (1962).

[53]   R. H. Stolen, E. P. Ippen, and A. R. Tynes, "Raman oscillation in glass optical waveguide," Appl. Phys. Lett. **20**, 62 (1972).

[54]   C. Headley, and G. P. Agrawal, *Raman Amplification in Fiber Optical Communication Systems* (Elsevier Science, 2005).

[55]   F. Capasso, and P. Di Porto, "Coupled‐mode theory of Raman amplification in lossless optical fibers," J. App. Phys. **47**, 1472 (1976).

[56]   C. A. Codemard, "*High-power cladding-pumped Raman and erbium-ytterbium doped fibre sources,*" PhD dissertation (University of Southampton, 2007).

[57]   R. G. Smith, "Optical power handling capacity of low loss optical fibers as determined by stimulated Raman and Brillouin scattering," Appl. Opt. **11**, 2489 (1972).

[58]   R. Stolen, and J. Bjorkholm, "Parametric amplification and frequency conversion in optical fibers," IEEE J. Quantum Electron. **18**, 1062 (1982).

[59]   S. Hong, Y. Feng, and J. Nilsson, "Off-Peak dual-wavelength multimode diode-laser-pumped fiber Raman laser," IEEE Photonics Technol. Lett. **30**, 1625 (2018).

[60] J. Ji, C. A. Codemard, M. Ibsen, J. K. Sahu, and J. Nilsson, "Analysis of the conversion to the first Stokes in cladding-pumped fiber Raman amplifiers," IEEE J. Sel. Top. Quantum Electron. **15**, 129 (2009).

[61] C. A. Codemard, J. K. Sahu, and J. Nilsson, "Tandem cladding-pumping for control of excess gain in ytterbium-doped fiber amplifiers," IEEE J. Quantum Electron. **46**, 1860 (2010).

Chapter 3   Simulations on gain saturation induced purity degradation in FRAs and YDFAs

3.1   Introduction

In this chapter I present the simulations to investigate the difference in signal mode purity degradation of a target Bessel HOM as a result of the difference in modal gain in RE-doped fibre amplifiers and FRAs. Ideally, all signal power should be in the target mode, but because of the imperfect signal launch, some of the launched power ends up in other modes. By contrast, mode-coupling along the fibre, which can also degrade the mode purity, is neglected. I start with the incoherent scenario with coupled-equations-based simulations in RP Fiber Power for a typical YDFA and in MATLAB for a comparable FRA. I then investigate the purity degradation in coherent amplifiers with BPM in RP Fiber Power for both the YDFA and FRA. Finally, I compare the results of the two different scenarios. The codes for incoherent simulations of the FRA are modified from the work of Mr Soonki Hong, and the codes for coherent BPM simulations are written with the assistance from Dr. Yutong Feng.

3.2   Simulations for incoherent amplifiers

I start with the simulations that match the parameters of our experiments. All the pump and signal modes are assumed to be incoherent and do not couple. The linewidth of our pump and signal sources in most of the experiments in this thesis are in the range of ~5 to 10 nm, or ~1.3 to 2.7 THz. The pump source is multimode with negligible coherence between the modes, so the spatial coherence of the excited pump modes is quite poor already at launch. For the signal modes, they can be spatially coherent at launch when they are excited from a single mode source, however, the coherence between modes degrades quickly for a spectrally broad beam. For instance, two modes with effective index difference of 0.001 remain spatially coherent for 1 m for a spectral linewidth less than 0.3 THz, which corresponds to ~1.1 nm at 1060 nm wavelength [1]. More generally, if the modes can be considered to be distributed evenly in effective index (e.g., in a highly multimode step-index waveguide), the average effective index separation between two modes is one third of the index step. For multimode fibres with index-step 0.0165 (NA 0.22), the average separation becomes 0.0055. With ~10 m length, most modes can be considered incoherent in most of the fibre if the spectral linewidth is over 30 GHz, which is most of the cases for the experiments presented in this thesis. Mode coupling between the signal modes is ignored in the simulations, since high mode coupling is at odds with my objective of high mode purity amplification. Having said that, the targeted signal mode is selected for anticipated low mode-coupling, so the coupling between other modes could be higher. It is also worth noting that if the target mode does couple to another mode, it is more likely to couple to a mode with small

difference in effective index, so the modes can be expected to have above-average coherence. Insofar as there is coupling between parasitic modes (but not with the target mode), this would be expected to reduce the total amplified output power in parasitic modes. The power is expected to be higher in parasitic modes with high gain, so the coupling would transfer power to modes with lower gain.

I evaluate the growth of the parasitic modes, in the absence of coupling between signal modes, by injecting a portion of the total signal power into the parasitic modes, distributed evenly among all the supported modes other than the signal mode. We expect coupling to occur for the pump modes, however, it is convenient to look at the extreme cases where the pump modes do not couple, or the pump modes are fully coupled so that the pump intensity profile is always top-hat shaped. We have compared the results of the YDFA for both cases and found them to be similar. This suggests that the mode-selective gain saturation in my YDFA-simulations is primarily a result of the local signal intensity rather than the pump depletion. The case of fully coupled pump is not simulated for the FRA, since this does not lead to mode-selective gain saturation.

The simulations for the YDFA are conducted with a conventional rate-equation based model [2, 3] in RP Fiber Power. The amplification of each signal mode as well as the depletion of each pump mode are calculated according to the local gain or loss given by equation (2.33) which we repeat here:

$$g_i^w(z) = \int_0^\infty \int_0^{2\pi} N_0 \left[\left(\sigma_a^w + \sigma_e^w \right) n_2(z,r,\phi) - \sigma_a^w \right] \psi_i^w(r,\phi) r \, dr \, d\phi \, . \tag{3.1}$$

Here, N_0 is the total doping concentration of the Yb ions and is assumed uniform across the fibre core, σ_e^w and σ_a^w are the emission and absorption cross-sections for signal (w=s) and pump (w=p) respectively. ψ_i^w is the normalized transverse mode intensity distribution. For the pump $g_i^p(z) < 0$, and ψ_i^w can take values from any appropriate distribution. n_2 is the local fractional population in the excited state at steady state given by equation (2.34). In our realization with RP Fiber Power, the fibre is divided into multiple sections defined by 30 rings with uniform spacing along the radial direction and 16 equal sections in the azimuthal direction. In each section, the optical intensity of a fibre mode is assumed to be constant with value based on the fraction of power in that section. This is slightly different from the validated model in [3] where local fractional population and optical intensities are used. As a result, in our simulations, the difference in the saturated gain between modes are slightly reduced, and the dominant target signal HOM appears to suffer slightly less purity degradation. Nevertheless, repeated simulations with varying spatial resolutions yield almost identical output signal power and purity of the target signal mode, suggesting the impact of using averaged intensity values in sections are small.

For the FRA, the pump power in mode i, P_i^p and signal power in mode j, P_j^s are given by the coupled equations (2.27) and (2.28) under CW conditions. They are repeated here with background loss ignored for the short length of fibre we use in the simulation:

$$\frac{dP_i^p(z)}{dz} = -\frac{\lambda_S}{\lambda_p} g_R \sum_{k=1}^{N_S} \frac{P_k^s(z)}{A_{i,i,k,k}^{eff}} P_i^p(z),$$
(3.2)

$$\frac{dP_j^s(z)}{dz} = g_R \sum_{k=1}^{N_p} \frac{P_k^p(z)}{A_{j,j,k,k}^{eff}} P_j^s(z),$$
(3.3)

where $A_{i,i,j,j}^{eff}$ is the effective area of the intermodal interaction between modes i and j given by equation (2.26).

The parameters used in the simulations are listed in Table 3.1. They are chosen to approximately match the experiments of amplification of LP$_{08}$ in section 4.2. Since the number of modes defined in the simulation software is limited, we scale down the core sizes and NA by 10%. For the YDFA, I assume uniform doping in the fibre core. It is impractical to simulate the large number of cladding modes, hence the YDFA is programmed to be core pumped but with performance similar to typical cladding pumping by scaling down the absorption and emission cross-section values for the pump. The cross-sections are from typical YDF with a phospho-aluminosilicate host. For the FRA, the Raman gain coefficient is chosen to be 45 fm/W which matches the value for unpolarized light in pure silica with 14 THz pump and signal frequency shift in the experiments. The launched signal is set to have 80% of its total power in the target LP$_{08}$ mode and the remaining 20% distributed evenly among all the other modes which include the cosine and sine versions of LP$_{lm}$ with non-zero l. Each parasitic mode has an initial power of ~0.1% of the total input signal. This is chosen to evaluate scenarios where the imperfect signal launch introduces moderate power that is not in a few specific parasitic modes, whereas an optimized signal launch mostly excites the neighbouring LP$_{0m}$ modes and some LP$_{1m}$ modes, each with power 15 dB lower than the target mode [4].

Table 3.1: Parameters for incoherent simulations

Parameter	Value for FRA	Value for YDFA
λ_p	1060 nm	975 nm
λ_s	1115 nm	1045 nm
N_0	N/A	$4 \times 10^{25} \, \text{m}^{-3}$
Core radius	22 μm	22 μm
Core NA	0.2	0.2

Parameter	Value for FRA	Value for YDFA
Fibre length	10 m	10 m
P_s	320 W	2 W
P_p	32 kW	0.2 kW
g_R	45 fm/W	N/A
σ_a^p	N/A	$1.650 \times 10^{-26}\,\mathrm{m^2}$
σ_a^s	N/A	$2.011 \times 10^{-26}\,\mathrm{m^2}$
σ_e^p	N/A	$1.519 \times 10^{-26}\,\mathrm{m^2}$
σ_e^s	N/A	$5.412 \times 10^{-25}\,\mathrm{m^2}$

For both the YDFA and FRA, due to the short fibre length, background loss is considered to be negligible. As we aim to investigate the gain saturation induced mode purity degradation which is mainly a result of the different saturated modal gain, the total signal gains of the two amplifiers are set to be similar for comparison. For the YDFA, the power values are the CW power level for the pump and the averaged power level for the signal. Pulsed pumping of the YDFA is also possible, but in this chapter, we aim to compare the performance of CW operation. Temporal profiles of the pump and signal beams can have significant impact on gain saturation but are beyond the scope of our investigation in this thesis. Owing to the weak nature of Raman scattering, the input pump and signal power levels for the FRA are set to be much higher than those for the YDFA to reduce the fibre length and thus computation time. Such high power is not practical for CW FRAs but can be understood as the instantaneous powers of a nanosecond pulsed device. The length of the gain fibre is short and hence the walk-off between the pump and signal pulses is negligible. Also, the Raman gain is fast enough to be considered instantaneous for nanosecond pulsed FRAs. Therefore, the pulsed FRA is effectively quasi-CW with no difference to the CW case, and setting the high peak power of the pulses is equivalent to setting an artificially high Raman gain coefficient and keeping the pump and signal power close to those of the YDFA. The approach is not expected to change the results if the length scale of the Raman amplification is different from other length scales such as the confocal length and beat lengths. The signal wavelength 1045 nm matches the gain peak wavelength of ~1045-1050 nm estimated from the averaged fractional excitation level in the fibre. Also, given the relatively strong seeding signal power even of parasitic modes (2 mW, ~0.1% of 2 W), the amplified spontaneous emission (ASE) in the YDFA can be neglected. Also note that with negligible ASE and thus no impact of backward-propagating waves, the signal and pump power (and modal distribution) at a given point in the fibre is the same as the output quantities if the fibre is cut at that position.
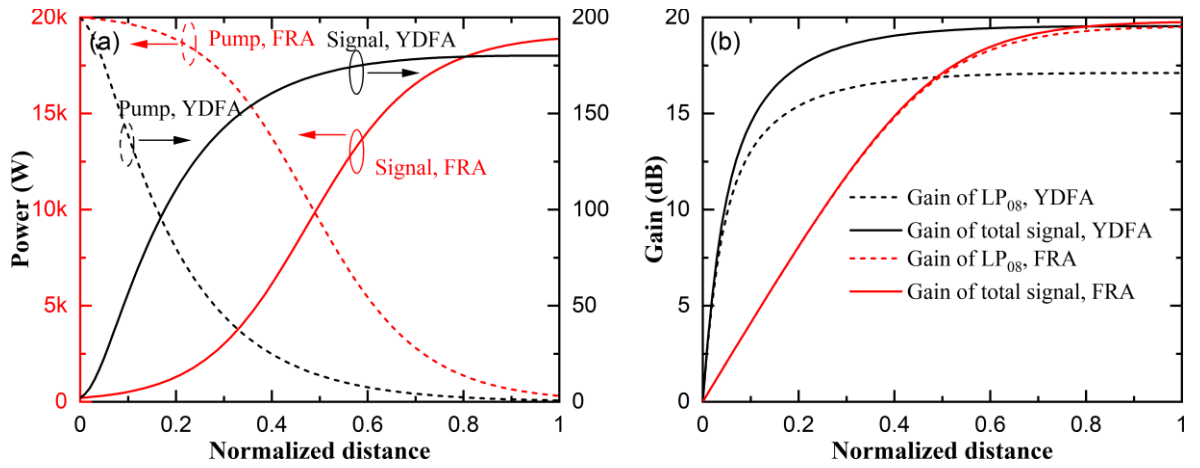
Figure 3.1: Comparisons of power and gain in the YDFA and the FRA in the incoherent simulations. (a) Evolutions of pump (dashed curves) and signal (solid curves) power in the YDFA (black curves) and FRA (red curves). The power of YDFA and FRA are in different scales as indicated by the arrows; (b) The total signal gain (solid curves) and the gain for the target HOM (dashed curves) in the YDFA (black curves) and FRA (red curves).

The evolutions of pump and signal power as well as the gain levels of the two amplifiers along the normalized fibre length are plotted in Figure 3.1. Although the power levels are different for the YDFA and the FRA, the total signal gains are comparable. From Figure 3.1(a), the growth of signal power and the depletion of pump power of the YDFA is faster than in the FRA. At about 50% of the fibre length, the pump depletion in the YDFA reaches ~86% while that in the FRA only reaches ~50%. As predicted, the gain of the target HOM is different in the two amplifiers despite the similar total gain. For the YDFA, the total signal gain is already higher than the gain of the LP_{08} mode by ~1.5 dB at only 10% of the fibre length. At the fibre output, the difference between the gain of the total signal and the LP_{08} mode is 2.44 dB. In comparison, the gain of the LP_{08} remains roughly the same as the total signal gain till the end of the fibre, with a gain difference at the fibre output of only 0.26 dB. As the pump power depletes, the gain saturation in the FRA is much less mode-selective than in the YDFA. These observations are consistent with higher unsaturated gain and mode-selective gain saturation that is primarily driven by the local signal intensity in the YDFA.
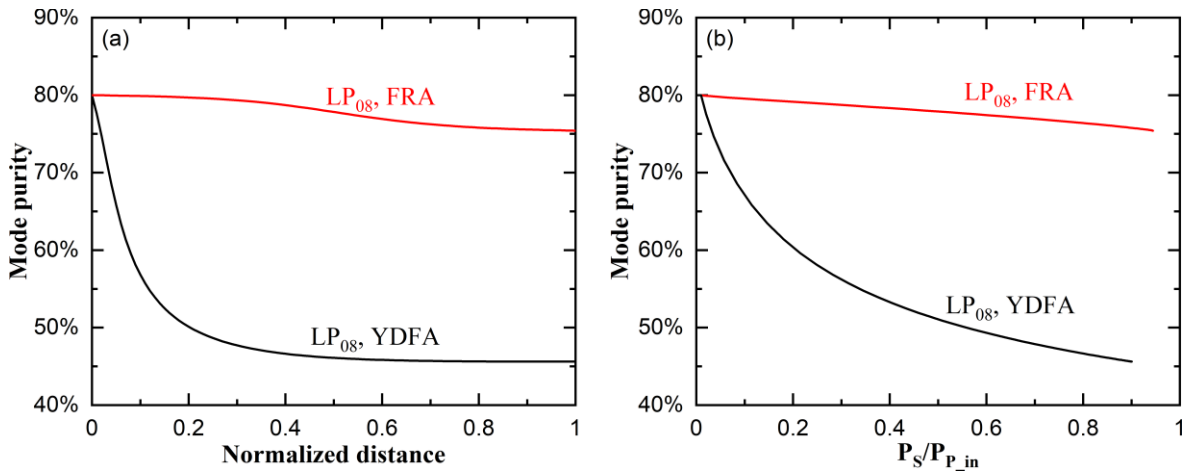
Figure 3.2: Mode purity of the target HOM in the incoherent FRA (red curves) and YDFA (black curves) plotted against (a) normalized distance and (b) normalized signal power. The normalized signal power is calculated as the ratio between the total signal power along the longitudinal direction and the total input pump power.

Consequently, the mode purity degradations are different in the two amplifiers. The evolution of the mode purity, defined as the ratio of power between the target LP_{08} mode and the total signal power, versus the normalized distance, as well as versus total signal power normalized to the launched pump power, are plotted in Figure 3.2. The mode purity quickly drops to ~57% for the YDFA at only 10% of the fibre length as a result of quick pump depletion and settles at 45.6% at the fibre output. In comparison, the mode purity of the FRA drops slowly at the beginning of the fibre, as the transverse pump intensity profile is only marginally altered. The purity then drops slightly faster near the middle of the fibre and eventually reverts to a slower rate and ends with an output purity of 75.4%. If we plot the mode purity against the normalized total signal power, which is given as the ratio between the total signal power and the launched pump power, we can see that the purity drops almost linearly versus the normalized signal power in the FRA. The purity drops much faster in the YDFA, in particular in the beginning of the fibre. The purity drops by 2.44 dB (from 80% to 45.6%) in the YDFA and 0.26 dB (80% to 75.4%) in the FRA. These values are identical to the difference in gain between the target HOM and the total signal gain plotted in Figure 3.1.

The transverse intensity distributions of the input and output pump and signal are also different for the YDFA and the FRA, as shown in Figure 3.3. Note here the intensities are normalized to their respective maximum values. For the FRA, although the edge of the pump seems undepleted, the absolute maximum intensity of the output pump is only ~1.5 % of the averaged intensity of the launched pump, so the gain and thus the difference in modal gain induced by the distorted pump distribution at the output end are small. Therefore, despite the altered shape of residual pump that is expected to favour some of the parasitic modes in the FRA, the saturated gain is still much less mode selective than that in the YDFA. As a result, the intensity profile of the output signal in the FRA is almost identical to the input while the profile in the YDFA sees significant distortion. Since mode coupling is not considered in this simulation, the higher purity degradation in the YDFA is attributed

to the mode-selective gain saturation. Although only one result is presented here, simulations with other fibre parameters lead to the same conclusion, i.e., that that the purity of the signal HOM degrades more in YDFAs than in FRAs with comparable total signal gain levels. Also, note that we have only looked at cladding pumped YDFAs. It is expected that core-pumped YDFAs can be less affected by local gain saturation [5] and therefore may introduce less purity degradation.
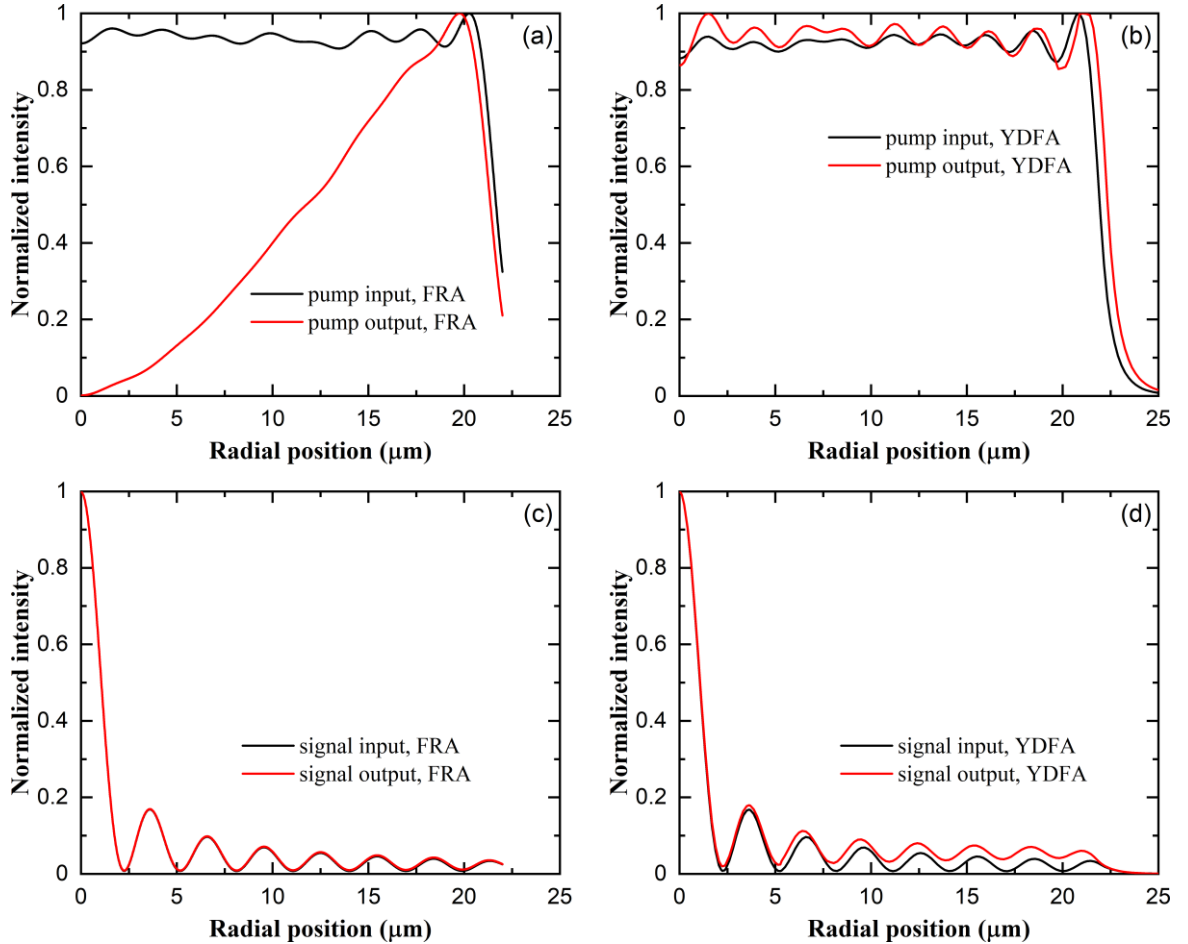
Figure 3.3: Intensity distributions normalized to the maximum value of the respective curves in the radial direction across the centre of the fibre core in the incoherent FRA and YDFA. Input (black curve) and output (red curve) pump distributions of the FRA (a) and the YDFA (b). Input (black curve) and output (red curve) signal distributions of the FRA (c) and the YDFA (d).

3.3   Simulations for coherent amplifiers

I next consider the case of linewidths sufficiently narrow so that the signal and pump modes are (separately) coherent. This is implicitly assumed in BPM. Thus, I investigate this case by propagating the fields with BPM. Information on fibre modes is then extracted afterwards, through post-processing. This is implemented in RP Fiber Power by defining a beam propagating device with two wavelength channels, pump and signal. In the transverse direction, a square computing window with $N \times N$ grid points is defined, large enough for the evanescent fields extending outside the core. In the longitudinal direction, the propagation repeats L/dz number of times where L is the fibre length

and dz is the size of the steps. Each step of propagation can be split into a refraction and a diffraction operation which incorporates the effects of refractive index profile and free-space propagation, respectively. Any gain or loss is also applied for each computation step. Both the transverse and longitudinal resolution need to be high enough to properly sample the transverse variations of the field and to avoid excessive longitudinal field changes. In our simulations, the fibre length is set to 1 m for both amplifiers to reduce the computing time. The grid size N is set to 256 so the transverse resolution is 250 nm. The longitudinal resolution, or the step size, is set to be 2 μm.

In addition, I have taken extra measures to resolve the correct modal power by solving for the eigenfunctions that correspond to the BPM modes. Usually, the power in a specific mode is calculated by taking the spatial integral of the dot product between the BPM field and the amplitude of the mode. In RP Fiber Power, the modal amplitudes are calculated with a mode solver. However, in BPM, the repeated operations in each step in the propagation define "BPM modes" $u_{ij}(x,y)$ which are the unique eigenfunctions in the fibre as defined in the BPM model [6]. These modes are slightly different from, and not orthonormal to, the modes from the mode solver, and hence the calculated modal power is inaccurate. I have therefore implemented the method by M. Feit and J. Fleck, Jr [6] to extract the BPM modes. To start with, the transverse electric field $E(x,y,z)$ in BPM can be written as the sum of all the BPM modes $u_{ij}(x,y)$:

$$E(x,y,z) = \sum_{n,j} A_{nj}(z) u_{nj}(x,y) \exp(-i\beta_n z),$$
(3.4)

where n is the mode index and j in addition distinguishes the different modes within a degenerate set having the same propagation constant β_n. The amplitudes $u_{nj}(x,y)$ denotes the normalized mode function whose transverse integral $\iint |u_{nj}(x,y)|^2 dxdy = 1$, $A_{nj}(z)$ is the corresponding mode amplitude along the fibre. Therefore, in the absence of gain and loss, by defining a correlation function:

$$P(z) = \iint E^*(x,y,0) E(x,y,z) dxdy$$
(3.5)

and taking its Fourier transform against z, one can extract the corresponding propagation constants of the eigenmodes by locating the local maxima and subsequently the eigenfunctions $u_{nj}(x,y)$. Then, the power of a particular mode becomes:

$$|A_n(z)|^2 = \left| \iint E(x,y,z) u_n(x,y) dxdy \right|^2.$$
(3.6)

With this, the parasitic oscillations in the evolution of modal power are reduced. A sample comparison of the mode purity calculated with the amplitudes from mode solver and BPM modes is plotted in Figure 3.4.
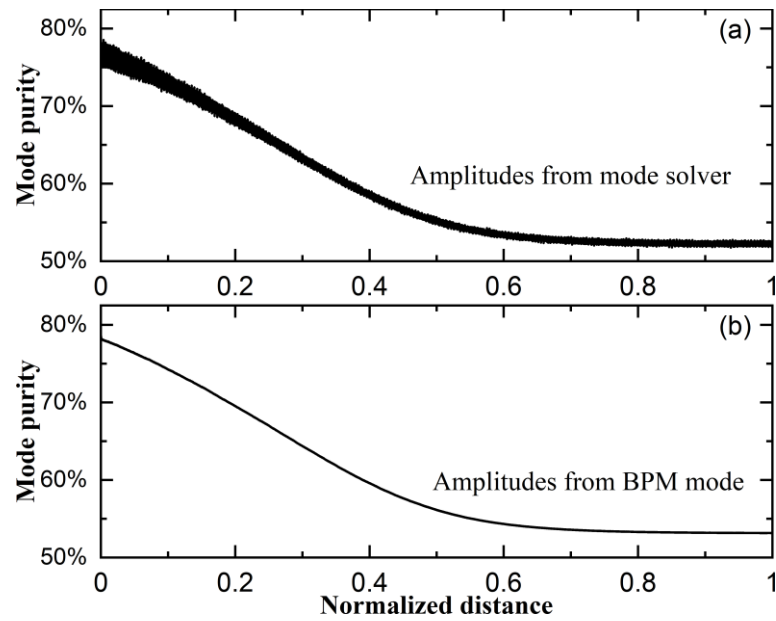
Figure 3.4: Comparison of the mode purity of a sample FRA with different mode field amplitudes. The powers used to calculate the purity are extracted by integrating the BPM fields with the mode amplitude from (a) the mode solver of RP Fiber Power and (b) the extracted BPM eigenmodes.

In BPM, both the pump and signal modes are treated as spatially and temporally coherent for the entire fibre length. The modes are also considered co-polarized. Although this is rarely the case for practical amplifiers, the investigation of completely coherent beams is important as the gain saturation behaves differently compared to the incoherent case, and in the real case, the modes may well be partially coherent, and coherent and incoherent propagation can be considered to be limiting cases.

In stark contrast to the incoherent case, the gain saturation in RE-doped fibre amplifiers can lead to mode competition between coherent modes that suppresses the gain of a mode with lower power compared to a mode with higher power, even if the unsaturated gain is higher for the weaker mode [7]. This is a result of modal interference. BPM accurately models interference and thus coherent mode competition.

Similar to the incoherent simulation, the input pump power is evenly distributed among all the pump modes and the signal power is mostly in the target HOM. The initial field for the pump is therefore the sum all the supported modes with equal power (thus equal modal amplitude) but random phase. For the signal, the initial amplitude is the sum of the target LP_{08} mode with 80% of the total input signal power and all the other modes (including the cosine and sine versions of LP_{lm} modes with non-zero l) with equal power from the remaining 20% and again with random phase. Since it is not possible to acquire the BPM eigenmodes before propagation, we use the modes from the mode solver. (The modes from the mode solver can generally not be written as a sum of BPM modes, so a fraction of the power will be radiated away. However, this effect is negligible.) The two amplifiers are distinguished by the local gain or loss applied at each sub step of the propagations.

Chapter 3

For the YDFA, the local gain is given based on the local fractional Yb-excitation $n_2(x,y,z)$ and the cross-section values at signal or pump wavelength:

$$g(x,y,z,\lambda) = N_0(x,y)\left[(\sigma_a(\lambda) + \sigma_e(\lambda))n_2(x,y,z) - \sigma_a(\lambda)\right]. \tag{3.7}$$

Here N_0 is the predefined doping profile, which is set to be uniform across the fibre core in our case. The steady state $n_2(x,y,z)$ is given by the local intensities:

$$n_2 = \frac{\lambda_p I_p \sigma_a(\lambda_p)/hc + \lambda_s I_s \sigma_a(\lambda_s)/hc}{\lambda_p I_p(\sigma_a(\lambda_p) + \sigma_e(\lambda_p))/hc + \lambda_s I_s(\sigma_a(\lambda_s) + \sigma_e(\lambda_s))/hc + \tau^{-1}}. \tag{3.8}$$

The local gain also applies for the pump evolution for which $g<0$. The cross-section values are for the same type of YDF as used in the incoherent simulations.

For the FRA, the local amplitude of the pump and signal are updated at each propagation step according to the coupled equations for the intensities in section 2.3 which we repeat here:

$$\frac{dI_p}{dz} = -g_R \frac{\lambda_s}{\lambda_p} I_s I_p, \tag{3.9}$$

$$\frac{dI_s}{dz} = g_R I_p I_s. \tag{3.10}$$

The intensities in the BPM are given as the squared modulus of the local amplitudes.

The parameters used in the coherent simulations are listed in Table 3.2. The core size and NA for both the YDFA and the FRA match the values for the incoherent simulation, although smaller than values in the experiments. The pump and signal wavelengths are also matching the incoherent case. To reduce the computation time, the fibre length is scaled down to 1 m and the input pump and signal power values are hence scaled up ten-fold to compensate. For the FRA, the Raman gain coefficient is increased to 100 fm/W as the pump and signal are now co-polarized. It also helps to reduce the length of fibre needed for adequate Raman gain. The nonlinear phase shift is ignored in the simulations as it produces spurious results such as power loss in the target signal mode, which can be a result of the exceptionally high phase change induced by the scaled-up pump power in each computation step. For the YDFA, the cross-sections are identical to the scaled-down values in the incoherent simulation for comparison. In addition to the increased pump and signal power, the doping concentration is also scaled up to reach a concentration-length product for a typical fibre length also in the short fibre.

Table 3.2: Parameters for coherent simulations

Parameter	Value for FRA	Value for YDFA
λ_p	1060 nm	975 nm
λ_s	1115 nm	1045 nm
N_0	N/A	$4 \times 10^{26}\,\mathrm{m}^{-3}$
Core radius	22 μm	22 μm
Core NA	0.2	0.2
Fibre length	1 m	1 m
P_s	2 kW	20 W
P_p	200 kW	2 kW
g_R	100 fm/W	N/A
σ_a^p	N/A	$1.650 \times 10^{-26}\,\mathrm{m}^2$
σ_a^s	N/A	$2.011 \times 10^{-26}\,\mathrm{m}^2$
σ_e^p	N/A	$1.519 \times 10^{-26}\,\mathrm{m}^2$
σ_e^s	N/A	$5.412 \times 10^{-25}\,\mathrm{m}^2$

Figure 3.5 shows the pump and signal along the fibre and the gain levels of the two amplifiers. Similar to the incoherent simulations, the total signal gains at fibre output of the two amplifiers are comparable despite different output power. The growth of signal power and depletion of pump power are faster in the YDFA than in the FRA. However, contrary to the incoherent simulations, the difference between the gain for the target LP_{08} mode and the total signal mode is slightly larger in the FRA (0.84 dB) than in the YDFA (0.81 dB). The gain difference in the YDFA is much less than the 2.44 dB in the incoherent amplifier, while that in the FRA is higher than the 0.26 dB in the incoherent case.

For the YDFA, since mode coupling is ignored in the simulations, we attribute the difference to the mode competition due to the beating between the modes [7, 8]. To elaborate, take a two-mode amplifier with a dominant LP_{01} and weak LP_{11} mode as an example, the LP_{11} mode with polarization either parallel to or perpendicular to the LP_{01} mode, has higher local gain coefficient than the LP_{01} mode when the local population inversion is depleted. However, the LP_{01} mode interferes with the co-polarized LP_{11} mode constructively in one side and destructively in the other side, causing higher local gain in the destructively interfering side due to a less depleted upper state population. Thus, the difference in gain serves to equalize the power in the two sides, and mode decomposition shows that

this effect is equivalent to suppression of the LP_{11} mode. Therefore, LP_{11} can be either enhanced relative to LP_{01} when the two modes have $\pi/2$ relative phase (thus no interference) or suppressed when they are in phase and interfere [8]. This modal interference adds a small oscillation to the evolution of power ratio between the two modes along the fibre, with the oscillation period determined by the mode beat length. The overall trend of LP_{11} relative to LP_{01} is affected by their respective gain and the strength of modal interference. This effect is not limited to these modes but can occur between any strong mode and weak mode. In our case, the YDFA is highly multimode, and the modes are all co-polarized. The target LP_{08} mode will interfere and compete with the other modes, with a net effect of suppressing the growth of the unwanted modes. Therefore, the modal gain difference is not as drastic as in the incoherent simulations. For the FRA, modal interference also occurs between the co-polarized LP_{0m} mode and the LP_{1m} modes, creating an asymmetric transverse intensity profile. However, since Raman gain is independent of the local signal intensity, the altered signal intensity profile will not cause any gain competition effects like in the YDFA. The slightly larger gain difference between the total signal and the target mode in the coherent FRA than the incoherent FRA which is apparent from Figure 3.5(b) and Figure 3.1(b) may be due to the difference in the pump evolution between the two cases, but has not been investigated yet.
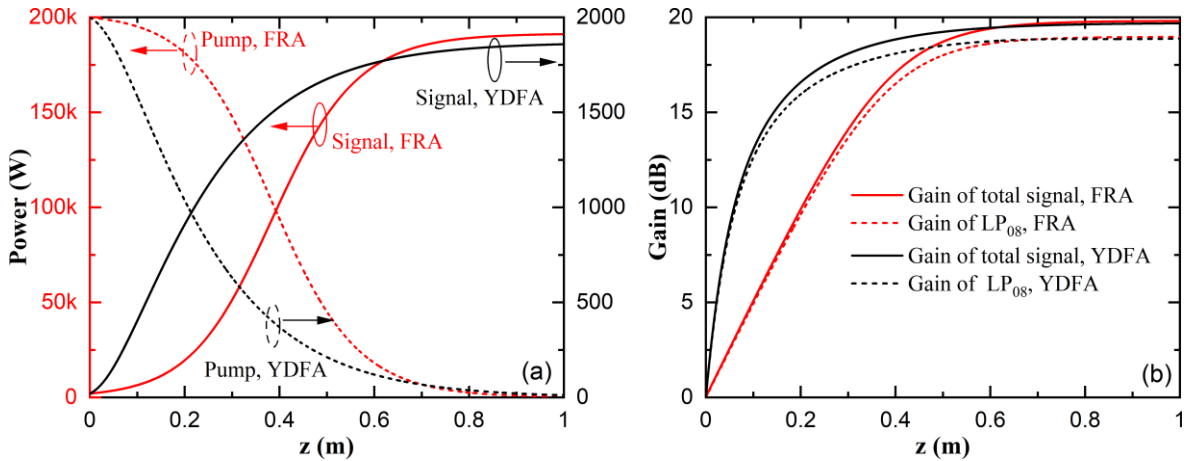
Figure 3.5: Comparisons of power and gain in the YDFA and the FRA in the coherent simulations. (a) Evolutions of pump (dashed curves) and signal (solid curves) power in the YDFA (black curves) and FRA (red curves). The power of YDFA and FRA are in different scales as indicated by the arrows; (b) The total signal gain (solid curves) and the gain for the target HOM (dashed curves) in the YDFA (black curves) and FRA (red curves).

As a result of the mode competitions, the purity of the LP_{08} mode in the two amplifiers are different from the incoherent simulation, as shown in Figure 3.6. The purity drops from 80% to 66.2% (0.82 dB drop) at the fibre output for the YDFA and to 65.7% (0.85 dB drop) for the FRA. In the YDFA, the purity drops quicker against the longitudinal distance than in the FRA in the first 10% of fibre length, but overall degrades slower as the signal power increases than the FRA. Compared to the incoherent results, when plotted against the normalized signal power, the mode purity in the FRA drops quickly first and then returns to a linear trend. For the YDFA, from Figure 3.6(a) the mode

purity of LP_{08} oscillates slowly along the fibre. From Figure 3.6(b), when plotted against the normalized signal power, the purity of LP_{08} in the YDFA drops quicker than in the FRA at low to medium signal power but recovers a bit at higher signal power. This is not explained by mere mode beating which can occur in both YDFA and FRA, but the competition between modes under gain saturation.
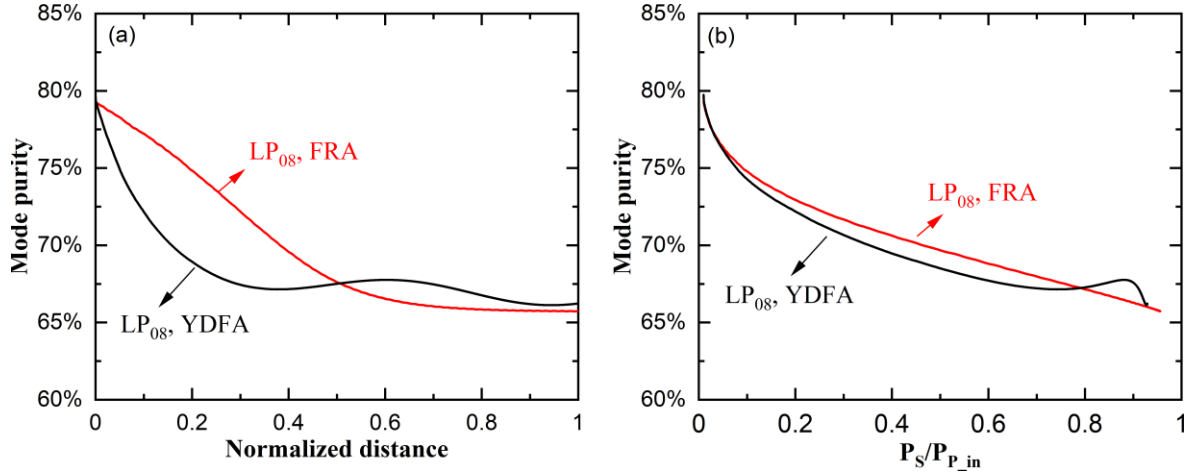
Figure 3.6: Mode purity of the target HOM in the coherent FRA (red curves) and YDFA (black curves) plotted against (a) normalized distance and (b) normalized signal power.

To further explore the effect of mode competition on the mode purity, I first increase the NA of the core from 0.2 to 0.25 while maintaining the core radium of 22 μm. The input pump and signal powers and the way they are distributed among the modes are unchanged. The mode purity at the fibre output is calculated for the core NA of 0.2, 0.22, 0.23 and 0.25. As the core NA increases, the number of signal modes increases and the initial power in each of the unwanted modes are reduced. Since the mode area and the pump intensity are essentially unchanged, the gain should be the same. Then I increase the core radius to 25 μm and repeat the simulation with the different NAs. The number of modes is further increased, and the pump intensity is overall reduced. The results for the two types of amplifiers are plotted in Figure 3.7. In general, the mode purities improve as the core NA increases. For a given NA, the mode purity is higher for an amplifier with a larger core. When plotted against the number of supported modes at the signal wavelength, the mode purity grows in an almost logarithmic rate. The curve of mode purity of the FRA is above the one of the YDFA, suggesting that for the same number of supported signal modes, the FRA has better purity preservation than the YDFA. In addition, in both the YDFA and the FRA, the mode purities are similar with similar number of signal modes, even though the core sizes are different. For instance, the mode purity of a FRA with 22 μm core radius and 0.25 core NA is 70.0%, and the purity of a FRA with 25 μm core radius and 0.22 core NA is 70.3%. In both amplifiers, the improvement of mode purity saturates as the number of modes becomes larger.
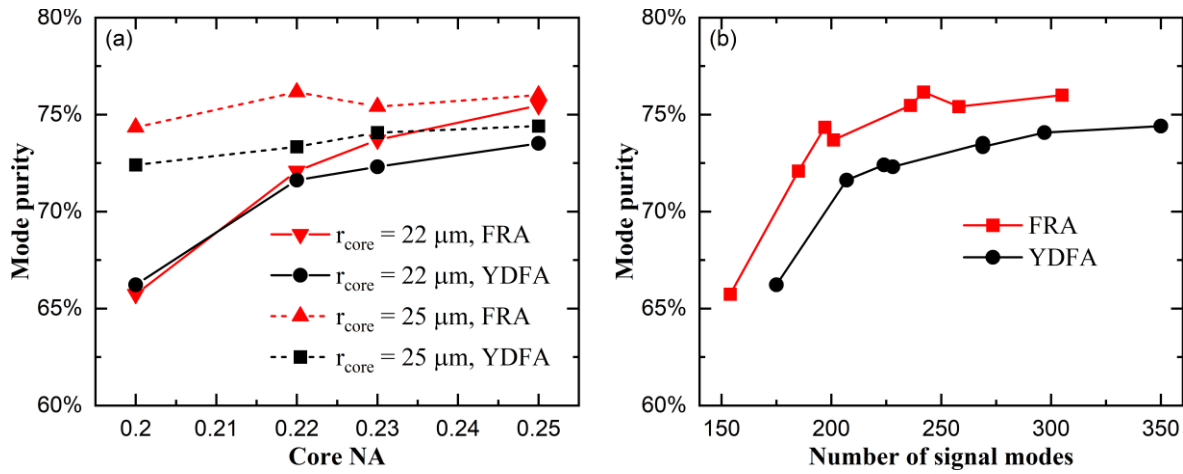
Figure 3.7: (a) Mode purity of the target HOM in the coherent YDFA and FRA with different core radii against the core NA. (b) Mode purity of the YDFA and FRA from (a) plotted against the number of signal modes supported in the fibre. The number of modes consider the cosine and sine variation of a mode but do not count the polarization multiplicity.

It is worth mentioning that if the modal power is evaluated with the amplitude from the mode solver, one can see that for both the YDFA and the FRA, the main culprit for the purity degradation is the LP_{07} mode, with power almost 1% of the target mode at the fibre output. At the fibre input, LP_{07} has the same power as the other unwanted modes. However, after ~50 µm propagation, the power in LP_{07} becomes several times higher than in the other unwanted modes. In addition, the oscillation of the mode purity in the YDFA plotted in Figure 3.6 is not seen if the power is evaluated with the amplitudes from the mode solver, despite a small difference between their evolutions of the power in the target mode. This is a result of the discrepancy between the mode field distribution from the mode solver and the BPM mode that I mentioned earlier. If evaluated with the BPM mode, there is not any dominant parasitic modes for both the YDFA and the FRA. Instead, results of both the YDFA and the FRA show that the strongest parasitic modes are usually the LP_{l1} modes. For instance, in the FRA with a core of 22 µm radius 0.2 NA, the top three parasitic modes at the fibre output are the LP_{31}, LP_{51} and LP_{71} modes, taking 0.64%, 0.61% and 0.59% of the total signal power, respectively. This agrees with the generally higher overlap of the LP_{l1} modes with the pump beam depleted mostly by the Bessel HOMs.

The simulation results in this chapter suggest that typical FRAs have better signal HOM preservation than the YDFAs when the pump and signal are both incoherent. On the other hand, for the coherent amplifiers, the FRAs still outperform the YDFA in purity preservation in most configurations, especially when the number of signal modes becomes larger, but with less advantage than in the incoherent case. This is expected. When the power in a parasitic mode is negligible, its effect on the gain saturation is negligible, whereby its phase and thus its coherence becomes irrelevant. Even if there is power in other parasitic modes, their phases are effectively random when averaged over a length with non-negligible Raman gain and can therefore be considered incoherent. Therefore, the benefit of the coherent gain competition in the YDFA is reduced when the parasitic power is

distributed over large number of parasitic modes. Amplifiers with either the pump or signal being coherent while the other being incoherent are not simulated, as it is not possible with the available software. Among these, the most interesting configuration is perhaps the one with a coherent signal and incoherent pump. For the YDFA, a coherent signal is likely to improve the purity preservation, thanks to the mode competition effect. For the FRA, current simulation results show that the purity degradation is less with incoherent pump and signal. Since the absence of local gain saturation is likely to make the signal coherence less important in the FRA, the performance of the FRA with coherent signal and incoherent pump is expected to be closer to the case of incoherent pump and signal. Again, these are hypothesis to be verified by further investigations. Practical fibre amplifiers are likely to have a partially spatially coherent signal with an incoherent pump. Therefore, the mode purity preservation performance of YDFAs and FRAs in real life is expected to sit between the cases of coherent and incoherent signal with an incoherent pump. Note also that mode-coupling is not considered in this analysis. However, fibre imperfections are likely to be more severe in YDFAs and will render mode-coupling significant in many cases.

Fibre modes carrying OAMMs are not investigated here, as BPM simulations of OAMMs are hindered by the use of square (or rectilinear) grids, which in general do not support OAMMs (there are no OAMMs among the BPM modes. Charge-1 OAMMs may be an exception since they can be decomposed into constituent modes that are rotated 90 degrees with respect to each other, just like the axes of a square grid. OAMMs of other charges can be decomposed into constituent modes with different relative rotation angles, but those modes will also have different rotation relative to the square grid and the corresponding BPM modes are therefore not degenerate.)

Strictly, OAMMs are vector modes, but they can still be approximately treated as linear combinations of degenerate scalar modes with 90-degree longitudinal phase difference between them. The purity of the LP-modes that correspond to the OAMMs in YDFAs and FRAs is expected to behave similarly to the purity of the Bessel HOMs, if any change in their relative phase is neglected. However, unlike the Bessel HOMs, the purity of an OAMM is affected by the relative ratio of power between the degenerate scalar modes that it corresponds to, which in turn corresponds to a change of power in the conjugate OAMM with the opposite charge. Since the degenerate modes are always coherent even if the linewidth is large (ignoring any anisotropic perturbations in the fibre), the impact of mode competition under gain saturation in the YDFA can be significant. In other words, the mode competition in the RE-doped fibre amplifiers may enhance a stronger OAMM and suppress the growth of a weaker parasitic OAMM with opposite charge. This effect can be further boosted by the identical intensity profiles of conjugate OAMMs and improve the purity of the target OAMM in YDFAs. Nevertheless, the net effect of mode competition is dependent on the parameters of the amplifier, and further simulation or experimental investigations are required to draw any conclusions.

3.4   Summary

In this chapter I presented the simulation results to compare the performance of typical YDFA and FRA in both incoherent and coherent regimes. For the incoherent amplifiers, as expected, the FRAs benefit from the non-local gain saturation, excelling over the YDFAs in signal mode purity preservation. For the coherent amplifiers, the mode competition can suppress the growth of a weaker parasitic modes and compensate for the mode-selective gain saturation. Depending on the amplifier parameters, the YDFAs can outperform the FRAs in purity preservation. However, for the same number of supported signal modes, FRAs still have better purity preservation than the YDFAs. In this thesis, the experiments focus is on FRAs where the signal and pump modes are mostly incoherent except for the degenerate OAMMs with opposite charges. FRAs may preserve the purity of the target mode in these amplifiers better than the YDFAs. Mode coupling is neglected in my simulations, which I expect can be more detrimental for YDFAs than for FRAs.

3.5   References

[1]   B. Crosignani, and P. Di Porto, "Coherence of an electromagnetic field propagating in a weakly guiding fiber," J. App. Phys. **44**, 4616 (1973).

[2]   C. R. Giles, and E. Desurvire, "Modeling erbium-doped fiber amplifiers," J. Lightwave Technol. **9**, 271 (1991).

[3]   Z. Jiang, and J. R. Marciante, "Impact of transverse spatial-hole burning on beam quality in large-mode-area Yb-doped fibers," J. Opt. Soc. Am. B **25**, 247 (2008).

[4]   J. Demas, L. Rishøj, and S. Ramachandran, "Free-space beam shaping for precise control and conversion of modes in optical fiber," Opt. Express **23**, 28531 (2015).

[5]   C. A. Codemard, J. K. Sahu, and J. Nilsson, "Tandem cladding-pumping for control of excess gain in ytterbium-doped fiber amplifiers," IEEE J. Quantum Electron. **46**, 1860 (2010).

[6]   M. D. Feit, and J. A. Fleck, "Computation of mode properties in optical fiber waveguides by a propagating beam method," Appl. Opt. **19**, 1154 (1980).

[7]   D. V. Vysotsky, and A. P. Napartovich, "Mode competition in steady-state optical waveguide amplifiers," J. Exp. Theor. Phys. **108**, 547 (2009).

[8]   A. V. Smith, and J. J. Smith, "Mode competition in high power fiber amplifiers," Opt. Express **19**, 11318 (2011).

Chapter 4   Fibre Raman amplifiers for high order Bessel modes

4.1   Introduction

Fibre Raman amplifiers (FRAs) are a versatile platform for wavelength-agile power scaling and brightness enhancement. As shown in Chapter 3, their unique gain mechanism that introduces little purity degradation under gain saturation make them attractive for power-scaling through amplification of a single mode in a multimode fibre. In this chapter, I report our experiments with four different FRAs for Bessel higher order modes (HOMs) and analyse their performance in terms of Raman gain, pump depletion, brightness enhancement and mode purity. In section 4.2, a proof-of-concept configuration which uses a pulsed commercial YDFL master oscillator is introduced. Then an upgraded amplifier setup that aims to resolve some shortcomings in the first setup and improve its performance is described in section 4.3. In section 4.4, an efficient low-brightness-pumped FRA for HOM based on the upgraded amplifier and its performance are discussed. Finally, I report our preliminary results with a QCW FRA for HOM with spectrally combined diode laser pumping in section 4.5. The results are summarized in section 4.6.

4.2   Pulsed fibre Raman amplifier for LP$_{08}$ mode with multimode pumping in a 9-m large mode area fibre

As a starting point, I describe a relatively straightforward amplifier configuration where a single master oscillator produces pulses at 1060 nm for both Raman pump and seed generation. The gain fibre is kept relatively short, at 9 m, to avoid potential excessive mode coupling while still allowing sufficient Raman gain with only 10~20 kW of pump peak power. A physical silica axicon is used for mode conversion from LP$_{01}$ to LP$_{08}$. This simple configuration, though lacking tunability, serves well for a proof-of-concept demonstration of FRA for HOM.

4.2.1 Experimental setup
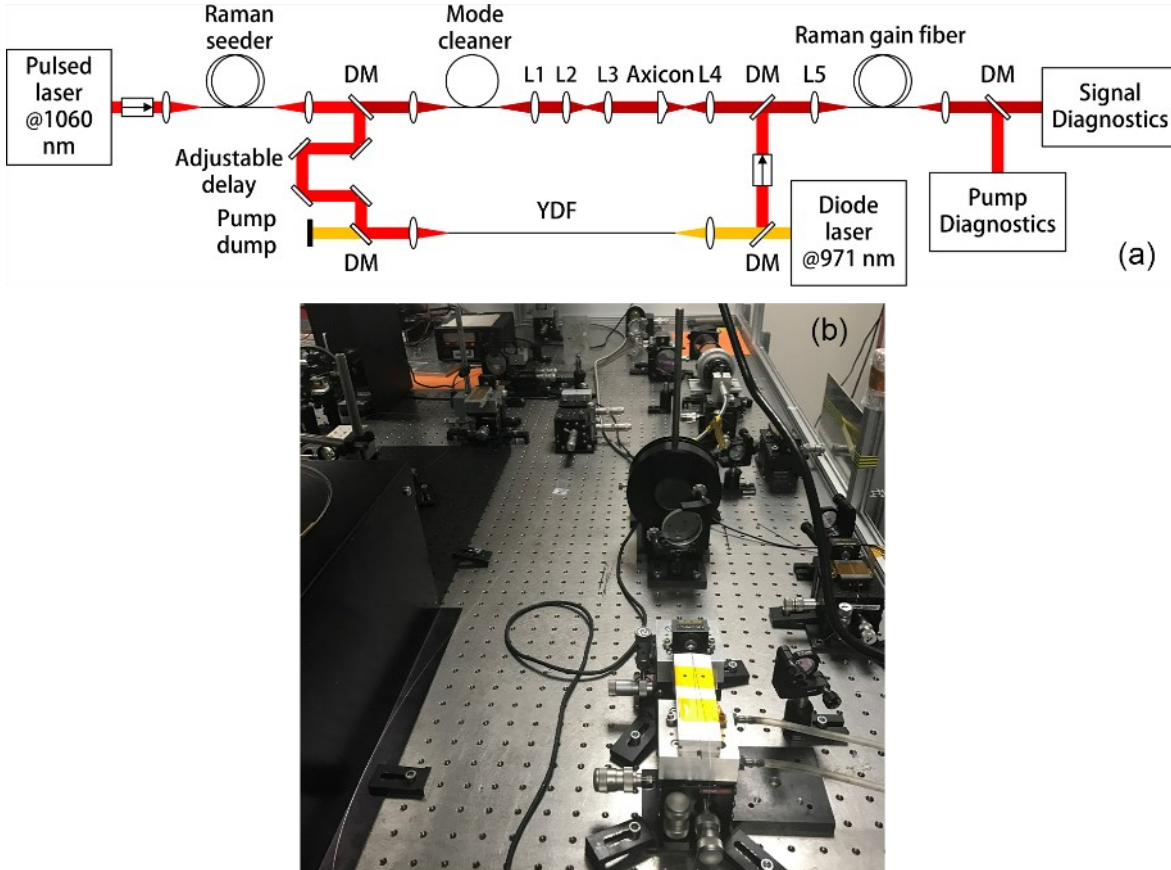
Figure 4.1: (a) Schematic of the experimental setup for LP$_{08}$ mode Raman amplification. (b) Picture of the experimental setup without the delay line. The Raman pump source and the diagnostics are not shown in the picture.

The schematic of the experimental setup and a photo of the Raman generation and mode conversion part are shown in Figure 4.1. A commercial YDFL (G3, SPI Lasers) emitting 1060-nm, 60-ns pulses at 4 kHz serves as the master oscillator. The YDFL has an output collimator and the output beam has a M^2 value of ~3. The output pulses are sent to a 30-m long Ge-doped silica fibre (Freelight, Pirelli) with about 35% launch efficiency. The launched pulses have an average power of ~0.3 W and are partly converted to the first order Stokes at 1115 nm via SRS. The converted 1115 nm pulses have a FWHM duration of ~25 ns. A dichroic mirror (DM) which is HR (high reflection) at 1060 nm and HT (high transmission) at 1115 nm separates the 1115 nm pulses from the residual 1060-nm pulses. The 1115-nm pulses are launched into a 3-m single mode fibre (1060-XP, Nufern) to achieve a clean fundamental mode. The output is then collimated by an aspheric lens (L1, f = 8 mm), expanded by a two-lens telescope (L2, f = 100 mm and L3, f = 250 mm), and converted to a Bessel beam by a UV-fused-silica axicon (AX251-C, Thorlabs). The axicon is labelled to have an angle of 1° (apex angle 179°) and converts the incident Gaussian beam to a Bessel beam [1]. At the focal plane of the axicon, the converted beam becomes a Bessel-Gaussian beam that should have a spatial frequency matching the target HOM in the Raman gain fibre after appropriate magnification, which ideally requires the

knowledge of the propagation constant of the target HOM. Instead, here it is assumed that for proper coupling, the location of the mth zero of the truncated Bessel function $J_0^{(m)}$, where m is the radial order of the target HOM LP$_{0m}$, is matching the fibre core radius. From [1], the axicon angle is related to the target HOM by the following equation:

$$\alpha = \frac{J_0^{(m)}}{k_0(n-1)R_c M} , \qquad (4.1)$$

where $J_0^{(m)}$ is the mth zero of the truncated 1st order Bessel function, k_0 is the wavenumber in vacuum, n is the refractive index of the axicon, R_c is the core radius of the RGF and M is the magnification. The focal length of the axicon is given by:

$$f_{axicon} = \frac{0.64W_0}{(n-1)\alpha} , \qquad (4.2)$$

where W_0 is the amplitude width of the incident Gaussian beam. A pair of lenses (L4 and L5) then image the beam at the focal plane of the axicon to the facet of the Raman gain fibre to excite the target HOM. The arrangement for HOM excitation is depicted in Figure 4.2. For a given axicon angle, the radial order m of the excited LP$_{0m}$ mode in the 50-µm fibre is determined by the magnification. In practice, the estimated locations of the optics are marked on the optical table. The incident signal beam is first collimated, expanded by L2 and L3 and kept straight at low power. A silicon camera is fixed slightly further away from the estimated focal plane of the axicon and records the location of the incident Gaussian beam. The axicon is mounted on a 3-axis translation stage and placed in the beam path with the beam roughly crossing the centre of the axicon. The transverse location of the axicon is then fine-tuned via the translation stage until the centre of the generated pattern (shown as the right inset in Figure 4.2) overlaps with the marked location of the incident signal beam. The camera is then moved close to the estimated focal plane of L4 and records the location of the centre of the signal beam without inserting L4. After this, L4 is mounted on a 3-axis translation stage, inserted in the beam path, and has its XY position fine-tuned till the centre of the captured pattern (shown as the left inset in Figure 4.2) and the marked location overlap. The DM for combining the pump and signal beam is then inserted before placing the final aspheric lens L5. Again, the transverse position of L5 is adjusted by overlapping the signal beam captured by the fixed camera in the beam path with and without the optics. These procedures can roughly ensure that the beam path passes the centre of the optics and is a straight line. The longitudinal position of L5 is coarsely adjusted so that the output power of the RGF is maximized. The camera is then moved to capture the output of the RGF which is imaged by an aspheric lens for final adjustments. The incident signal beam is then walked in the horizontal and vertical direction by first adjusting the horizontal or vertical position of L4 and then L5. Beam walking is repeated till the output of the RGF shows the intensity profile of the target HOM with clean edges and good contrast between the rings. In addition, by changing the

longitudinal position of the axicon and then repeating the beam walking with L4 and L5, the excited HOM can be changed. However, usually only one or two Bessel HOMs show best power launch efficiency and contrast in the intensity pattern.
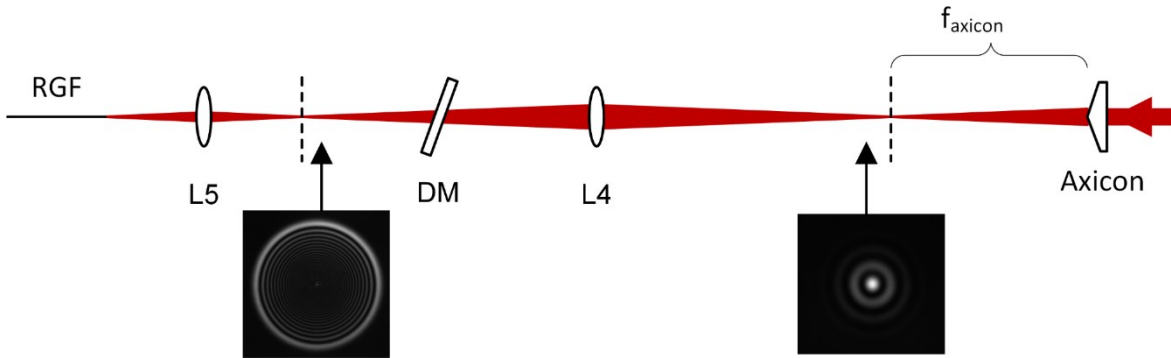
Figure 4.2: Illustration for HOM launching arrangement with the axicon. Dashed lines denote object and image planes of L4. Insets show the intensity profiles of the signal beam captured by a silicon camera near the focal plane of the axion (right inset) and L4 (left inset).

In this experiment, we compare the intensity profiles of the transmitted mode and look for the mode with the best purity as we use different combinations of the launching lens pair. We settle with a magnification of ~31 (L4, f = 250 mm and L5, f = 8 mm) and excite the LP_{08} mode, which yields the best transmitted mode purity among the several Bessel modes that we tried.

The residual 1060-nm pulses from the Ge-doped fibre are reflected by another DM which is HT at 1115 nm (not shown in Figure 4.1) to minimize the unwanted downstream Stokes light. A delay line that consists of four broadband mirrors temporally synchronizes the 1060-nm pulses and the 1115-nm pulses when they reach the Raman gain fibre. The 1060-nm pulses are then launched into the core of a 2-m long multimode YDF. The YDF has a core diameter of 50 μm and NA of 0.2 and boosts the power of the 1060-nm pulses which are later used as the Raman pump. The end facets of the YDF are 8° angle polished to avoid parasitic oscillation. The YDF's preform was fabricated in Nanyang Technological University through conventional modified chemical vapor deposition process and then drawn to a double-clad fibre with low-index coating. A CW diode laser (LDL 80-500, Laserline) cladding-pumps the YDF in the backward direction and the boosted 1060-nm pulses reach an average power of ~6.4 W and pulse energy of ~1.6 mJ. The amplified 1060-nm beam has a spectral linewidth of ~7 nm, as shown in Figure 4.3. These pulses are recombined with the Raman seed by another DM and launched into the core of the Raman gain fibre by lens L5 with a launch efficiency of ~65%.
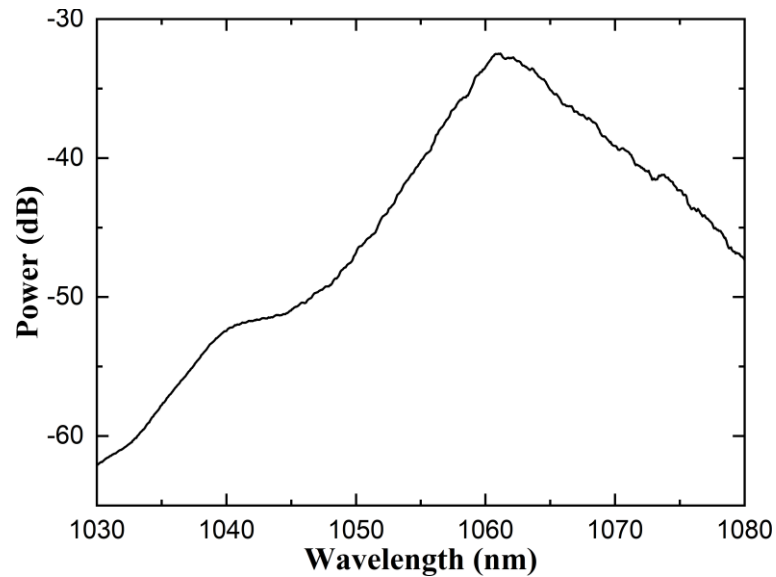
Figure 4.3: Spectrum of the 1060-nm pump beam from YDFA at ~18 kW output peak power. OSA resolution 2 nm.

The Raman gain fibre is a 9-m long commercial step-index fibre (FG050LGA, Thorlabs) with a pure silica core of 50 μm diameter and 0.22 NA. It has a beam parameter product (BPP) that matches the 50-μm YDF and we are able to launch the pump with efficiency over 60%. The pump launch is not optimized for efficiency as the optics and their positions are prioritized for signal launch. Although we did not measure the refractive index profile of the RGF, we believe the fibre perturbations are small based on its pure silica composition and literature reports [1]. The fibre has a V number of 31 at 1115 nm and supports more than 400 modes including degenerate modes with different polarizations. The coupling between the target LP_{08} mode and its nearest-neighbour antisymmetric mode LP_{18}, which usually governs the stability of HOMs in the fibre [2], is expected to be small in the RGF. At 1115 nm, the effective index difference between LP_{08} and LP_{18}, calculated by a scalar mode solver (RP Fibre Power), is 1.252×10^{-3} in comparison to an effective index splitting of 1.452×10^{-4} between LP_{01} and LP_{11}. Therefore, we expect increased stability of LP_{08} over the fundamental mode in this fibre. The loss of the RGF at ~1.1 μm wavelength is reported to ~2.7 dB/km and is negligible for a length of 9 m.

In the experiment, 1115-nm seed pulses with ~50 mW average power is generated in the Freelight fibre and ~15 mW is incident to the RGF after passing through the mode-cleaning passive fibre and the optics. The launched seed beam has an average power of ~7 mW and a pulse energy of 1.75 μJ. The launched pump beam has an average power of up to 4.16 W with 1.04 mJ pulse energy and 21.5 kW peak power. The output of the RGF is collimated by an aspheric lens (f = 6.24 mm), separated into pump and signal beam by a DM and sent to their respective diagnostics which include a thermal power meter, a 12.5 GHz InGaAs detector (ET-3500, EOT) connected to a 6-GHz oscilloscope (Infiniium 54855A, Agilent), an optical spectrum analyser (AQ6317B, Ando) and a silicon camera (BA CAM, HAAS Laser). The temporal traces of the incident signal and pump pulses

are also monitored by 12.5 GHz InGaAs detectors by measuring reflections from inserted wedge prisms (not shown in Figure 4.1).

4.2.2   Results and analysis
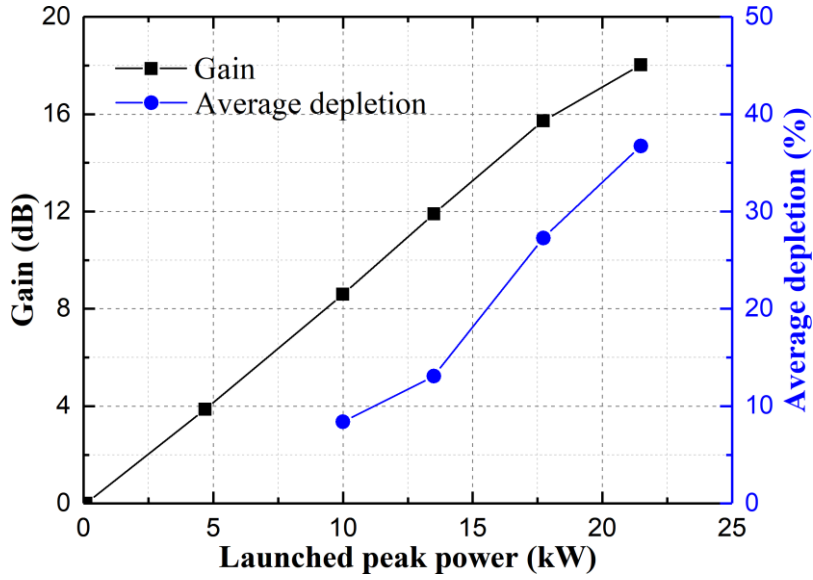
Figure 4.4: Measured average power gain and weighted pump depletion versus launched peak pump power.

Figure 4.4 shows the measured average power gain and the average pump depletion versus launched pump peak power. The average power is measured with the thermal power meter and the launched pump peak power is calculated from the throughput pump power with negligible fibre loss and the measured pump pulse duration. The pump pulse duration is the part where pump and signal pulses overlap (shown between the dashed line in Figure 4.5(a)). This excludes parts of the pump pulse that do not result in any conversion. Note also that most of the conversion happens between 0 and 10 ns. A maximum of 18 dB gain is achieved, with 115 µJ of amplified signal pulse energy and 4.6 kW peak power. The average pump depletion $\eta_{depletion}$ is calculated by weighting the instantaneous depletion $\eta_P(t) = (P_P^{in}(t) - P_P^{out}(t)) / P_P^{in}(t)$ with the instantaneous signal output power:

$$\eta_{depletion} = \frac{\int P_S^{out}(t)\eta_P(t)dt}{\int P_S^{out}(t)dt}, \tag{4.3}$$

where P_P^{in}, P_P^{out}, P_S^{out} are input pump, output pump, and output signal power, respectively. These are from the temporal shapes of pump and signal pulses, which are shown in Figure 4.5. At 18 dB gain, the average pump depletion reaches 36.7%. From Figure 4.4, the average power gain increases almost linearly with the launched pump peak power up to around 16 dB gain for 17.7 kW, with a slope of 0.9 dB/kW. The Raman gain coefficient calculated from the slope value and the core area of 1960 µm² is 45 fm/W, which is in good agreement with the theoretical value of ~47 fm/W for pure

silica with a signal at 1115 nm and unpolarized pumping at 1060 nm. Beyond 17.7 kW pump peak power, the Raman gain sees a roll-off due to pump depletion. Further power scaling was not attempted as parasitic oscillation emerged in the YDF and destabilized the pump beam.
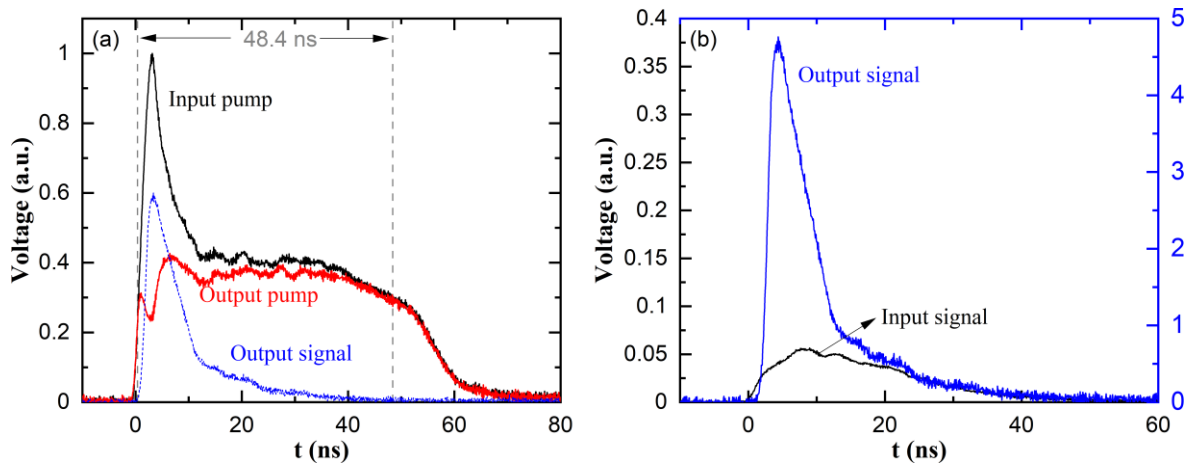
Figure 4.5: (a) Pump pulse at input and output of Raman gain fibre at 18 dB signal gain. The output signal is also shown but temporally shifted. Dashed line shows temporally overlapped region between pump and signal pulses. (b) Signal pulse at input and output of Raman gain fibre at 16 dB gain. Scales are different for input (left) and output.

As shown in Figure 4.5(a), the incident pump pulse has a sharp peak at the beginning with a maximum instantaneous power of twice the average power across the pulse. The transmitted pump pulse shape shows that most pump depletion occurs at the peak with a 58% drop in energy, and the peak at 3 ns drops by 76%. However, the overall weighted pump depletion is only 36.7% as the narrow peak of ~5 ns in the leading edge of the pump, which overlaps well with the signal (shown in Figure 4.5(b)) and provides Raman gain, only contains ~15% of the pulse energy, while the remainder of the pump pulse whose instantaneous power is much lower sees only minor depletion. This is due to the pump pulse shape from the master oscillator which is designed for material processing as well as the narrow peak coming from the partial Raman conversion of the 1060-nm master pulses. As shown in Figure 4.6, the output 1060-nm pulse from the YDFA without 970-nm pumping has a small peak followed by a dip in the leading part. When pumped, the first small peak sees much higher gain than the remainder of the pulse and creates the narrow peak in the Raman pump pulse shown in Figure 4.5(a).
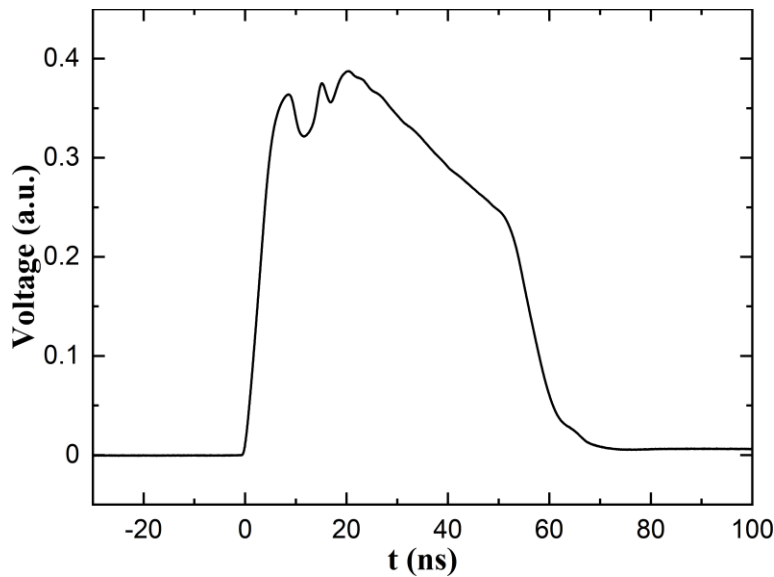
Figure 4.6: Transmitted 1060-nm pulse from YDFA without 970-nm pump.

Figure 4.7 shows the measured spectra of the amplified Raman signal at various gain levels, where 0 dB gain corresponds to the input spectrum. The spectra are measured with an OSA resolution of 0.5 nm. The 3 dB linewidth of the input signal is ~8.6 nm and the linewidth of the amplified signal at 18 dB gain is ~8.1 nm. There is an extended tail at around 1130 nm, however the fraction of power beyond 1130 nm is 10 dB less than the power at 1115 nm and there has not been any significant power corresponding to the second order Stoke observed in the experiment.
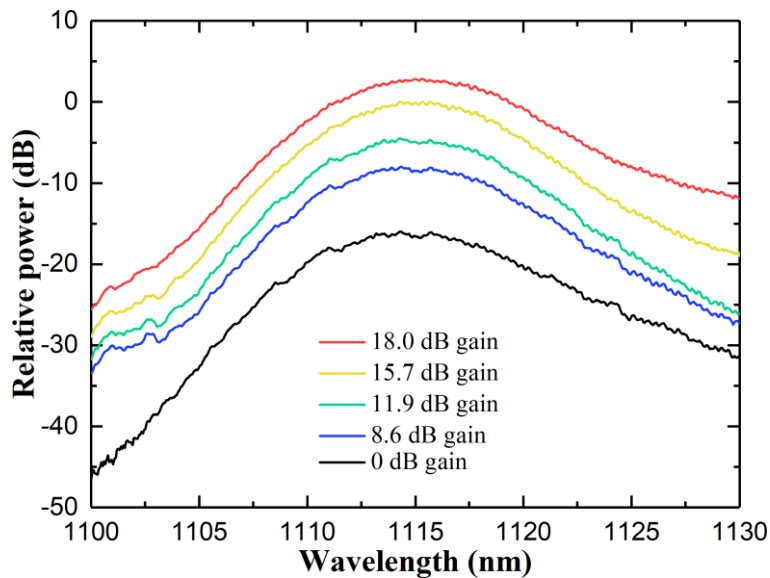
Figure 4.7: Measured spectra of amplified signal at different gain levels. OSA resolution 0.5 nm.

The intensity profiles of the output signal beams at 0 dB, 16 dB and 18 dB gain are shown in Figure 4.8(a) to (c). These are plotted in log scale and normalized to maximum intensity for better visibility. The intensities along the line that crosses the centre of the beams, also in log scale and normalized, are plotted in Figure 4.8(d). The ideal LP_{08} mode has seven non-zero rings around a central peak with similar energy in each ring and separated by null rings. The non-zero minima observed in the profiles

indicate an imperfect LP_{08} mode even without pumping. This could be a result of imperfect mode launch that excites unwanted modes and / or scattering into neighbouring modes. As the gain increases, further mode degradation is observed. According to the simulations in the previous chapter, such further degradation is not explained by mode-selective gain saturation, especially when the gain saturation is not high. In our report in [3] we attribute this to thermal effects that deteriorate the alignment and signal launch. In later experiments using Raman seed and pump with narrower linewidth, we improved the purity of the signal mode, although the performance of the axicon is not expected to alter within a few nanometres of wavelength.
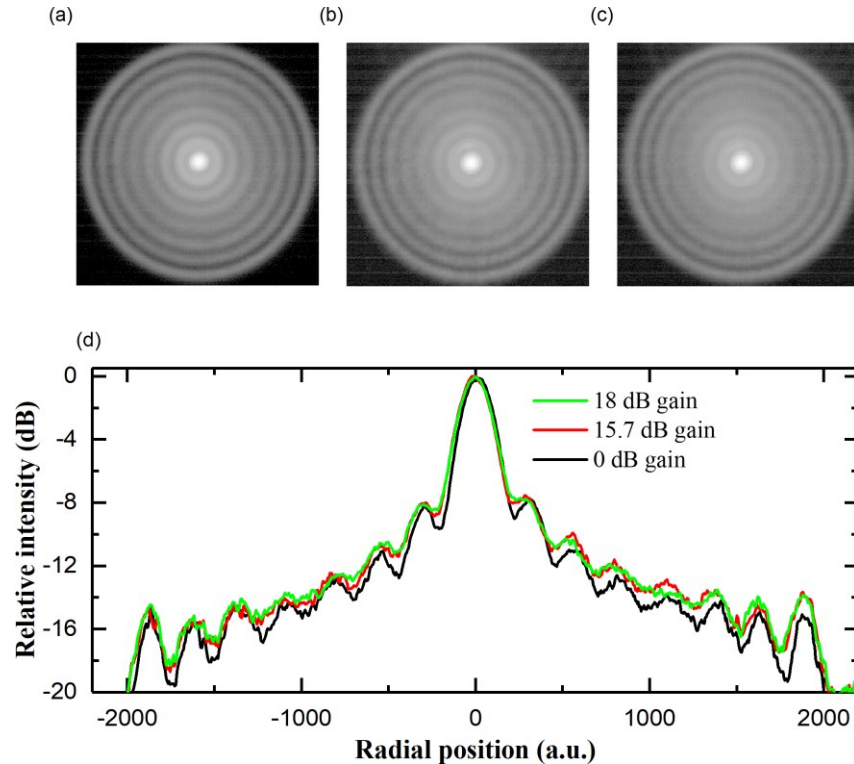
Figure 4.8: Transverse intensity distributions and line profiles of the signal output beams. Images of the intensity distribution at gain levels of (a) 0 dB, (b) 15.7 dB and (c) 18 dB. The greyscale is in log scale and normalized to enhance contrast. The bright spot in the centre corresponds to maximum intensity. (d) Normalized intensity line profiles (in log scale) for different gain values.

Further investigations with quantitative analysis of the modal content may help to clarify the extent of such degradation which may help in identifying the culprits. Various techniques have been reported to evaluate the modal content in multimode fibres. For instance, one can correlate the measured fibre output with the known eigenfunctions of the fibre [4, 5]. Such knowledge of the fibre is not always available or accurate enough to determine the relative weight of each mode. Alternatively, there are interferometric approaches such as spatially and spectrally (S^2) resolved imaging [6], cross-correlated (C^2) imaging [7] and cross-correlated imaging in the frequency domain (fC^2) [8]. However, fC^2 are not applicable to broadband sources we use in the experiments, and C^2 requires dispersion matching between the arms of the interferometer which is not trivial for HOMs in LMA fibre. We are able to coarsely resolve the modal content of the Raman gain fibre when

launched with a Gaussian beam with the S^2 method and a broadband source. However, the S^2 method requires a dominant mode as a reference mode before the content of the weaker modes can be determined. In our case, when the fibre is launched with a Bessel HOM, the dominant mode is the target HOM whose modal weight is to be determined. To the best of my knowledge, there is yet a well acknowledged method reported for quantitative modal content analysis for the broadband Bessel HOM and such analysis has not been pursued in this thesis.

The brightness enhancement is typically evaluated as the ratio between the brightness of the output signal and the incident pump. Here we estimate brightness enhancement from the change of power in each pump or signal mode. The exact power distributions among the pump or signal modes are unknown. However, from the measured intensity profile of the output signal, we assume most signal power in the target HOM LP_{08}. The power in the pump modes can be estimated from the measured beam quality (M^2 value), which however is not measured in this experiment. I hence estimate the power in each pump mode from the measured pump power and the number of supported modes in the YDF that generates the pump. The V-number of the YDF is 25.3 at 1060 nm and the number of supported modes including polarization multiplicity is approximately 320. At 18 dB amplifier gain, the peak power in each pump mode is then evaluated to ~67.2 W. Note that this value can be much lower than the actual value depending on how the pump modes are excited in the YDF. I also estimate 80% of the 4.6 kW signal peak power in the target signal mode LP_{08} which include two degenerate modes with orthogonal polarizations, each with a peak power of 1.84 kW at 18 dB gain. The increase of power per mode from pump to signal is thus ~14 dB, although this can be an overestimated value. A brightness enhancement of at least 10 dB requires that no less than 40% (–4 dB) of the modes are excited.

This was, to the best of my knowledge, the first experimental demonstration of a fibre Raman amplifier for a high order Bessel mode. A multimode YDF pump source is used to pump the 9-m long 50-µm diameter core commercial step-index silica fibre. The signal LP_{08} mode is largely preserved throughout the amplification, with only minor degradation. However, it remains to be confirmed experimentally that the purity is preserved in FRA when the pump conversion is high, which is our primary objective. Additionally, in our experiment, the pump pulse shape is not favourable for efficient Raman conversion. To resolve this issue, a pump source with more flexible control over the pulse shape and duration is needed. In addition, the current master oscillator has an emission linewidth of ~5 nm, and the incident pump beam has a linewidth of ~7 nm, as shown in Figure 4.3. pump and seed sources with narrower linewidth will help to isolate the causes of purity degradation.

4.3 Nanosecond pulsed fibre Raman amplifier for LP$_{05}$ mode with multimode pumping from YDF MOPA in a 10-m large mode area fibre

In the previous experiment I have demonstrated Raman amplification of a Bessel HOM in a 9-m long 50-µm core step index silica with multimode pumping. The maximum Raman gain for the average signal power is 18 dB with a weighted pump depletion of 36.7%. The signal mode purity is considered well preserved throughout amplification. However, further power scaling is hampered by parasitic oscillation in the pump source when I increase the pump power. The pump depletion is also limited by the non-ideal pump pulse shape which has a poor overlap with the signal pulse. To resolve these issues, we built another FRA for HOM with updated pump and seed sources. The Raman pump now comes from a diode-seeded YDF MOPA which consists of three amplifiers. The Raman seed is now in two configurations, one is a diode-seeded NDFA which generates Raman Stokes via SRS in a passive fibre, the other is a Raman pre-amplifier that boosts the power of a diode at the Stokes wavelength. The former configuration is adopted in this section and the latter in the next section. Both the pump and seed source now allow flexible control over the pulse duration down to a few nanoseconds and repetition rate from a few kilohertz to hundreds of kilohertz. An important difference is the short pump pulse duration which is expected to greatly reduce the parasitic effects from fibre facet reflections. The pump source is also capable of pulse shape control and wavelength tuning over a few nanometres around 1060-nm. A liquid-crystal-on-silicon (LCOS) spatial light modulator (SLM) is also incorporated as a mode converter that allows convenient selection of the signal mode and higher purity of the converted mode than an axicon.

Fibre MOPAs can be versatile sources that offer flexible spectral and temporal control while allowing high power output and beam quality. However, the MOPA source in the previous experiment had limited tunability in the master oscillator. Therefore, it is replaced with a pulsed YDF MOPA that has a directly modulated seed and multiple amplifier stages with better tunability. The MOPA was designed and built for a different project and therefore modified to meet the requirements of the present experiment.

4.3.1 Experimental setup
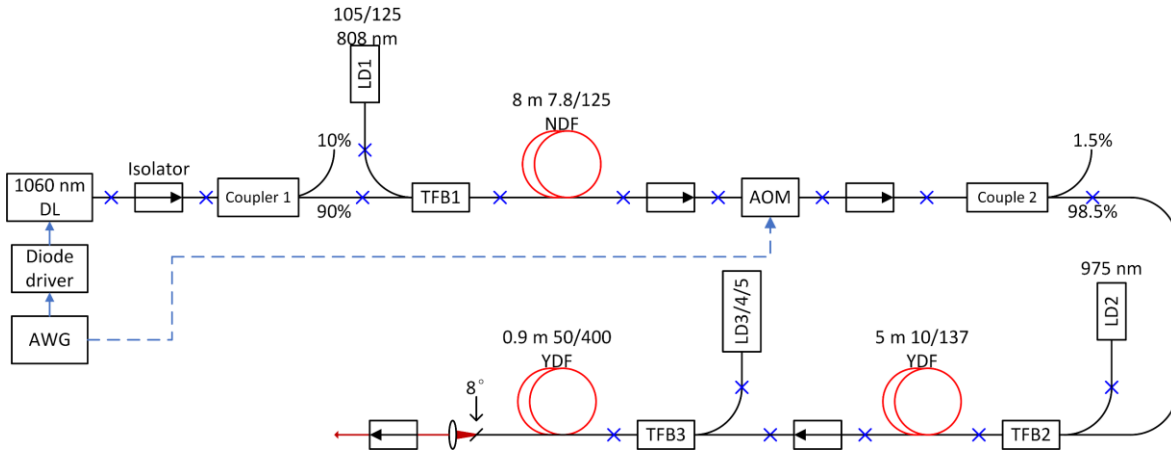
Figure 4.9: Schematic of the Raman pump source for the LP_{05} mode Raman amplification.

The schematic of the pump MOPA is shown in Fig 4.8. The seed source is a Fabry-Perot diode laser (LC96A1060-20A, Oclaro) driven by a diode driver (BFS-VRM 03 HP, Picolas). The 3-dB linewidth becomes ~3.7 nm. The drive current follows the signal from a 4 GSa/s, 729-MHz bandwidth arbitrary waveform generator (AWG710, Tektronix), connected to the diode driver. The diode emits at ~1060 nm and the wavelength can be tuned from 1055 nm to 1065 nm by changing the temperature of the diode. Its maximum average power when operating CW is 400 mW while the maximum peak power is 1.3 W when pulsed. In our experiment, the diode is driven to emit pulses with a duration of 5 ns with 15 kHz pulse repetition rate and 1 W peak power. The seed is protected by two cascaded polarization-insensitive (PI) isolators (only one is shown in Figure 4.9). A 10% tap coupler is spliced for seed light monitoring. The first amplifier consists of an 8-m long NDF with a 7.8 μm diameter core that is cladding pumped by a CW 808 nm laser diode. The NDF has a circular cladding which is not ideal for pump absorption. Therefore, it is bent with a tight radius of 2~3 cm and pressed to improve the pump absorption to a sufficient level. The seed and pump are combined with a (2+1)×1 tapered fibre bundle (TFB). The output of the NDFA then passes a PI isolator and is amplitude-modulated by a fibre coupled acousto-optic modulator (AOM, Fibre-Q, G&H). The AOM is set to transmit for a window of 60 ns that is synchronized with the seed to reduce energy between the pulses. The AWG that drives the seed diode also drives the AOM and controls the transmission window. Another PI isolator is spliced after the AOM to improve isolation between stages. A 1.5% tap coupler is used to monitor the output of the first amplifier. The second amplifier uses a 5-m long double clad YDF with a core diameter of 10 μm as the gain fibre, which has a cladding pump absorption of ~6 dB/m at 975 nm and is pumped by a 975 nm wavelength-stabilized diode laser (PLD-975-70-WS, IPG). The seed and pump are combined by a (6+1)×1 TFB. The output of the second amplifier passes another PI isolator and reaches the final amplifier. The gain fibre of the final amplifier is a 0.9 m double-clad YDF with a core of 50 μm diameter and 0.13 NA, with end facet polished with an angle of ~8° to prevent reflection at the fibre facet from going back into the fibre core. The pump comes from three 105/125 μm wavelength stabilized diode lasers (PLD-975-70-WS, IPG), and is combined

with the signal by a (6+1)×1 TFB. The output beam from the final amplifier is collimated by an aspheric lens (f = 11 mm) and passes a final free space PI isolator. At full power, the M^2 value of the pump beam is measured to ~7.
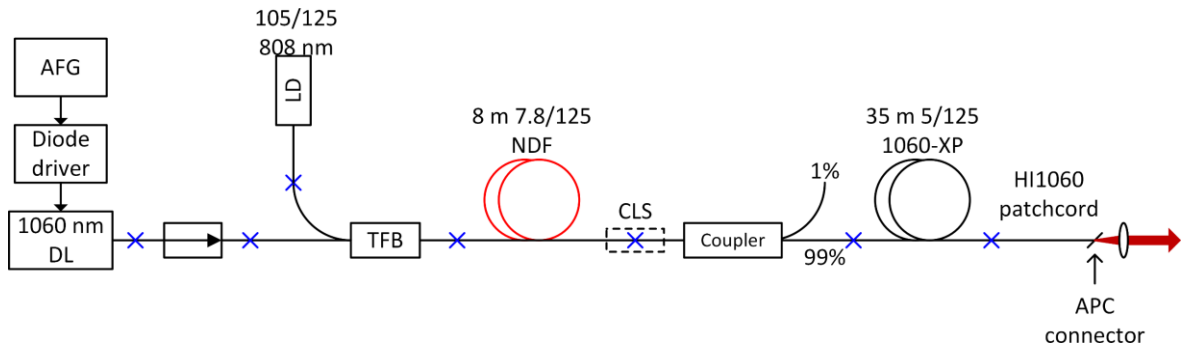
Figure 4.10: Schematic of the Raman seed source for the LP_{05} mode Raman amplification.

The Raman seed source comprises a diode-seeded NDFA that is converted to Raman Stokes via SRS, as shown in Figure 4.10. The seeding diode is the same type as the one used in the pump MOPA and is driven by a diode driver (LDP-V 03-100, Picolas) connected to a pulse generator (LDP-AV 40-70, Picolas), which is triggered by a 160-MHz bandwidth arbitrary function generator (AFG) (Model 4065, BK Precision). The AFG is synchronized with the AWG for the pump MOPA. The seed diode laser emits 1060-nm pulses with 2-ns duration and 1 W of peak power. An NDFA that is similar to the one in the pump MOPA boosts the seed pulse to a peak power of ~400 W with 1.2 μJ energy. At the splice point of the NDF, the unabsorbed pump light is removed by a homemade cladding light stripper (CLS). A 1% tap coupler is used to monitor the output of the NDFA. The 1060-nm pulses are then partly converted to Raman Stokes light at 1114 nm in a 35-m long single mode passive fibre (1060-XP, Nufern) via SRS. The length was optimized for efficient conversion into the 1st order Stokes and low amount of higher order Stokes. The converted Stokes light, as a result of the SRS building from quantum noise, has a linewidth of ~11 nm. A single mode fibre patchcord with an angled physical contact (APC) output connector is spliced to the passive fibre to suppress reflection into the fibre core. The output beam is then collimated by an aspheric lens (f = 8 mm).
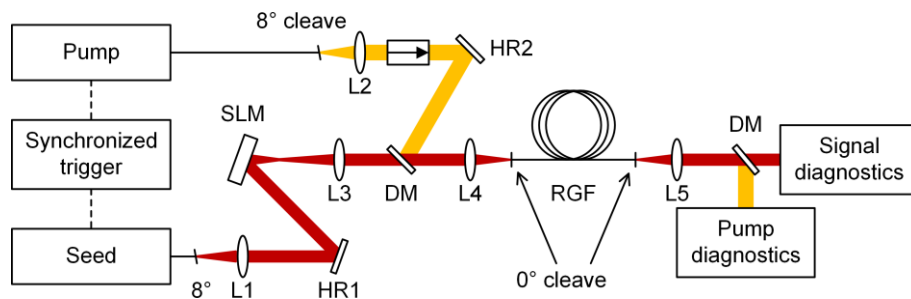
Figure 4.11: Schematic of the experimental setup for the LP_{05} mode Raman amplification.

We first attempt Raman amplification of a Bessel HOM LP_{05} in a 10-m in-house pulled 50-μm core step index silica fibre. The experimental setup of the main FRA is shown in Figure 4.11. The AFG that drives the diode in the seed also triggers the AWG for the pump and thus enables synchronization

for both beams. The seed is converted to a Bessel beam by a SLM with holograms incorporating the phase profile of an axicon and a diffraction grating. The SLM is hence effectively an axicon but without the rounded tip, which is a common imperfection of a physical axicon. A pair of lenses L3 (f = 200 mm) and L4 (aspheric, f = 8 mm) image the Bessel-Gauss beam at the focal plane of the SLM to the facet of the RGF. A DM combines the pump and seed beam. L4 also launches the pump into the core of the RGF. The temporal overlap between the pump and seed pulses is tuned by the trigger to maximize the average-power gain. The RGF is 10-m long, and has a pure silica core with 50 μm diameter and 0.227 NA. It is pulled in-house from a commercial preform (Fluosil Preform SWS6.95/SWU1.4, Heraeus). The measured refractive index profile is shown in Figure 4.12. A fluorine doped trench with reduced refractive index defines the core region. The measured background losses of the RGF at 1060 nm and 1114 nm are both ~0.8 dB/km and are negligible for 10 m. The output beam is collimated by an aspheric lens (f = 8 mm) and separated into a 1060-nm pump arm and a 1114-nm signal arm for their respective diagnostics. The diagnostics include a thermal power meter for the pump, a Ge power sensor for the signal, two 12.5 GHz InGaAs detectors (ET-3500, EOT), a 6-GHz oscilloscope (Infiniium 54855A, Agilent), an optical spectrum analyser (AQ6317B, Ando), and a silicon camera (DCC3240M, Thorlabs) with 12-bit resolution. The pump and signal beams that go into some of the diagnostic devices are attenuated by reflecting from silica wedges and the signal beam incident to the camera is additionally attenuated with a reflective variable neutral density filter (wedges and filter not shown in Figure 4.11).
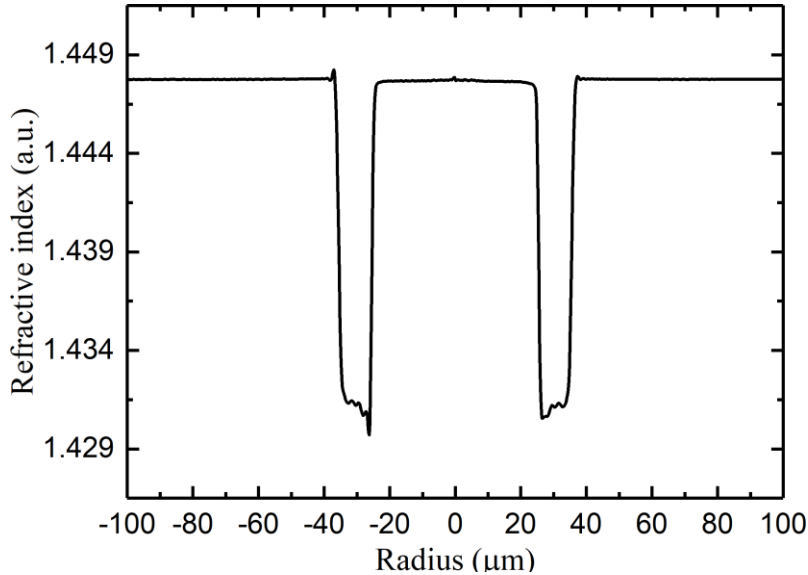
Figure 4.12: Measured refractive index profile of the Raman gain fibre with a 50-μm diameter core.

The SLM used in the experiment is a phase-only LCOS SLM that applies local phase modulation to the wavefront of the incident light, which greatly adds to the flexibility of controlling the signal mode excitation. To convert the incident Gaussian beam to a Bessel beam, the phase structure of an axicon is displayed on the SLM. A blazed grating is also added to the phase structure to separate the modulated beam from the specular reflection of the SLM surface. Axicons with different angles can be readily implemented on the SLM, and the negative effects [9] of a rounded axicon tip can be

reduced. The SLM is mounted on a mirror mount that is fixed on a 3-axis translation stage and can be adjusted in pitch and yaw in addition to XYZ directions. This allows the holograms to be precisely aligned to the incident beam and collimation of the diffracted beam. The target HOM to be excited in the RGF can be adjusted by varying the axicon angle α, the focal lengths of the imaging lens pair, and the position of the fibre input end, as described in section 4.2.1. The illustration of HOM launching is depicted in Figure 4.13.
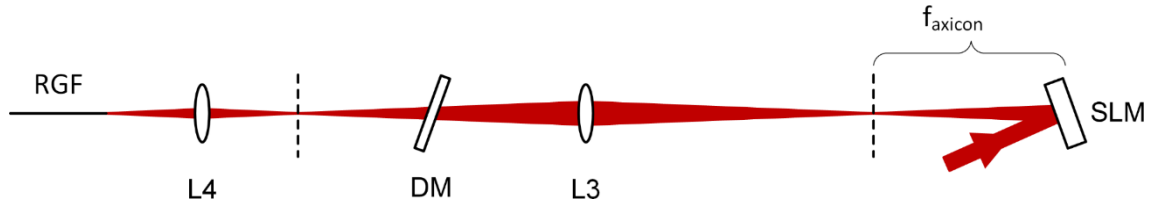
Figure 4.13: Illustration for HOM launching arrangement with SLM. Dashed lines denote object and image planes of L3. Path of pump beam not shown.

As mentioned in section 4.2.1, the relation between the axicon angle, the matching HOM and the magnification is given in equation (4.1). The location of the focal plane which is imaged to the facet of RGF with a lens pair L3 and L4 is given in equation (4.2). Although it is convenient to adjust the magnification by varying the distance between the two lenses, the tuning range can be limited since the total distance between the SLM and the front end of the RGF is limited by the available space. The first lens L3 is placed with its object plane near the SLM focal plane so that the magnification is roughly the ratio of the focal lengths of L3 and L4.

In our experiment, the maximum the SLM and L3 is limited to ~700 mm, by the distance between the output end of the YDF MOPA and the DM which sits between L3 and L4. The selection for L4 is also limited to a few available aspheric lenses that have adequate clear aperture for the pump beam and low aberrations. These aspheric lenses have focal lengths of 6~15 mm. In addition, although the SLM can in theory display phase patterns that correspond to any axicon angle, we have observed that the rapid phase change for a large angle axicon produces Bessel beams with less contrast between rings, which we believe is due to the limited SLM resolution and the relatively small incident Gaussian beam size of ~1.5 mm diameter. However, a smaller axicon angle leads to longer SLM focal length and shorter focal lengths of L3. As a trade-off we chose the angle value 0.787° that is used in [1]. The blazed grating has a fringe spacing of ~109 µm and the diffracted beams are along the horizontal direction. By varying the combination of L3 and L4 and tuning the position of the fibre end, we can excite HOM from LP_{05} to LP_{08}, of which LP_{05} displays best contrast of the transmitted beam. In theory, with 0.787° axicon angle, 1 mm incident beam diameter, and a magnification of ~25, the matching signal mode for the 50-µm RGF is LP_{07}. The discrepancy is mainly due to a different actual magnification and the imaging plane deviating from the focal plane of the SLM.

The facets of the RGF are perpendicularly cleaved to minimize distortions to the signal beam (facet image shown in Figure 4.14). Usually, in an amplifier configuration, the gain fibre is either angle

cleaved or spliced to endcaps to avoid Fresnel reflections at the interfaces. In our case, the perpendicular cleaves introduce feedback of ~4% at the fibre ends, but the reflections are unlikely to cause significant parasitic oscillations as we are using synchronized pulses with short durations of only a few nanoseconds. To elaborate, consider pump and signal pulses, both rectangularly shaped and with duration of τ_P, τ_S and peak power of P_P, P_S respectively. The centre of the pump and signal pulses are temporally aligned. The reflected signal with peak power ηP_S will meet a portion of the forward pump that is still within the fibre, where η is the reflectivity. For perpendicularly cleaved fibre facets without any coating, this reflectivity is roughly equivalent to a loss of ~14 dB. Assuming $\tau_P > \tau_S$, the leading edge of the reflected signal will overlap with the forward pump for a duration of $(\tau_P + \tau_S)/4$, and for the trailing edge the overlap duration is $(\tau_P - \tau_S)/4$. On average the reflected signal pulse will overlap with the forward pump for a duration of $\tau_P/2$, during which the signal pulse will see Raman gain. The overlap duration corresponds to a length of $v\tau_P/2$ and is limited by the actual fibre length L, where v is the group velocity of the pulse. If the single pass Raman gain is G_{sp}, then the reflected signal pulse will have an average gain of about $v\tau_P G_{sp}/2L$. If the pump pulse duration is less than double the transit time in the fibre, the doubly reflected signal, which is in the forward direction, will no longer meet the pump pulse and on average has a net gain of roughly $\left(G_{sp} + v\tau_P G_{sp}/2L - 28\right)$ dB. However, for pump pulses longer than this, the leading edge of the doubly reflected signal pulse may still overlap with the trailing part of forward pump pulse and will be amplified with another single pass gain. In case of rectangular pulses, this can lead to significantly higher net gain for the reflected signal if the single pass gain is much higher than the 14 dB reflection loss. Parasitic oscillations can occur, and unseeded Stokes can grow rapidly. In our case, the pump pulse duration is 5 ns, which is ~10% of the single pass time in a 10-m fibre. Assuming a 20 dB single pass gain, the doubly reflected signal pulse will not meet the pump pulse for a third time and only sees ~1 dB Raman gain. The total gain of the signal pulse after reflections from both the end and front facet becomes 20+1-28 = -7 dB, thus the perpendicular cleaves should not cause any parasitic effects.
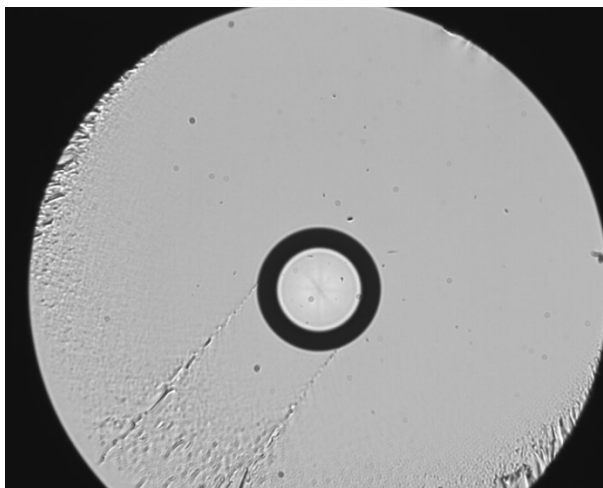
Figure 4.14: Image of the facet of the RGF. The dark ring corresponds to fluorine doped trench.

Despite the large number of modes supported in this fibre at 1 µm wavelength, the signal LP_{05} mode is expected to propagate stably thanks to the large effective index separation from the LP_{15} modes as well as the reduced fibre perturbations in the silica core. The effective index difference between LP_{05} and LP_{15} at 1114 nm is 7.8×10^{-4}, which is much higher than the 1.4×10^{-4} difference between LP_{01} and LP_{11} in this fibre.

4.3.2 Results and analysis
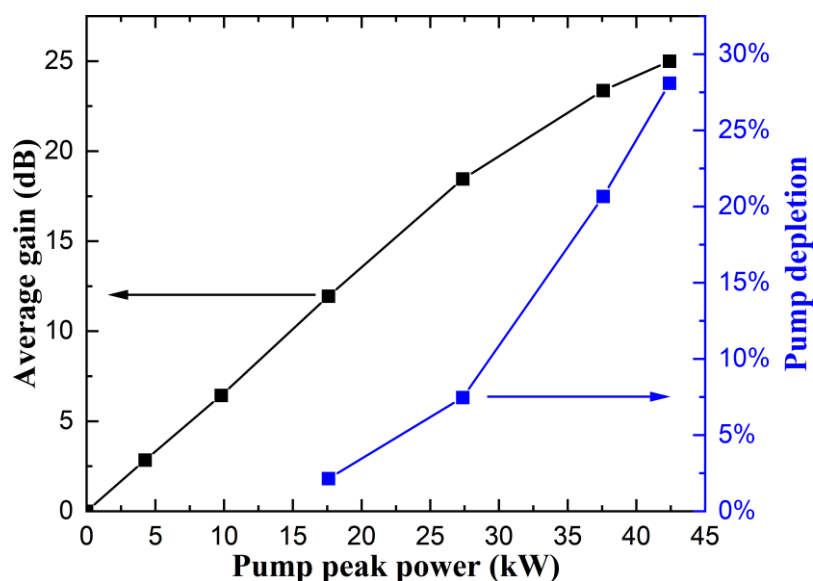
Figure 4.15: Measured average power gain and weighted pump depletion (right scale) versus launched pump peak power.

The measured average power gain of the signal (i.e., the ratio between the launched and output average powers) as well as the calculated weighted pump depletion (described in 4.2.2) versus the launched peak power is shown in Figure 4.15. The launched pump peak power is calculated from the transmitted average power when no Raman seed is present (unseeded) and the pulse duration of ~4.7 ns, disregarding any background loss. The launched Raman seed pulses have ~0.15 µJ of energy

and 58 W of peak power with a pulse duration of 2.5 ns. The Raman gain increases almost linearly with the pump peak power up to ~18.5 dB gain, with a slope of ~0.68 dB/kW. This slope corresponds to an effective area of ~3211 μm^2, assuming a Raman gain coefficient of 50 fm/W for unpolarized pump. The effective area is larger than the core size of 1963 μm^2, indicating a reduced spatial overlap between the pump and signal overlap. At 18.5 dB gain, the launched pump pulses have 128.7 μJ of energy and 27.4 kW of peak power, while the amplified signal pulse have 10.2 μJ of energy and 4.1 kW of peak power. The Raman gain reaches up to 25 dB as the launched pump increases to 42.4 kW of peak power and 199.3 μJ of pulse energy. At this gain, the signal pulses reach 46.1 μJ of energy and 18.5 kW of peak power. Figure 4.16 shows the measured spectra of the output signal with an OSA resolution of 0.5 nm. The launched Raman seed has a 3-dB spectral linewidth of ~11 nm with a peak at 1114.4 nm. A small peak around 1169 nm is also present as a result of conversion into higher order Stokes from the Raman seed source. The spectral shapes are slightly altered as the gain increases and significant power at longer wavelengths emerges beyond 18.5 dB gain due to strong nonlinear effects. At 25 dB gain, the linewidth is ~11.6 nm. The small peaks around 1060 nm are residual pump light that leaks into the signal arm. Higher pump power is available but not attempted due to the spectral broadening.
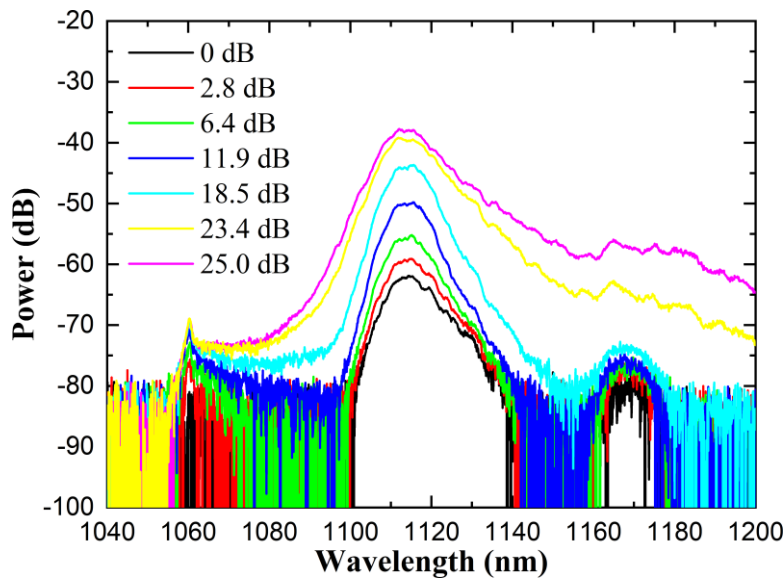
Figure 4.16: Measured spectra of the output signal. Resolution 0.5 nm.

Figure 4.17(a) shows the temporal traces of the pump pulse at 25 dB gain with and without Raman seed. Figure 4.17(b) shows the traces of the transmitted signal at 0 dB gain and the amplified transmitted signal at 25 dB gain. We calculate the weighted pump depletion to 28%. The peak instantaneous power of the unseeded pump drops by ~33%. The shape of the amplified signal pulse is slightly different from the unamplified pulse due to the non-constant instantaneous pump power and its varying degrees of depletion.
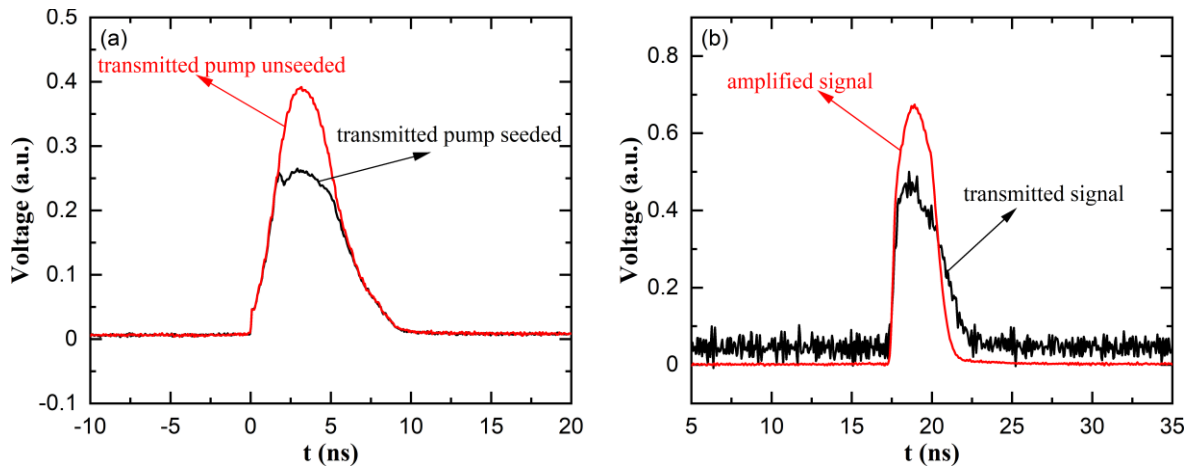
Figure 4.17: (a) Transmitted pump pulses at 25 dB gain level with (black curve) and without (red curve) Raman seed. (b) Transmitted signal pulses without pumping (black curve) and amplified signal (red curve).

The brightness enhancement once again can be evaluated as the increase in modal power as described in section 4.2.2. Here I estimate the average power in the pump modes from the measured beam quality of the pump which roughly gives the number of modes excited in the pump source. Although the actual power distribution among the pump modes is more complicated, I expect that this is a reasonable estimate of the brightness enhancement from pump to signal. From the measured M^2 value of 7 of the pump beam, we estimate ~49 modes in the pump beam, disregarding polarization multiplicity. At 25 dB gain, the launched pump has a peak power of 42.4 kW and ~865.3 W in each mode if we assume equal power distribution among all the modes. The amplified signal has a peak power of 18.5 kW. Assuming 90% of signal power in the target LP_{06} mode, the power per mode becomes 16.7 kW. The increase is ~12.9 dB, which is slightly less than our previous result with LP_{08}, although the difference may well be within the error margins.

Figure 4.18 shows the normalized near-field intensity profiles of the transmitted signal beam at 0 dB gain and 25 dB gain in linear scale and log scale, as well as the intensity profiles across the beam centre in log scale. The intensity profiles show very minor differences, indicating high mode preservation of the signal with high gain, high peak power, and moderate pump depletion. Although the mode-selective gain saturation is expected to be small in our case and not going to degrade the signal mode, the presence of spectral broadening and higher order Stokes prevents us from reaching any firm conclusions.
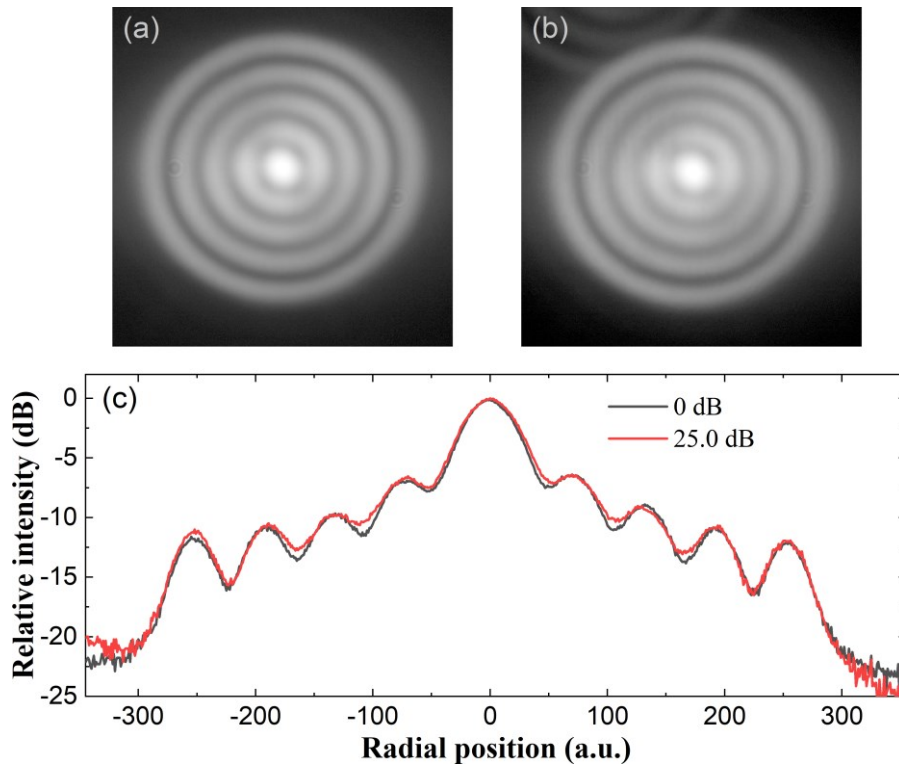
Figure 4.18: Intensity profiles of output signal at 0 dB gain (a) and 25 dB gain (b) with greyscale in log scale and normalized. (c) Line profiles across the centre of the beam at 0 dB and 25 dB gain in log scale.

In conclusion, the results are improved in Raman gain and peak power of the signal compared with our previous experiment, but with similar mode purity and pump depletion. However, a spectrally purer signal is required to suppress the nonlinear spectral broadening and higher order Stokes to pinpoint the reasons for the purity degradation. The temporal overlap between pump and signal pulses also requires adjustments to allow efficient Raman conversion. Nevertheless, the results demonstrate the versatility of the updated experimental setup and opens up for better performance and new applications with further optimizations.

4.4 Nanosecond pulsed fibre Raman amplifier for LP$_{06}$ mode with low brightness multimode pumping from YDF MOPA in a 335-m large mode area fibre

So far, our results have demonstrated multi-kW peak power capability of FRA for HOMs, with good mode purity preservation and more than 10 dB of pump to signal brightness enhancement. However, since Raman scattering is a relative weak process, high instantaneous pump intensity and peak powers of tens of kilowatt are required to reach sufficient gain in RGFs of tens of meters. Such high instantaneous power is usually only available from pulsed sources. The FRAs for HOMs are then limited to the pulsed regime, using pulsed pump sources. However, those are less cost effective and offer lower average power than continuous-wave pump sources (notably diode lasers), which are

fully adequate for pumping the rare-earth counterparts. Intuitively, a ready solution to this problem is scaling the fibre length to reduce the pump brightness and intensity requirement, which can ultimately allow for pumping directly with diode lasers. Thanks to the improvements in diode brightness and low loss fibres, it is already possible to pump RFLs with RGFs of length over 100 m directly with multimode diode lasers. Kuznetsov *et al.* demonstrated substantial brightness enhancement and ~50 W laser output with 1 km GRIN fibre [10]. RFL with output power over 100 W has also been demonstrated in 200 m of GRIN fibre [11]. In addition, pumping with multiple wavelength-combined diodes alleviates the brightness requirement of single diode and allows further power scaling. In ORC, Yao *et al.* demonstrated 20 W of RFL output in GRIN fibre and ~10× brightness enhancement in DCRF with two narrowly spaced diodes at ~975 nm [12]. Hong *et al.* have also reported RFL with spectrally combined pumping from five DLs in large core step index fibre [13]. Brightness enhancement is usually achieved via beam clean up effect in GRIN fibres or mode-selective launch and feedback in step index fibres. However, the beam clean up effect in GRIN fibres, which is essentially a mode competition process [14] that mostly favours the fundamental mode, is still unable to effectively suppress some HOMs such as LP_{11} mode relative to the fundamental mode and thus cannot convert the pump to a single signal mode. DCRFs are able to produce high beam quality output via mode selective devices such as fibre Bragg gratings (and, of course, mode-selective gain akin to that provided by rare-earth doping confined to the core, but this is much less effective with Raman gain). However, DCRFs are restricted in core/cladding area ratio in order to suppress higher order Stokes [15, 16], which ultimately limits the cladding area if the fundamental mode operation is desired in the core. FRAs for HOMs are promising alternatives to these configurations, allowing high beam quality and great mode area scalability in a multimode core that can be core-pumped directly by multimode diode lasers. Traditionally, a major concern for continuous-wave FRAs is mode coupling in extended fibre length. Higher order Bessel modes are expected to be resistant to mode coupling, but so far to the best of my knowledge there has been no demonstration of stable propagation let alone Raman amplification of these modes in fibres with length over 100 m.

Our previous results confirm the stability of HOMs in large core step index fibres with length of ~10 m. However, the broad spectral linewidth of the Raman signal can affect the performance of the SLM which results in reduced purity of the excited mode. The significant seed linewidth is also likely to increase the severe spectral broadening and growth of higher order Stokes, preventing further power scaling. We have thus improved the Raman seed source by reducing its spectral linewidth, to improve the purity of the excited mode and to alleviate the spectral broadening. We are therefore able to demonstrate 23 dB Raman amplification of a cleaner HOM in 335 m fibre with a pure-silica step-index core with a diameter of 70 μm and NA of 0.227. The signal peak power reaches 774 W with 942 W of pump peak power at 23 dB gain. This pump beam, although still from a pulsed YDF MOPA, has a relatively low brightness, which together with the compatibility of the core of

commercially available pigtailed high-power diode lasers (e.g., 105-μm core diameter with 95% of power within an NA of 0.16), predicts the feasibility of direct diode pumping.

4.4.1 Experimental setup
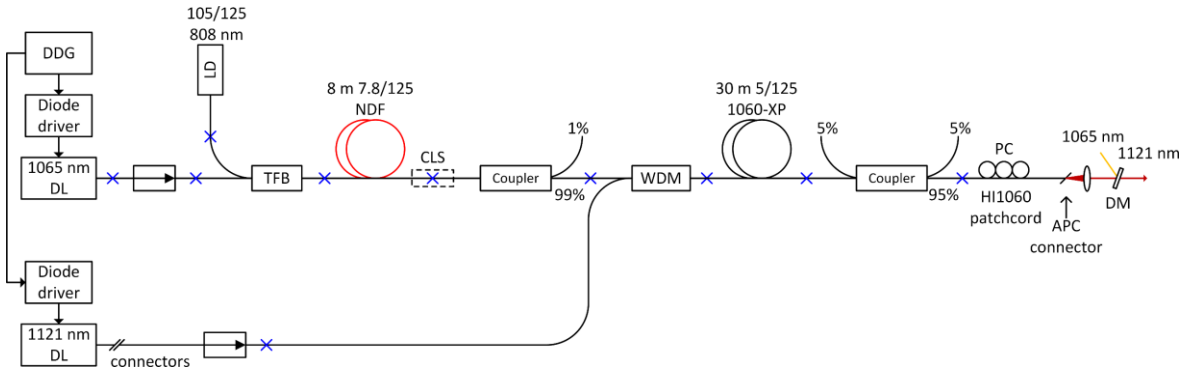
Figure 4.19: Schematic of the updated Raman seed source for the LP_{06} mode Raman amplification.

The Raman pump source remains almost the same as described in section 4.3 except for a different electrical driving configuration. The AWG that controls the diode driver (BFS-VRM 03 HP, Picolas) is now triggered by a digital delay generator (DDG, DG645, Stanford Research System). The DDG also controls the AOM in the MOPA. The Raman seed source is modified to generate narrow linewidth pulses at 1121 nm. A fibre Bragg grating (FBG) stabilized diode (QFBGLD-1122-400, QPhotonics) is added to the setup, as shown in Figure 4.19. It emits ~40 ns pulses at 20 kHz and is modulated by a driver board (BFS-VRM 03 LP, Picolas). The long pulse duration is to ensure wavelength locking. Its central wavelength is 1121.2 nm with a 3 dB linewidth of 0.08 nm, as shown in Figure 4.20. A PI isolator is connected to the 1121-nm diode and protects it from reflections and backward light. In the other arm, like in the previous setup, a Fabry-Perot diode (LC96A1060-20A, Bookham) emits 2-ns pulses at ~1065 nm that are amplified in an NDFA. The emission of the diode is tuned to longer wavelength by adjusting the diode temperature, to increase the Raman gain for 1121-nm light from the diode. Instead of being sent to the passive fibre for Raman conversion, the 1065-nm pulses are now combined with the 1121-nm pulses via a wavelength division multiplexer (WDM). The DDG that drives the YDF MOPA also drives the 1065-nm and 1121-nm diodes, synchronizing the pulses in the subsequent 30-m passive fibre to allow preamplification of the 1121-nm pulses. The combined pulses then pass a 5% tap coupler, a fibre polarization controller (PC), and a single mode fibre patch cord with an APC connector. The PC allows flexible control of the polarization of the Raman seed. The APC connector suppresses facet reflections back into the core. An aspheric lens collimates the output beam, of which the residual 1060-nm pump pulses are removed by a DM.
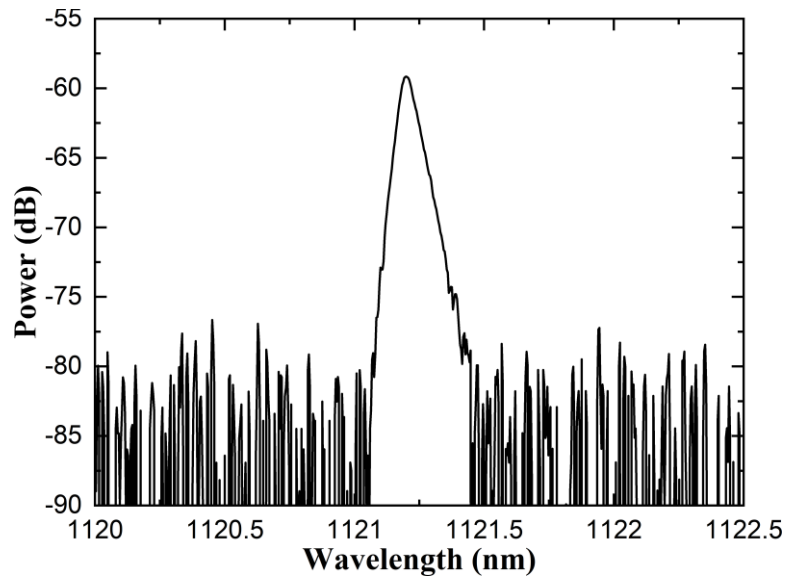
Figure 4.20: Spectrum of FBG stabilized diode. OSA resolution 0.02 nm.

The schematic of the main FRA is shown in Figure 4.21. The setup is similar to Figure 4.11 but with a few adjustments in generating the Bessel HOM. The collimated Raman seed is expanded to a diameter of ~3.2 mm by a telescope comprising a pair of plano-convex lenses L3 (f = 75 mm) and L4 (f = 200 mm) before being sent to the SLM. The expanded incident Gaussian beam to the SLM now allows more liquid crystal pixels per unit phase change and reduces the impact of the inactive area between pixels. The seed beam is linearly polarized and aligned by the PC to the preferred polarization of the SLM. The phase response of the SLM is recalibrated and compensated with a lookup table for 1121 nm. The hologram displayed on the SLM now has a diffraction grating encoded with 45° angle to the horizontal axis, so that the 1st order diffraction which contains the phase modulated beam does not overlap with the spurious diffractions from the spaced liquid crystal pixels [17]. The fringe spacing of the grating is ~88.9 μm, and an axicon with angle of ~0.45° (apex angle 179.55°) is implemented in the hologram. The lens after the SLM remains a plano-convex lens (L5) with 200 mm focal length, but the aspheric (L6) that launches the seed and pump beam into the RGF now has a 6.24 mm focal length.
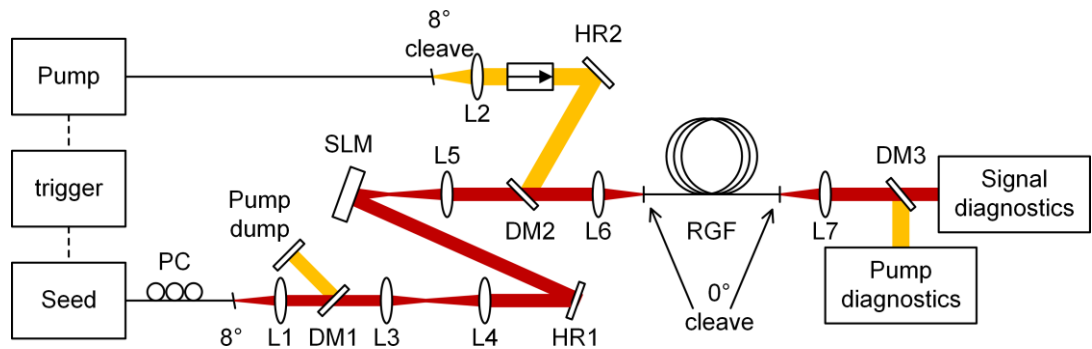
Figure 4.21: Schematic of the experimental setup for LP_{06} mode Raman amplification.

We determine the parameters based on our previous experiences, starting with the 200 mm (L5) and 8 mm (L6) lens combination. From here we tune the angle of axicon synthesized by the hologram

and adjust the position of the two lenses which are placed on translation stages, to achieve best transmitted mode purity. We then replace L6 with lenses of different focal lengths and repeat the process to compare the transmitted mode, during which we compare the contrast between the adjacent maxima and minimal of the intensity profiles. We settle for a lens L6 of 6.24 mm focal length and a signal mode of LP_{06}. We have also attempted launching and amplifying LP_{05} and LP_{07} modes. Similar gain levels were observed but with slightly worse transmitted mode purity than with LP_{06}. The converted mode near the focal plane of the SLM is shown in Figure 4.22. Despite a much longer RGF with a larger core of 70 µm diameter, the transmitted signal mode has better contrast between the rings than our previous results.
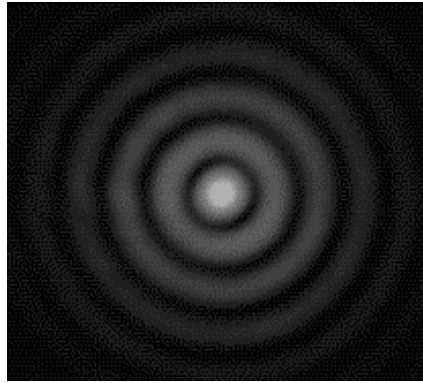
Figure 4.22: Bessel beam near the focal plane of SLM. Brightness and contrast adjusted for better visibility. White spot corresponds to higher intensity.

The RGF is a 335-m step index fibre with a pure-silica core of 70-µm diameter and 0.227 NA. The fibre is pulled in-house from the same preform pulled to 50-µm core fibre in the previous experiment. The cladding diameter is 483 µm and is surrounded by low index coating. We are not able to measure the refractive index profile of this fibre due to limitations in measurement devices. For reference, a refractive index profile scaled from the 50-µm core fibre is shown in Figure 4.23. At 1121 nm, the V value for the fibre is 44.5, and the estimated number of supported scalar modes (i.e., disregarding polarisation multiplicity and azimuthal dependence) is ~260 from a mode solver. The effective index difference between LP_{06} and its nearest neighbour antisymmetric mode LP_{16}, which is considered to be the most likely candidate for mode-coupling, is 5.0×10^{-4}. In comparison, the effective index difference between the fundamental mode and its nearest HOM, LP_{11}, is 7.6×10^{-5}. The large index separation between LP_{06} and LP_{16} helps to suppress mode-coupling. Furthermore, the differences between LP_{06} and LP_{05} (LP_{07}) is 8.9×10^{-4} (1.1×10^{-3}), which means that mode-coupling is unlikely. The RGF is coiled on a 31-cm diameter bobbin and again has both ends perpendicularly cleaved to suppress spatial beam distortion. As discussed in the previous section, reflections at fibre facets will not cause significant parasitic effects when the pulse is much shorter than the fibre length. The background loss is measured to ~0.8 dB/km for both 1065 nm and 1121 nm. The effective fibre length is hence ~325 m. We launch the signal beam into the core of the RGF with ~59% efficiency. For the pump, we slightly misaligned the incident pump beam from the fibre axis to excite more

pump modes and thus better approximate the beam profile from diode lasers. As a result, the launch efficiency of the pump beam is only ~50%, which is still fully adequate for this experiment.
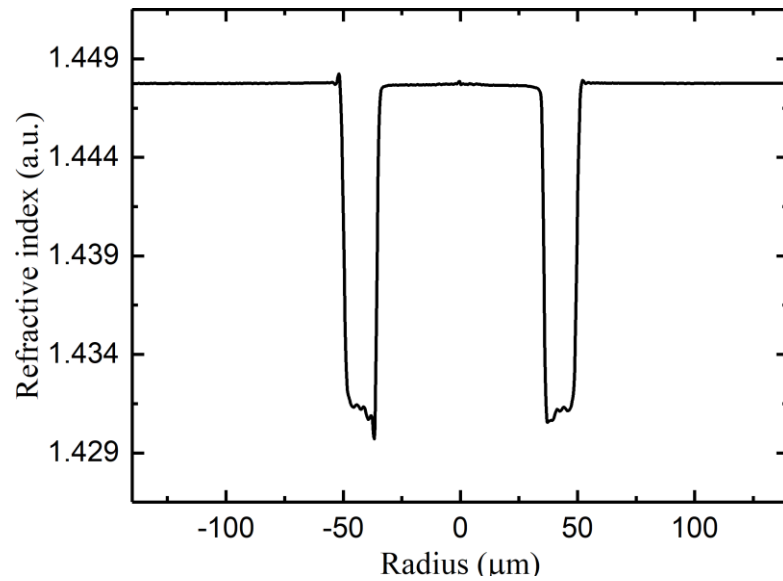
Figure 4.23: Refractive index profile of the RGF with 70-μm core. Scaled from the 50-μm core fibre which is pulled from the same preform.

The remainder of the experimental setup resembles the one described in the previous section (see Figure 4.11). The output beam is collimated by an aspheric lens L7 (f = 8 mm) and separated into pump and signal arms by a DM before being sent to their respective diagnostics. The temporal traces of both beams are captured by two 12.5 GHz InGaAs detectors (ET-3500, EOT) connected to a 6-GHz oscilloscope (Infiniium 54855A, Agilent). The average power of the transmitted pump and signal are measured by a thermal power meter and a lightwave multimeter (HP 81525A power head connected to HP 8153A module) respectively. The optical spectra are measured by an OSA (AQ6317B, Ando) in CW measurement mode. The imaged intensity profiles of both the transmitted signal and pump beams are measured by two 8-bit silicon cameras (DCC1545M, Thorlabs).

4.4.2 Results and analysis
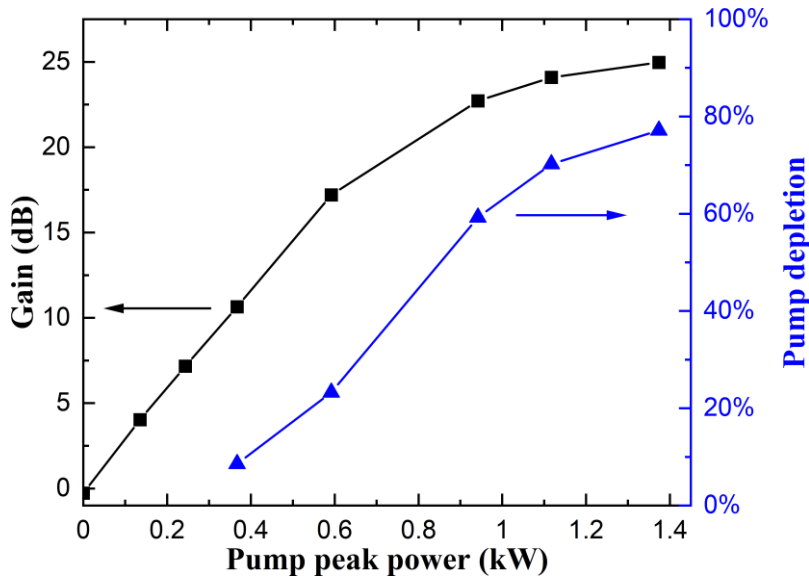
Figure 4.24: Average power gain of signal (black curve, left scale) and weighted pump depletion (blue curve, right scale) versus launched pump peak power.

The average power gain and the weighted pump depletion versus launched pump peak power are plotted in Figure 4.24. The gain is the ratio between the output average power at different pump levels and the launched average power. The launched pump peak power is calculated from the measured transmitted average pump power when no Raman seed is present for a FWHM pulse duration of ~11 ns. The fibre background loss of ~0.27 dB is accounted for in the peak power calculation. The weighted pump depletion is calculated as described in section 4.2. The Raman gain grows almost linearly with the pump peak power till ~17 dB gain, with a slope of ~29 dB/kW. Since the pump peak power is calculated with the transmitted pump duration which is much longer than the incident duration of ~4.6 ns, if we assume a linear pump pulse broadening along the fibre, the harmonic average of the pulse duration is $2 / (4.6^{-1} + 11^{-1}) = 6.5$ ns, and the actual slope is 6.5/11 of the 35 dB/kW. Hence, we can estimate the Raman gain coefficient to ~45 fm/W, if we assume that the pump is uniformly distributed across the fibre core. In reality, the effective area is larger than the core area, as the pump has a non-uniform intensity distribution and its overlap with the signal is not perfect. Nevertheless, the gain coefficient value agrees with the theoretical value for pure silica. After 17 dB, the gain starts to saturate due to pump depletion. At 23 dB gain, the signal pulses reach 774 W of peak power and 1.69 µJ of pulse energy, whereas the pump peak power is 942 W, and the weighted depletion is 59%. We reach a maximum gain of 25 dB with 1.4 kW pump peak power. At this gain, the signal peak power is 1.27 kW with 2.84 µJ of pulse energy. The pump depletion reaches 77%. Further power scaling is not attempted as 2nd order Stokes at ~1180 nm appears in the signal spectra, as shown in Figure 4.25(a). Zoomed-in spectra are shown in Figure 4.25(b). The transmitted signal without amplification has a linewidth of ~0.16 nm which is slightly broadened to 0.22 nm at 23 dB and 0.26 nm at 25 dB of gain. The 1180-nm peak is 22 dB lower that the peak at 1121 nm, however,

we estimate the power beyond 1140 nm is ~13% of the power from 1100 nm to 1140 nm by integrating the spectral power over respective range. This suggests non-negligible power is converted by other nonlinear effects (beyond the desired 1st-Stokes conversion). There is also self-phase modulation (SPM), which is evident from the peak at 1130 nm. Here the shorter wavelength part of the spectra is attenuated by the DM which separates the output pump and signal. The 2nd order Stokes, when unseeded, builds up from quantum noise [18], whose level can be estimated from the energy of a fictitious photon in each mode per effective bandwidth per second and the effective input Stokes power can be calculated with [19]:

$$P_S^{eff}(0) = h\nu_S B_{eff} N_P,\tag{4.4}$$

where ν_S is the signal frequency, N_P is the number of transverse modes in the pump and B_{eff} is the effective bandwidth, given by

$$B_{eff} = \frac{\sqrt{\pi}}{2}\frac{\Delta\nu_{FWHM}}{\left[I_P(0)g_R/\alpha_P\right]^{1/2}}.\tag{4.5}$$

Here, $I_P(0)$ is the input pump power, α_P is the loss for pump, g_R is the peak Raman gain coefficient which is ~50 fm/W and $\Delta\nu_{FWHM}$ is the FWHM width of the gain profile assuming a Lorentzian shape. In our case, the number of transverse modes is assumed to 500, and the effective bandwidth B_{eff} is estimated to ~1.06 THz assuming a FWHM width of ~100 cm^{-1}. Therefore, the equivalent noise input power is estimated to ~90 µW within ~4.3 nm at around 1.1 µm of wavelength. In comparison, by referencing to the measured average power at 1121-nm and the spectrum of the Raman seed output, the power at ~1180 nm is ~4 mW in 4 nm, which is 15 dB higher than the quantum noise. This suggests that Raman seed source is also seeding the 2nd order Stokes and a spectrally purer seed will allow higher Raman gain for the 1st order Stokes before unwanted nonlinear effects become prohibitive.
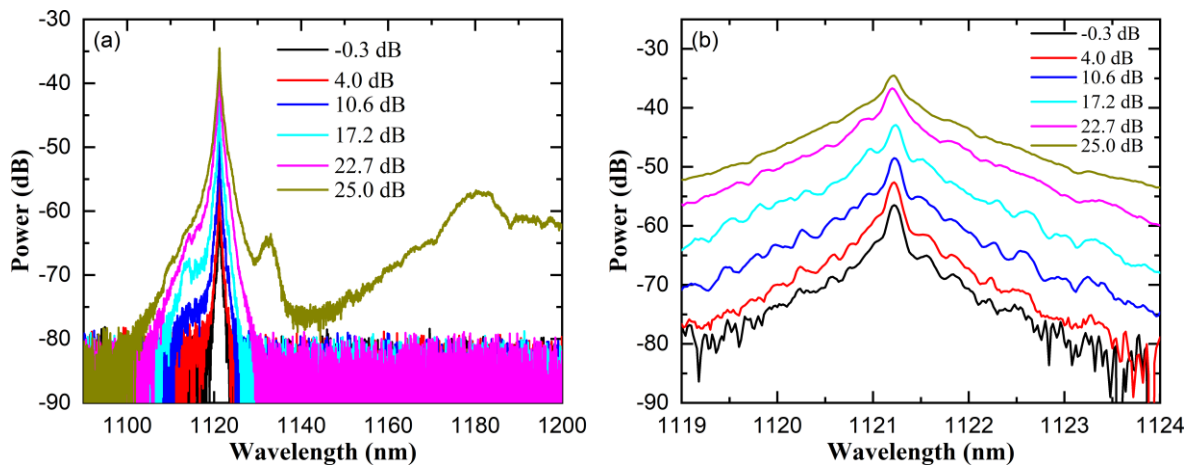

Figure 4.25: (a) Measured spectra of output signal. (b) Zoomed in spectra. Resolution 0.1 nm.

Temporal traces of the incident and transmitted pump and signal pulses are shown in Figure 4.26. Figure 4.26(a) shows the incident pump pulse and the transmitted pump pulse at 23 dB gain as well as the pump at the same pump level but without input Raman seed. The pump pulse shapes show significant depletion with the peak instantaneous power dropping by ~70% and a weighted depletion of 59%. The transmitted pump pulse also experiences dispersion that broadens the pulse from ~5 ns to ~11 ns. As the chromatic dispersion induced pulse broadening is only less than 100 ps in this fibre, the culprit for pulse broadening is modal dispersion. The actual broadening of ~6 ns is only ~1/3 of the estimated value of 20 ns from the core-cladding difference of the RGF, as described in [20]. This is indicative of an incident pump beam that is underfilling the core NA and thus exciting only part of the core modes. Coupling between the excited pump modes can also reduce the pulse broadening as the slowest modes can couple into faster modes. Figure 4.26(b) shows the incident signal pulse as well as the transmitted ones at 0 dB and 23 dB gain. The transmitted pulses have a duration of ~2.1 ns compared to the ~2.0 ns of the incident ones. The pulse shapes are almost identical for the incident and unamplified transmitted pulse. The amplified pulse however has a small shoulder in the leading edge which suggests a small fraction of power in modes with smaller group index than the signal mode. This can originate from an imperfect mode launch and / or mode coupling. In theory, the converted Bessel modes in free space has an overlap with the target fibre modes that is smaller than 100% [1]. Hence excitation of unwanted modes is inevitable, especially since the mode launch is tuned without real-time modal content analysis. Nevertheless, the close resemblance between the incident and transmitted pulses suggests good preservation of the target signal mode.
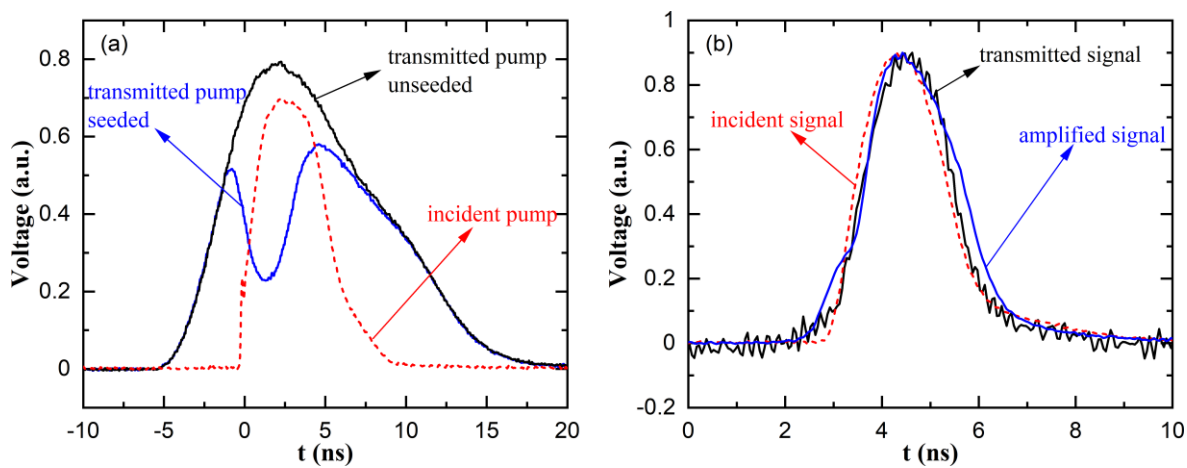
Figure 4.26: (a) Transmitted pump pulse at 23 dB gain with Raman seed (blue curve) and the same pump level but without seed (black curve). Incident pump shown in dashed curve, with shifted time and different scaling. (b) Incident (dashed curve) and transmitted signal pulses at 0 dB (black curve) and 23 dB (blue curve) gain. Traces scaled to same height.

There is also walk-off between the signal and pump beam due to different modal content and group velocities. The estimated delay between the LP_{06} at 1121 nm and LP_{01} at 1065 nm after 335-m fibre propagation is ~2.9 ns. The actual delay between pump and signal can be much less as the pump is multimode, and note that dispersion broadens the pump pulse from 5 ns to 11 ns. The walk-off affects

the shape of amplified signal as well as the pump depletion, as shown in Figure 4.27 where the amplified signal and the depleted pump are compared. Here, the depleted pump is simply the difference in the traces of the seeded and unseeded transmitted pump pulse. It is apparent that the depleted pump is longer that the signal, which can be partly explained by assuming that the pump is already significantly depleted where the remaining fibre length still causes a lot of broadening. The walk-off also contributes as the signal is effectively sweeping across a few nanoseconds of the pump pulse. It is worth noting that the neighbouring Bessel HOMs LP_{05} and LP_{07}, which have ~1 ns walk-off from LP_{06}, are having temporal overlaps with the pump that are close to LP_{06}. Consequently, these neighbouring modes will have similar gain to LP_{06}. Thus, the difference in group velocity between the most relevant signal modes is expected to not degrade or improve the signal mode purity.
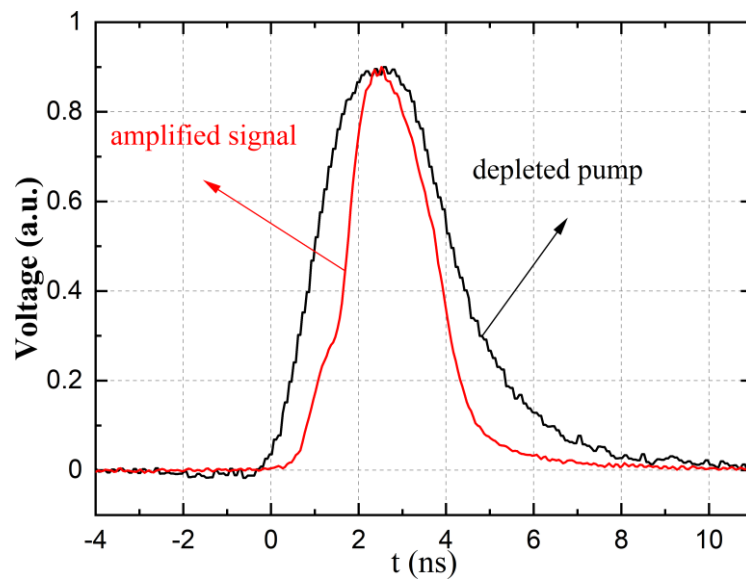
Figure 4.27: Pump depletion (black curve) and transmitted signal (red curve) at 23 dB gain. Traces are scaled and temporally shifted to have aligned peaks.

The 2D intensity profiles as well as the line profiles of the transmitted signal beam at different gain levels are shown in Figure 4.28. Compared with the results in section 4.2 and section 4.3, the transmitted signal beam, both unamplified and amplified, show better contrast between the neighbouring maxima and minima despite a 30 times longer fibre. The improvements are believed to mainly stem from the use of a spectrally purer Raman seed. The transmitted mode remains well preserved up to 23 dB gain, with only minor degradation in the contrast between rings. At 25 dB gain, there is stronger but still small degradation. We tentatively attribute the purity drop to the higher order Stokes and other nonlinear effects rather than the gain saturation. The growth of higher order Stokes consumes the signal beam and effectively introduces mode dependent losses to the signal beam. The higher Stokes order in the same spatial mode as the dominant target signal mode is expected to see the highest gain, and selectively deplete the dominant target mode. This leads to purity degradation. Although the converted higher order Stokes is likely to follow the modal distribution of the signal, its wavelength is outside the response range of silicon-based cameras. Power transfer from the target mode to the parasitic modes may also occur through other nonlinear

processes such as cross-phase modulation and four-wave mixing. The incident pump average power at 25 dB gain is ~0.6 W and is too low to introduce any thermal drifts. The measured temporal traces and the intensity profiles are also visually stable without any significant drifts or jitters in the short term.
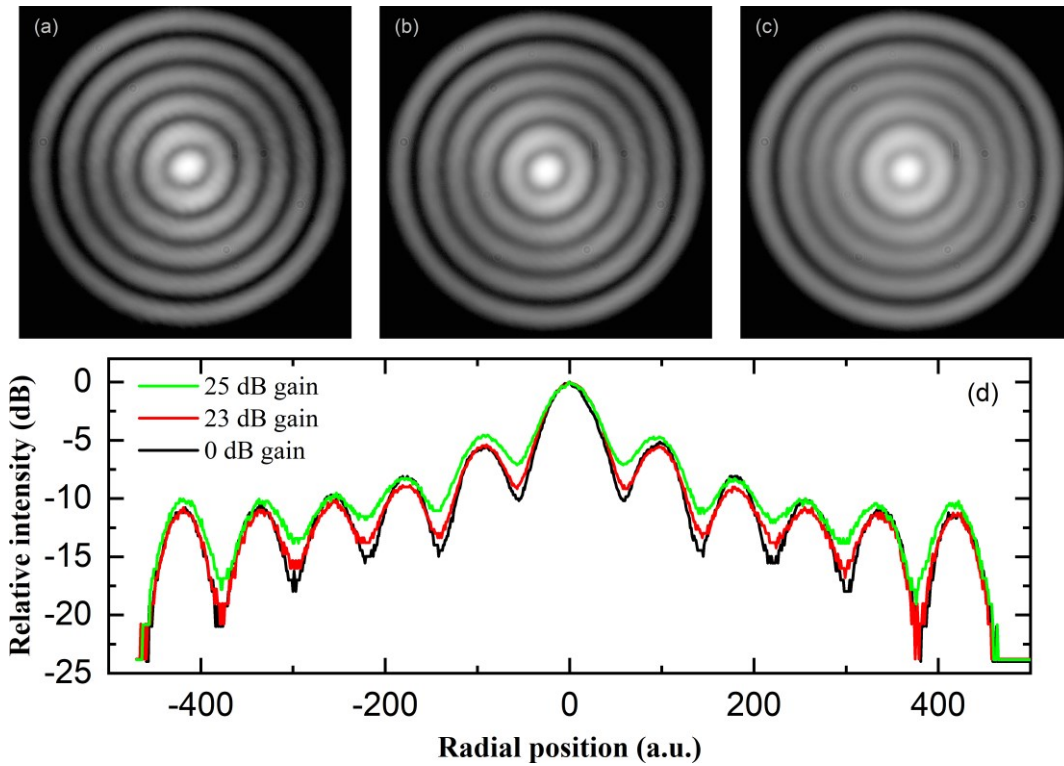
Figure 4.28: Intensity profiles of output signal beams at (a) 0 dB, (b) 23 dB, (c) 25 dB in log scale and normalized. (d) Normalized line profiles in log scale across the centre of the signal beams at selected gain levels.

To verify the effects of pump depletion on mode purity, we compare the near field intensity profiles of the transmitted pump beam captured with and without Raman seeding. These profiles, together with the line profile across the centre of the beam in linear scale, are shown in Figure 4.29. The plateaus in the centre may resemble that from a Gaussian distribution and suggest that the pump is mostly in the fundamental mode. However, the effective mode area of the unseeded pump beam at

23 dB gain, calculated by $A_{eff} = \left(\iint I(x,y)dxdy \right)^2 \Big/ \iint I^2(x,y)dxdy$ where $I(x,y)$ is the mode

intensity, is 3244 μm^2, which is 84.3% of the core area (3848 μm^2) and 169% of the effective area of the fundamental mode (1919 μm^2). The overlap [21] between the measured pump field and a simulated LP_{06} mode, is 2863 μm^2, whereas that between the fundamental mode and LP_{06} is 2290 μm^2. The signal mode thus sees 34% more gain with the measured pump than with a uniformly distributed pump, which is significant but modest. Therefore, although the pump looks similar to a Gaussian beam, it is closer to a uniform pump. The relative pump depletion, which is the difference in local intensity between the seeded and unseeded beam over the unseeded beam, is also plotted. At both gain levels, the relative depletion is almost uniform across the fibre core, with small peaks in

the centre and at the edges. There is no sign of significant transverse hole burning, at neither 23 dB nor 25 dB gain. As the local Raman gain depends only on the local pump intensity and overlap, the difference in local gain between the unwanted modes and the signal mode is little, if any. Hence, the pump depletion is unlikely to be the culprit behind the purity degradation.
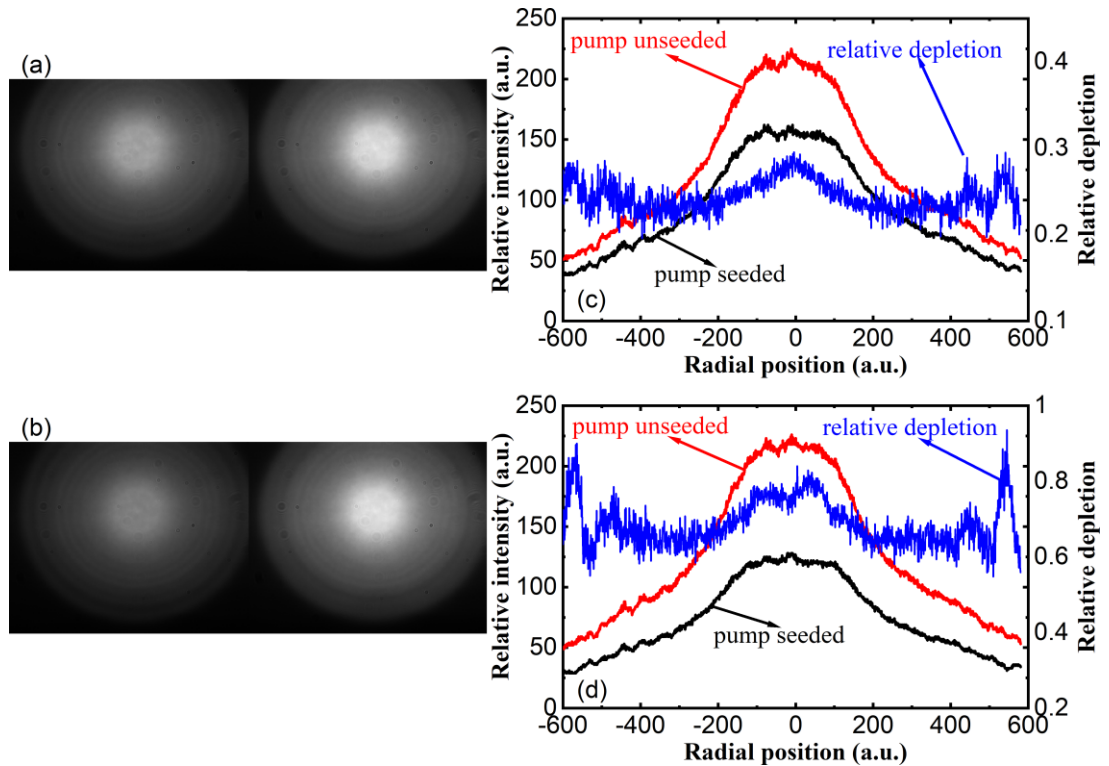
Figure 4.29: Intensity profiles of output pump beam with (left) and without (right) Raman seed at 23 dB (a) and 25 dB (b) gain. Line profiles of output pump beam (left scale) and transverse pump depletion (right scale) at 23 dB (c) and 25 dB (c) gain.

The brightness enhancement in terms of increase in power per mode from pump to signal can be calculated similarly to section 4.3. The pumping YDF MOPA has approximately 49 modes disregarding polarization multiplicity. At 23 dB gain, the launched pump has a peak power of 942 W and ~19.2 W in each mode if we assume equal power distribution among all the modes. The amplified signal has a peak power of 774 W. Assuming 90% of signal power in the target LP_{06} mode, the power per mode becomes 696.6 W. The increase is ~16 dB. Although the actual power distributions of the pump and signal may differ from the estimated value, and the peak pump power along the fibre varies due to dispersion, the pump brightness enhancement is still estimated to be at least 10 dB.

The long RGF used in the experiment allows high gain with multimode pumping at a brightness that is more than one order of magnitude less than our previous configurations. By scaling the fibre length, the requirement for pump brightness can be further relaxed to an extent where direct diode laser pumping is possible. The RGF has a beam parameter product of ~8 mm·mrad. For comparison, state-of-the-art laser diode at 976 nm emits ~150 W average power from a delivery fibre with 105-μm core

diameter with 90% power confined in a half-angle divergence of 0.15 rad, making the beam parameter product of diode output ~7.9 mm·mrad. This is comparable to that of the RGF and one can expect ~90% pump launch efficiency. Based on our results with a 335-m RGF, although the gain of the LP_{06} mode with the pump in our experiment is 34% higher than with a uniform distribution as is usually seen with DLs, by scaling the length of RGF to 1 km, we can still expect ~15 dB gain with ~200 W of diode laser pump power. These predictions are supported by recent diode-pumped results [13] in which a Raman laser is realised with a pure silica core 917-m fibre and wavelength-combined diode laser pumping.

In conclusion, we have demonstrated Raman amplification of a single HOM LP_{06} in a 335-m step-index RGF with a 70-μm core diameter. The signal mode is well preserved to 23 dB average power gain with low-brightness multimode pumping. The weighted pump depletion reaches 59% and the estimated pump to signal brightness enhancement is ~16 dB. The results confirm that FRAs are excellent for signal mode purity even under significant pump depletion. More importantly, the fact that our RGF and pumping configuration are compatible with CW direct diode laser pumping indicates that FRAs are an excellent platform for power scaling and brightness enhancement with clean and stable HOMs.

4.5 Quasi-CW fibre Raman amplifier for LP_{06} mode with spectrally combined direct diode laser pumping

Fibre Raman amplifiers and lasers are unique in that they are wavelength agile and allow power scaling in spectral ranges that are otherwise inaccessible by rare-earth doped fibre sources. However, FRAs and FRLs usually require rather sophisticated rare-earth doped fibre pump sources to reach adequate Raman gain, especially when single mode operation is favoured. In some cases, the requirement for pump brightness is so high that it can only be fulfilled in pulsed regimes. This adds complexity to the Raman pump sources. Thanks to the recent improvements of pump brightness in DLs and low loss RGF, as we have mentioned in the previous section, FRLs with direct diode laser pumping with high power output and substantial brightness enhancement have been demonstrated in the past few years. The utilization of diode laser pumping also enables FRLs emitting at wavelengths which are difficult for rare-earth doped sources [10, 22, 23]. Nevertheless, the potential of high brightness Raman sources at these wavelengths is still quite attractive.

The previous section verified the stability of Bessel HOM in a large core step index fibre with length of over 100 m, and efficient Raman amplification with low pump brightness requirement. The results, although achieved a with pulsed YDF based pump source, encourage me to attempt Raman amplification of HOM with CW diode laser pumping. Since longer fibre of the one used in the previous experiment is unavailable, I switched to the 50-μm core fibre which is pulled from the same preform and has been used in section 4.3 and in [13]. The fibre has the same core NA of 0.227 but a

reduced BPP of ~5.7 mm·mrad, which in theory allows only ~50% launch efficiency from a diode laser with BPP of 7.9 mm·mrad. However, the Raman gain per unit length stays roughly the same as with the 70-μm core fibre since the pump brightness is unchanged. To overcome the limited brightness of a single diode laser, we use the multi-wavelength pump source in [13] and build a FRA for HOM to verify the feasibility of direct diode laser pumping. The pump and signal are operating QCW to alleviate the thermal load and associated wavelength drifts in the diode lasers.

4.5.1   Experimental setup

The schematic of the experimental setup is shown in two parts in Figure 4.30 (a). The top part shows the FRA, and the bottom part shows the wavelength-combined pump source. A photo showing the part of Raman seed generation and launching is shown in Figure 4.30 (b). A Fabry-Perot diode laser (QFLD-1030-400S, QPhotonics) is direct-modulated by a diode driver (driver 3, SDL 820, Spectral Diode Labs) that is controlled by a 25 MHz AFG (AFG2, AFG31022, Tektronix). The diode emits pulses with duration of ~50 μs at 10 kHz repetition rate in the forward direction. A FBG (OEFBG-100, O/E Land) with a central wavelength of 1015.9 nm and spectral width of 0.5 nm connects to the diode laser and stabilizes its wavelength. The stabilized seed diode laser emits at 1016.3 nm with ~0.3 nm of linewidth. A PI isolator is connected to the FBG to protect the seed, and a single mode tap coupler is spliced to the isolator to monitor forward and backward beams. The main output of the tap coupler is collimated by an aspheric lens (L1, f = 8mm). A pair of plano-convex lenses (L2, f = 75 mm and L3, f = 150 mm) expand the beam to ~3 mm of diameter. A DM that transmits light with wavelength shorter than ~980 nm and a broadband mirror align the beam through the centre of the axicon. The axicon (XFM25-010-U-C, asphericon), which is made of fused silica, has an angle of 1° (apex angle 179°) and converts the incident Gaussian beam to a Bessel beam, as described in section 4.2. A plano-convex lens (L4, f = 150 mm) and an aspheric lens (L5, f = 11 mm) images the focal plane of the axicon to the facet of the RGF to excite the target signal mode. A DM between the two lenses reflects the transmitted backward pump and sends it to its diagnostics which include a thermal power meter and an OSA (AQ6315, Ando). The 877-m RGF is the same type as the one used in section 4.3 and is pulled from the same preform as the one used in section 4.4. It has a pure silica core with a diameter of 50 μm and NA of 0.227. The fibre facets are perpendicularly cleaved to mitigate distortions of the signal mode. The background losses are measured to 1.06, 1.25, 1.28, 1.70, 1.90 and 1.50 dB/km at 1016, 976, 969, 950, 940, 915 nm. The effective lengths at these wavelengths are ~790, 776, 773, 743, 729, 757 m, respectively. A homemade CLS removes the pump light in the cladding near the pump launch. An aspheric lens (L6, f = 20 mm) collimates the output signal beam and launches the combined pump beam at the same time. Two DMs steer the transmitted forward signal to its diagnostics which include a thermal power meter, a 350 MHz bandwidth Si detector (DET10A2) connected to a 1 GHz bandwidth oscilloscope (Infiniium DSO9104H, Agilent), the OSA and a silicon CMOS camera (DCC1545M, Thorlabs).
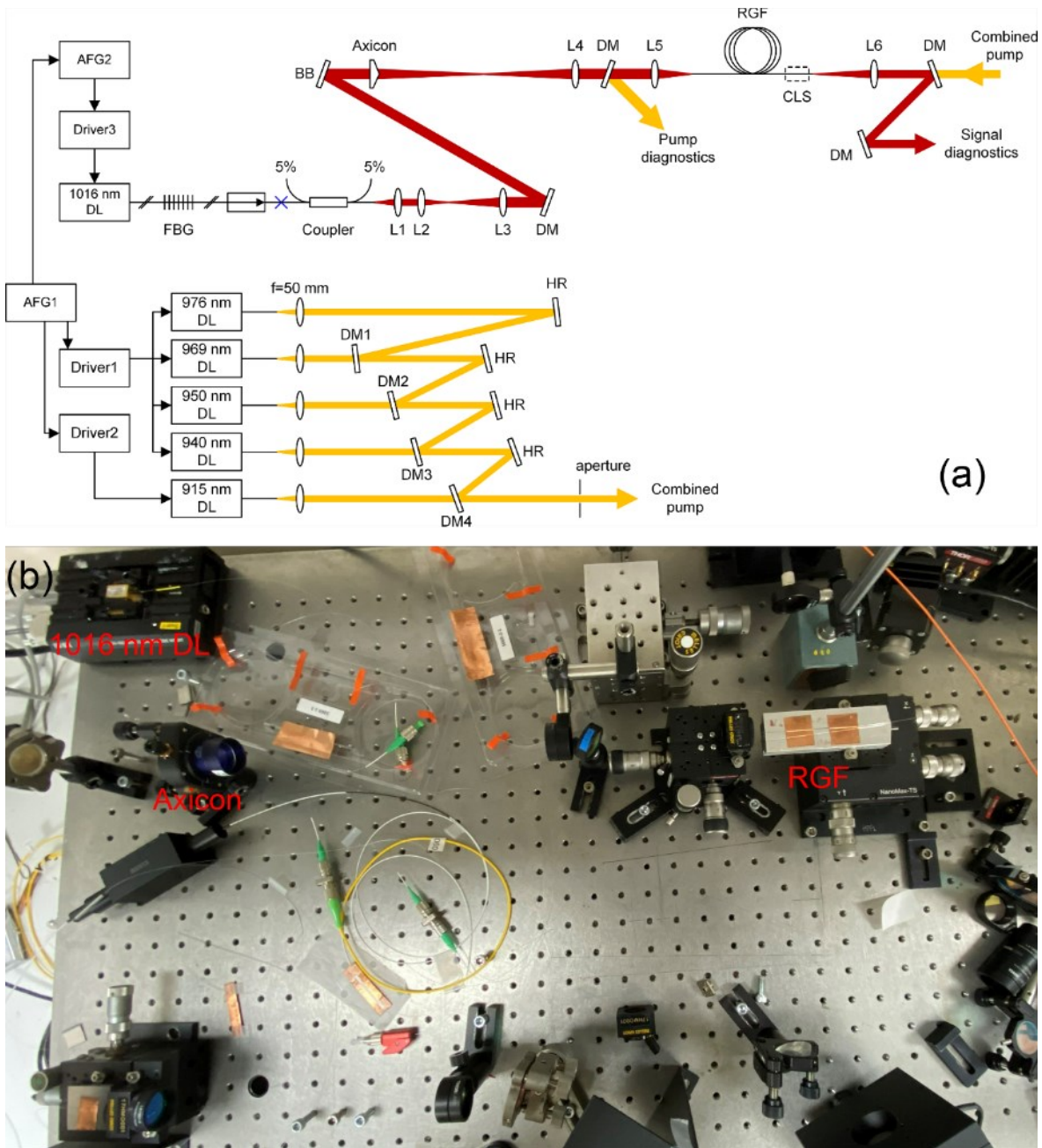
Figure 4.30: (a) Schematic of experimental setup for diode laser pumped LP$_{06}$ mode Raman amplification, including Raman seed source (top) and pump source (bottom). (b) Picture of the Raman seed source (top part of the schematic in (a)). The RGF and its output are not shown.

The pump source consists of five modulated DLs emitting at 976, 969, 950, 940 and 915 nm that are spectrally combined by several broadband mirrors and four DMs. The original setup is detailed in [13], but now updated with modifications in the way the DLs are driven. A four-channel diode driver (Driver 1, LDD-1125, Meerstetter) modulates the current of four DLs with wavelength from 976 to 940 nm individually while the 915 nm diode laser is modulated by another diode driver (Driver 2, LDD-1046, Meerstetter). Another 150 MHz AFG (AFG1, AFG31152, Tektronix) triggers both drivers and ensures temporal synchronization between the different diodes. The modulation of the 915 nm diode follows the voltage from AFG1 while the modulation of the other diodes is controlled via a software interface. All the DLs emit pulses with ~100 μs duration and 1 kHz

repetition rate, with a duty cycle of ~10%. The DLs work QCW to avoid excessive thermal load primarily in the diode lasers but also at the fibre launch and in the optics, while the long pulse duration allows accurate performance approximation to CW operation. The 976, 969 and 940 nm DLs are wavelength-stabilized and have emission linewidths of ~0.5 nm at full power, although the 940 nm diode laser has significant unstabilized emission at shorter wavelengths. The measured spectrum of the combined beam at full pump power is shown in Figure 4.31. The DLs all have 105/125 μm pigtails with core NA of 0.22 and 95% of the output power specified to be within a half-angle divergence of 0.15 rad. The output beams are collimated individually with aspheric lenses (f = 50 mm) and combined one after another from long to short wavelength by DMs. DM1 to DM4 have the same coating but are placed with slightly different angles of incidence to tune the transmission range. The combined beam passes through a 10-mm diameter aperture before being launched to the RGF to reduce the angular spread of the focused pump beam. At full pump current, the total average power incident to the RGF is 36.1 W, which corresponds to a peak power of ~361 W, and each of the DLs emits 4.6, 9.0, 5.2, 7.4 and 9.9 W of average power from 976 nm to 915 nm, in descending wavelength order. This is calculated from the increment of total power when each diode laser is turned on one after another. The average power of each diode laser, when turned on individually, is 4.6, 9.0, 5.1, 7.1 and 10.0 W with a sum of 35.8 W, which is slightly different than when the DLs are turned on one after another. This crosstalk between the DLs may be caused by wavelength drifts and thermal drifts, e.g., in the mirrors or the heatsinking, where a single chiller was used for all the diode lasers. The 20 mm launching lens is selected as it provides best coupling efficiency, although the spot size is slightly larger than the core size and the angular spread of the focused pump beam is over-filling the core NA. The launched pump average powers, estimated from incremental transmitted pump power and fibre background loss at different wavelengths, are 2.5, 3.7, 2.1, 3.2 and 4.5 W. The pump beam propagates in the backward direction and is collimated by L5 before it is reflected by a DM. Although it is possible to double pass the pump beam by adding another DM, our preliminary attempts with double passing do not yield any significant improvements in Raman gain.
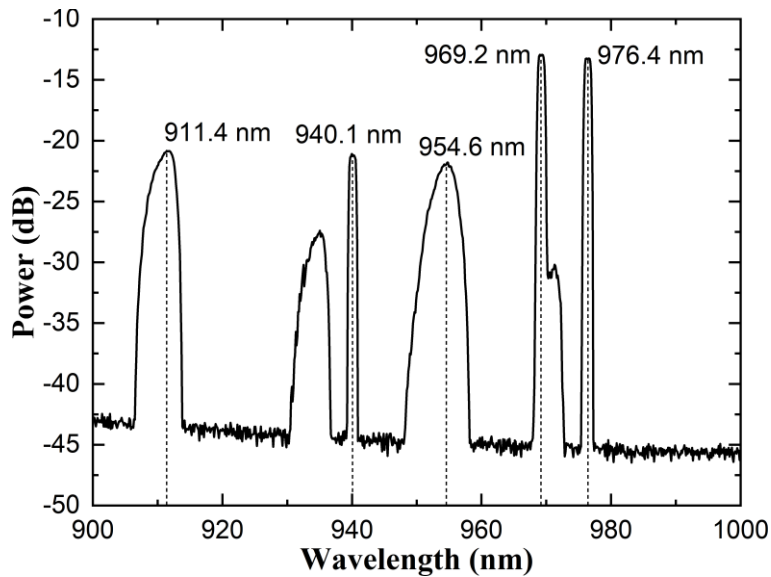
Figure 4.31: Spectra of combined pump from diode lasers at full power. Resolution 1 nm.

4.5.2   Results and analysis

Figure 4.32(a) shows the average power Raman gain versus launched pump peak power and the transmitted signal spectra. The Raman gain is calculated from the transmitted signal average powers with and without pumping. The launched pump peak power is estimated from the measured increment in transmitted pump average power, the wavelength-dependent background loss and the measured pulse width as the diode lasers are turned on one by one. The point where each pump is added is labelled in the plot. The launched Raman seed has an average power of 4.14 mW which corresponds to a peak power of 82.4 mW. A maximum on-off gain of 6 dB is achieved with full pump power. At this gain level, the amplified signal reaches 13.4 mW of average power and 243.7 mW of peak power, with a total launched pump peak power of 170.8 W. The maximum launched peak power of the diode lasers with wavelength from 976 to 915 nm, are estimated to 26.2, 38.1, 22.2, 32.7 and 47.4 W, respectively. The spectra of the transmitted signal are measured in the peak hold mode of the OSA with 10 ms hold time and a resolution of 0.1 nm. The spectral gain is ~6.5 dB and agrees with the average power gain.
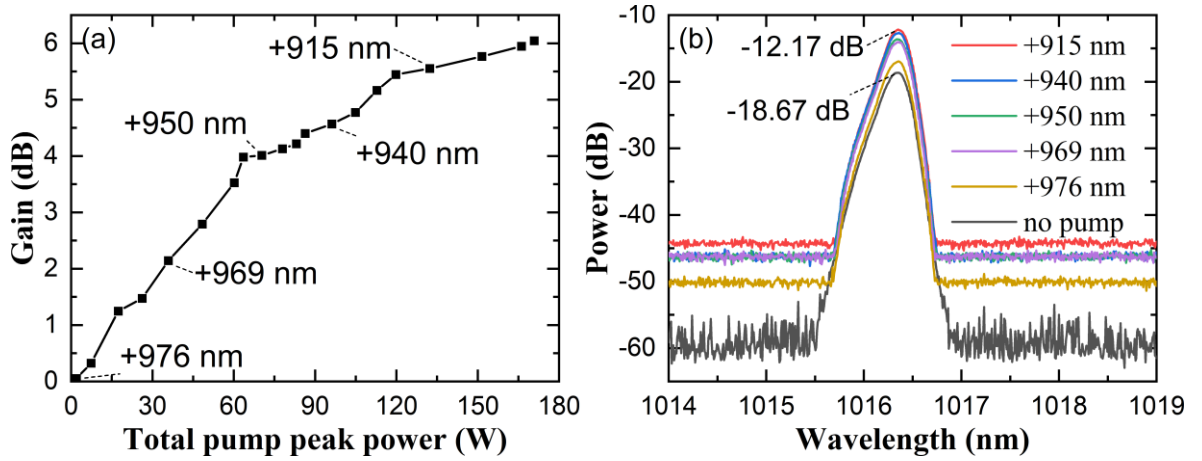
Figure 4.32: (a) Measured average power on-off gain versus total launched pump peak power. The labels show the power at which each diode laser is turned. (b) Measured spectra of output signal beam. Different curves correspond to maximum pump power before the next shorter-wavelength diode laser is turned on in (a) (e.g., +969 nm means that the 976-nm and 969-nm diode lasers are both at full power whereas the others are off).

The slope of gain versus launched pump peak power is 0.061, 0.064, 0.022, 0.038 and 0.012 dB/W after each pump diode laser from 976 to 915 nm is added. The slope for 976 and 969 nm is less than the theoretical slope of ~0.088 dB/W estimated with Raman gain coefficient of 50 fm/W for unpolarized pump in silica. As more pump wavelength is added, the signal and pump beams are coupled via differential equations with different Raman gain coefficient and mode overlap [18]. The estimated Raman gain coefficients between different wavelengths based on frequency shift is listed in Table 4.1. The effective gain coefficients calculated from the measured gain slope and the effective fibre lengths at each wavelength are also listed in the table. We see that the Raman gain coefficient varies by a factor of 15, whereas the variation in gain slope is only a factor of five. This is attributed to cascaded Raman scattering [24]. From the table we can see that the 915 nm diode laser mainly contribute to the 950 nm pump, which however has the least gain coefficient with the signal. This agrees with the low gain slope for 915 and 950 nm pumps. However, in comparison, the results presented in [13] suggest at least ~14 dB round trip Raman gain with ~100 W pump power. The pump configuration and power level are similar to ours. Although we are not double passing the pump, the single pass gain with ~170 W pump peak power is expected to be higher than 7 dB. This suggests excessive loss somewhere in the setup, presumably the RGF. Alternatively, the discrepancy is due to the difference in overlap between the pump and signal. However, as we are observing almost top-hat transmitted pump distribution, the difference in modal gain is expected to be negligible.

Table 4.1: Estimated Raman gain coefficients between wavelengths based on frequency shifts.

Wavelength (nm)	940	950	969	976	1016	Gain slope from Figure 4.32(a) (dB/W)	Effective g_R (fm/W)
915	29.4	47.3	15.7	4.0	3.1	0.012	7.2
940		12.1	34.0	45.9	8.8	0.038	23.6
950			18.0	27.4	4.0	0.022	13.4
969				9.4	46.4	0.064	37.4
976					47.1	0.061	35.6

The temporal traces of the transmitted signal as well as the incident scattered pump at different pump levels are shown in Figure 4.33. A small portion of the pump leaks into the signal diagnostic and has been subtracted. The transmitted signal without amplification is close to a top-hat shape. The long tail is due to the response time of the diode driver. As the gain increases, the top of the pulse becomes more slanted, with the trailing part having higher amplitude, which suggests higher gain for the trailing part of the pulse. This is because the transit time of the pump and signal pulses is only ~4 µs in the fibre and the power in the pump pulse increases continuously. The leading edge of the signal pulse only meets the leading part of the pump pulse in the fibre whereas the trailing edge of the signal pulse sees the part where the pump power is higher. Nevertheless, this effect is minor and not detrimental.
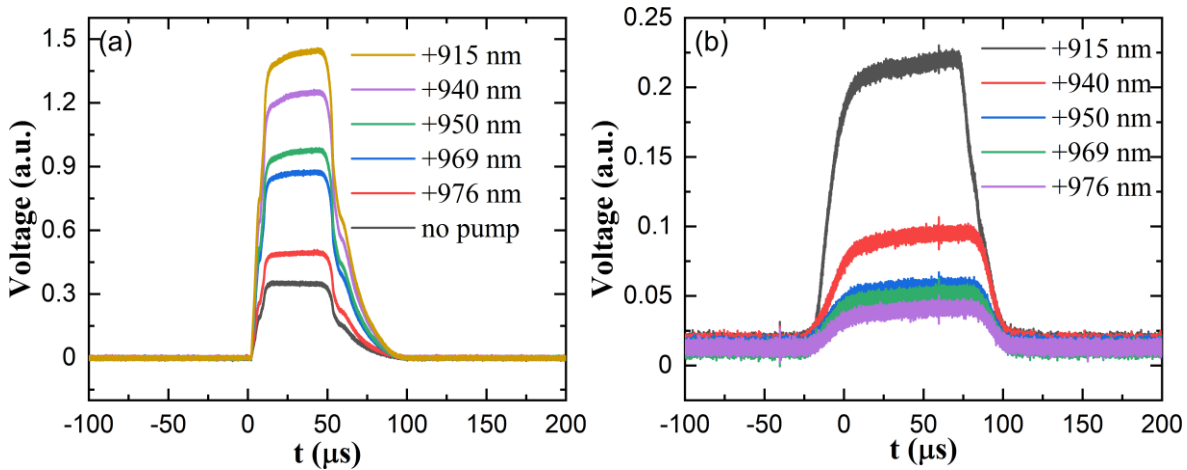
Figure 4.33: (a) Transmitted signal with no pumping and at maximum output of each diode laser. (b) Scattered pump at the maximum power of each diode laser.

The intensity profiles of the transmitted signal beam as well as the line profiles across the centre of the beam at different gain levels are shown in Figure 4.34. The intensities are plotted in log scale and normalized to enhance visibility. The unamplified signal displays good contrast between the rings even after propagation in fibre with length of almost 900 m. This again verifies the stability of Bessel

HOMs in large core fibres. The amplified signal sees negligible purity degradation, which is expected as the Raman gain is relatively low and there is almost no pump depletion. There is also no signal of 2nd order Stokes or significant other nonlinear effects.
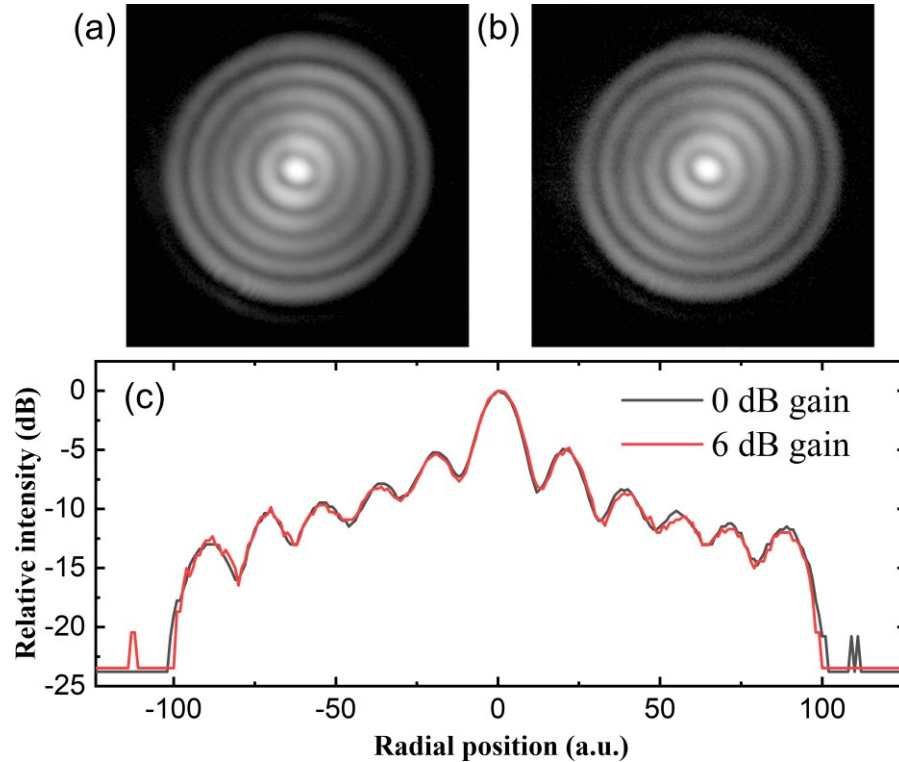
Figure 4.34: Intensity profiles of transmitted signal in log scale at (a) 0 dB and (b) 6 dB gain. (c) Line profiles across the centre of the beam at two gain level. Intensity plotted in log scale.

As the input Raman seed has much lower peak power than the pump, and the difference between the power of transmitted pump beam with and without Raman seed is comparable to the pump power fluctuations, the pump power depletion and the conversion efficiency from pump to Stokes are not evaluated. Future experiments with higher seed power are likely to clarify this.

In conclusion, despite the low Raman gain, these preliminary experimental results suggest great potential of diode pumped FRA for HOM with further optimizations. A gain fibre with higher BPP will significantly improve the pump launch efficiency and hence the Raman gain. Our results prove the feasibility of power scaling of HOM in large core FRAs with diode laser pumping, which points towards a flexible option for power scaling and brightness enhancement with excellent mode purity.

4.6   Summary

In this chapter I report four FRAs for Bessel HOMs with various RGF length and pumping configurations. Firstly, 18-dB Raman amplification of a single HOM LP_{08} in a 9-m 50-µm-diameter-core step-index fibre with pulsed multimode pumping from a YDFA is presented, which is the first demonstration of a FRA for Bessel HOM with multimode pumping. The output signal reaches 4.6 kW of peak power and 115 µJ of pulse energy, with ~36.7% weighted pump depletion. Then I

introduce 25-dB Raman amplification of LP_{05} mode in 10-m 50-μm-diameter-core step-index fibre with amplified signal of 18.5 kW peak power and 46.1 μJ pulse energy. The weighted pump depletion at 25-dB gain is 28%. After that, a low-brightness-pumped FRA for LP_{06} in 335-m 70-μm-diameter-core step-index fibre is discussed. The amplified signal reaches 774 W of peak power and 1.7 μJ of pulse energy with 942 W of pump peak power. The weighted pump depletion reaches ~59%. This is the first demonstration of stable propagation and Raman amplification of a single Bessel HOM in a fibre of hundreds of meters, and it opens up for direct diode laser pumping for FRAs with high signal mode purity. Last but not least, a proof-of-concept experiment on Raman amplification of a single Bessel HOM with spectrally combined diode laser pumping is reported. The maximum average power signal gain is 6 dB, with a combined launched peak power of 170.8 W. The results verify the feasibility of direct diode pumping for large core FRAs with pure signal mode. In each of the different configurations, the signal HOM is well preserved, even under high pump depletion and after hundreds of meters of propagation in the fibre. The output intensity profiles remain visually stable for at least a few hours when unpumped and for over 10 minutes when at maximum gain before being perturbed by the drifts in the alignment of the optics. The amplifiers also remain stable when external perturbations to the gain fibre, such as bending, minor twisting and pressing, are applied. The collective results showcase the exceptional flexibility of FRAs in power scaling and brightness enhancement with excellent mode purity, and the feasibility of FRAs as a competitive alternative to rare-earth doped fibre amplifiers in a wide range of applications.

4.7   References

[1]   J. Demas, L. Rishøj, and S. Ramachandran, "Free-space beam shaping for precise control and conversion of modes in optical fiber," Opt. Express **23**, 28531 (2015).

[2]   S. Ramachandran, J. W. Nicholson, S. Ghalmi, M. F. Yan, P. Wisk, E. Monberg, and F. V. Dimarcello, "Light propagation with ultralarge modal areas in optical fibers," Opt. Lett. **31**, 1797 (2006).

[3]   S. Zhu, S. Pidishety, Y. Feng, S. Hong, J. Demas, R. Sidharthan, S. Yoo, S. Ramachandran, B. Srinivasan, and J. Nilsson, "Multimode-pumped Raman amplification of a higher order mode in a large mode area fiber," Opt. Express **26**, 23295 (2018).

[4]   O. Shapira, A. F. Abouraddy, J. D. Joannopoulos, and Y. Fink, "Complete modal decomposition for optical waveguides," Phys. Rev. Lett. **94**, 143902 (2005).

[5]   D. B. S. Soh, J. Nilsson, S. Baek, C. Codemard, Y. Jeong, and V. Philippov, "Modal power decomposition of beam intensity profiles into linearly polarized modes of multimode optical fibers," J. Opt. Soc. Am. A **21**, 1241 (2004).

[6]   J. W. Nicholson, A. D. Yablon, S. Ramachandran, and S. Ghalmi, "Spatially and spectrally resolved imaging of modal content in large-mode-area fibers," Opt. Express **16**, 7233 (2008).

[7]   D. N. Schimpf, R. A. Barankov, and S. Ramachandran, "Cross-correlated (C^2) imaging of fiber and waveguide modes," Opt. Express **19**, 13008 (2011).

[8]   J. Demas, and S. Ramachandran, "Sub-second mode measurement of fibers using C^2 imaging," Opt. Express **22**, 23043 (2014).

[9]   O. Brzobohatý, T. Čižmár, and P. Zemánek, "High quality quasi-Bessel beam generated by round-tip axicon," Opt. Express **16**, 12688 (2008).

[10]   A. G. Kuznetsov, S. I. Kablukov, A. A. Wolf, I. N. Nemov, V. A. Tyrtyshnyy, D. V. Myasnikov, and S. A. Babin, "976 nm all-fiber Raman laser with high beam quality at multimode laser diode pumping," Laser Phys. Lett. **16**, 105102 (2019).

[11]   Y. Glick, V. Fromzel, J. Zhang, N. Ter-Gabrielyan, and M. Dubinskii, "High-efficiency, 154 W CW, diode-pumped Raman fiber laser with brightness enhancement," Appl. Opt. **56**, B97 (2017).

[12]   T. Yao, A. V. Harish, J. K. Sahu, and J. Nilsson, "High-power continuous-wave directly-diode-pumped fiber Raman lasers," Appl. Sci. **5**, 1323 (2015).

[13]   S. Hong, Y. Feng, and J. Nilsson, "Wide-span multi-wavelength high-power diode-laser pumping of fiber Raman laser," IEEE Photonics Technol. Lett. **31**, 1995 (2019).

[14]   N. B. Terry, T. G. Alley, and T. H. Russell, "An explanation of SRS beam cleanup in graded-index fibers and the absence of SRS beam cleanup in step-index fibers," Opt. Express **15**, 17509 (2007).

[15]   J. Ji, "*Cladding-pumped Raman fibre laser sources*," PhD dissertation (University of Southampton, 2011).

[16]   J. E. Heebner, A. K. Sridharan, J. W. Dawson, M. J. Messerly, P. H. Pax, M. Y. Shverdin, R. J. Beach, and C. P. J. Barty, "High brightness, quantum-defect-limited conversion efficiency in cladding-pumped Raman fiber amplifiers and oscillators," Opt. Express **18**, 14705 (2010).

[17]   D. Palima, and V. R. Daria, "Effect of spurious diffraction orders in arbitrary multifoci patterns produced via phase-only holograms," Appl. Opt. **45**, 6689 (2006).

[18]   G. P. Agrawal, *Nonlinear Fiber Optics* (Elsevier Science & Technology, 2006).

[19]   R. G. Smith, "Optical power handling capacity of low loss optical fibers as determined by stimulated Raman and Brillouin scattering," Appl. Opt. **11**, 2489 (1972).

[20]   J. Ji, C. A. Codemard, J. K. Sahu, and J. Nilsson, "Design, performance, and limitations of fibers for cladding-pumped Raman lasers," Opt. Fiber Technol. **16**, 428 (2010).

[21]   R. Stolen, and J. Bjorkholm, "Parametric amplification and frequency conversion in optical fibers," IEEE J. Quantum Electron. **18**, 1062 (1982).

[22]   S. I. Kablukov, E. I. Dontsova, E. A. Zlobina, I. N. Nemov, A. A. Vlasov, and S. A. Babin, "An LD-pumped Raman fiber laser operating below 1 μm," Laser Phys. Lett. **10**, 085103 (2013).

[23]   E. A. Zlobina, S. I. Kablukov, A. A. Wolf, A. V. Dostovalov, and S. A. Babin, "Nearly single-mode Raman lasing at 954 nm in a graded-index fiber directly pumped by a multimode laser diode," Opt. Lett. **42**, 9 (2017).

[24]   N. Zhao, S. Hong, A. V. Harish, Y. Feng, and J. Nilsson, "Simulations of multiwavelength cladding pumping of high-power fiber Raman amplifiers," Opt. Eng. **58**, 1 (2019).

Chapter 5 Fibre Raman amplifiers for orbital angular momentum modes

5.1 Introduction

As introduced in section 2.2.4, fibre modes carrying OAM are a group of HOMs that differ from the Bessel HOMs (as well as many other modes) in that they carry azimuthally dependent phase front in a helical fashion (right-handed or left-handed). True OAMMs are circularly polarized and in addition carry SAM of $\pm\hbar$ per photon. In the weakly guiding approximation, linearly polarized OAMMs can also be formed by pairs of degenerate LP_{lm} modes with $l \geq 1$. Like Bessel modes, FRAs are expected to preserve the OAMMs well thanks to the low perturbations of "passive" fibres (i.e., without rare earths and other dopants and compositions that are difficult to fabricate) and non-local gain saturation. An important difference though is degeneracy. A Bessel-mode is generally non-degenerate (unless accidentally degenerate, and then with a mode that differs both in radial and azimuthal mode order, which reduces the coupling rate). By contrast, an OAMM and its oppositely handed conjugate are degenerate (in the absence of circular birefringence). Degenerate modes can be assumed to be spatially coherent, and this leads to gain gratings and coherent gain saturation and competition [1, 2]. When the intensity-overlap between coherent modes is large, then the gain compression in a locally saturating gain medium is stronger for the weaker mode than for the stronger mode, which is the opposite to non-degenerate modes. The local gain saturation of Yb can then help to reduce the growth of a degenerate parasitic mode, including a parasitic conjugate OAMM, with perfect intensity overlap with the desired OAMM. However, differences in polarization may reduce this effect (if the interference pattern and thus the gain grating become weaker), although I have not investigated it yet. Still, relative to an YDFA, Raman gain is expected to reduce the coupling to other modes than the conjugate OAMM, if these can be considered incoherent with the target mode. This depends on the difference in effective index as well as the linewidth. It is also entirely possible that the gain saturation properties are unimportant compared to the lower mode-coupling that can be expected in a RGF, because of its high homogeneity.

In this chapter, I introduce our experiments on Raman amplification of OAMMs of first radial order. The amplifier performance and signal mode purity are reported and discussed. In section 5.2, a FRA for charge 2 circularly polarized OAMM in a 25-μm diameter core step-index fibre is first introduced. This experiment serves as a proof-of-concept experiment to verify the performance of FRA in a multimode step-index fibre. Also, methods to evaluate the purity of OAMMs of lower charge such as charge 1 or 2 have been reported and well acknowledged, which enables rigorous analysis of the amplifier design. The experimental setup is modified from the FRA for the Bessel-mode LP_{08} introduced in section 4.2. Then in section 5.3 I report Raman amplification of a charge 15 OAMM

in a 50-μm diameter pure silica core step-index fibre, with a setup adapted from the one introduced in section 4.3 and 4.4. This experiment is an addition and extension to the previous one with charge 2 OAMM. The target OAMM is now linearly polarized and chosen as we expect OAMMs of a higher charge show increased resistance to coupling into its degenerate OAMM of conjugate charges, which we elaborate in the following sections. The results are summarized in section 5.4.

5.2 Fibre Raman amplifier for $l = 2$ OAMM in a multimode step-index fibre

In this section I report our experimental setup and results of Raman amplification of a spin-orbit aligned (SOa) OAMM with $l = +2$, $s = +1$ in a multimode passive step-index fibre. A SOa OAMM is circularly polarized with the same handedness as the OAMM helix. As the amplifier for OAMMs shares similar principles with the one for Bessel HOMs, which was already discussed, we start with the experimental setup introduced in section 4.2 that utilizes a commercial YDFL as the master oscillator. A physical S-plate with laser imprinted nanogratings serves as the beam converter from the input Gaussian beam to an OAM beam. We have also added a mode decomposition setup to measure the purity of the signal OAMM. The results verify the viability of FRAs for power scaling OAMMs with high purity.

5.2.1 Experimental setup
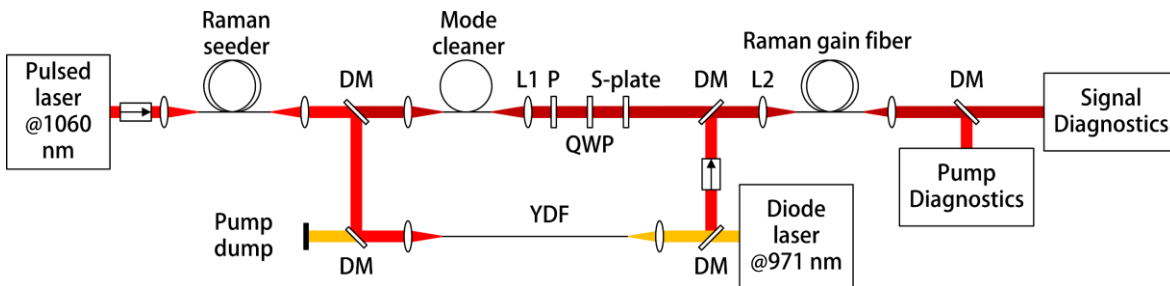
Figure 5.1: Schematic of the experimental setup for $l = 2$ OAMM Raman amplification. P – polarizer.

The schematic of the experimental setup is shown in Figure 5.1. It is similar to the setup used in section 4.2, but with modified signal mode converter, YDF pump booster and diagnostics. A master oscillator (G3, SPI Lasers) generates 1060-nm 60-ns pulses at a repetition rate of 4 kHz. The pulses pass through a 30-m Ge-doped fibre (Freelight, Pirelli) where SRS converts a portion of the pulse energy to 1115-nm Stokes. The mixed 1060-nm and 1115-nm beam are then collimated by an aspheric lens (f = 8 mm) and are separated into signal and pump arms by a DM. In the signal arm (top part of the setup), a 3-m long single mode passive fibre cleans up the signal beam, which then gets collimated by an aspheric lens (L1, f = 8 mm). A polarizer and a quarter waveplate (QWP) convert the signal beam into the desired circular polarization. An in-house made S-plate then converts the incident Gaussian beam into a vortex beam with $l = 2$ OAM [3]. The S-plate has a transmission

of ~72%. An aspheric lens (L2, f = 15 mm) launches the OAM beam into the core of the 5-m long RGF with ~41% efficiency. In the pump arm (bottom part of the setup), the remaining 1060-nm pulses from the Ge-doped fibre is amplified to ~1.3 mJ in a 5-m long YDF which is different from the one in section 4.2. The new double-clad YDF is fabricated in house and has a core with 55 μm diameter and 0.09 NA. Its inner cladding has a diameter of 725 μm with ~3.8 dB/m pump absorption at 976 nm. The YDF is 4° angle cleaved in both ends to suppress feedback from the fibre facets. A 971-nm CW DL (LDL 80-500, Laserline) pumps the YDF. Due to the increased length of the new YDF, the temporal delay between the signal and pump pulses in the RGF can be readily tuned by minor adjustments to the locations of the optics, so the delay line that was used in Figure 4.1 is removed. The boosted pump is combined with the Raman seed by a DM and is also launched into the core of the RGF with ~30% efficiency. The RGF (25/125 μm, No. 35275, OFS Inc.) is now a commercial but non-standard multimode fibre with a core diameter of 25 μm and NA of 0.12. Its measured refractive index profile is shown in Figure 5.2. Simulations with Comsol Multiphysics software show that the fibre supports 20 transverse modes at 1115 nm: $HE_{11}^{even/odd}$, TE_{01} , $HE_{21}^{even/odd}$, TM_{01} , $EH_{11}^{even/odd}$, $HE_{31}^{even/odd}$, $HE_{12}^{even/odd}$, $EH_{21}^{even/odd}$, $HE_{41}^{even/odd}$, TE_{02} , $HE_{22}^{even/odd}$, TM_{02} . The OAMMs supported in this fibre are $OAMM_{\pm 1,1}$, $OAMM_{\pm 2,1}$ and $OAMM_{\pm 1,2}$. The RGF is coiled with a 30-cm diameter and has both ends perpendicularly cleaved to minimize distortions to the signal beam.
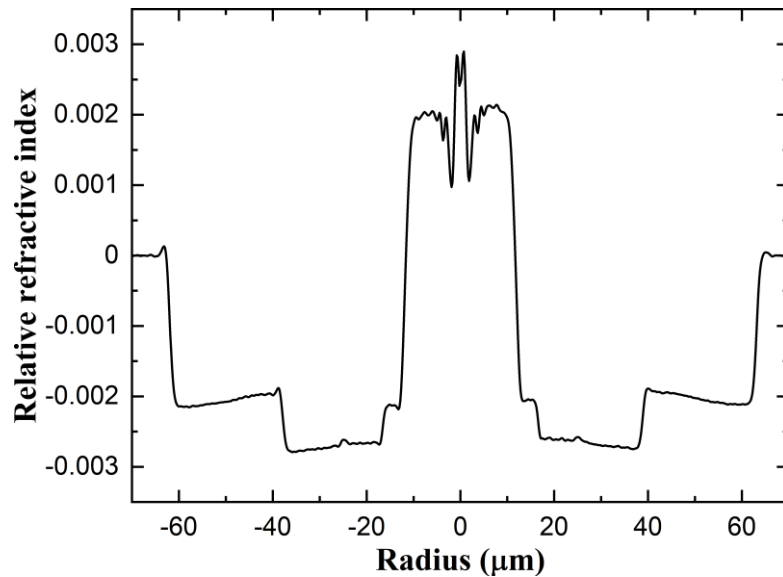
Figure 5.2: Measured refractive index profile of the OFS Raman gain fibre.

The S-plate used in the experiment are imprinted with radially symmetric nanogratings that produce space variant birefringence modulation [3]. An incident circularly polarized beam is then converted into optical vortices carrying OAM whose sign is determined by the handedness of the incident circular polarization. In our case, the beam incident to the S-plate has a left-handed circular polarization (SAM: $s = +1$), and the converted beam carries OAM with the same sign ($l = +2$). It follows that the excited OAMM in the RGF is the linear combination of HE_{31}^{even} and HE_{31}^{odd}. However,

due to the imperfect conversion by the S-plate, the transmitted unconverted light can excite the $l = 0$ modes. In addition, the 90-degree longitudinal phase difference between the two HE modes can be altered by azimuthally dependent perturbations and thus the SOa OAMM with the conjugate charge $l = -2$ can be excited, reducing the total OAM of the beam. If combined with an imperfect incident polarization state, SOaa OAMMs with $l = \pm 2$ can also be excited [4].

The output of the RGF is first collimated by an aspheric lens (L2, f = 11 mm) and then separated into signal and pump for their respective diagnostics. The average power is measured by two thermal power meters, the temporal traces are captured by 350 MHz Si detectors (DET10A2, Thorlabs) connected to a 6 GHz oscilloscope (Infiniium 54855A, Agilent), and the optical spectra are characterized by an OSA (AQ6317B, Ando).
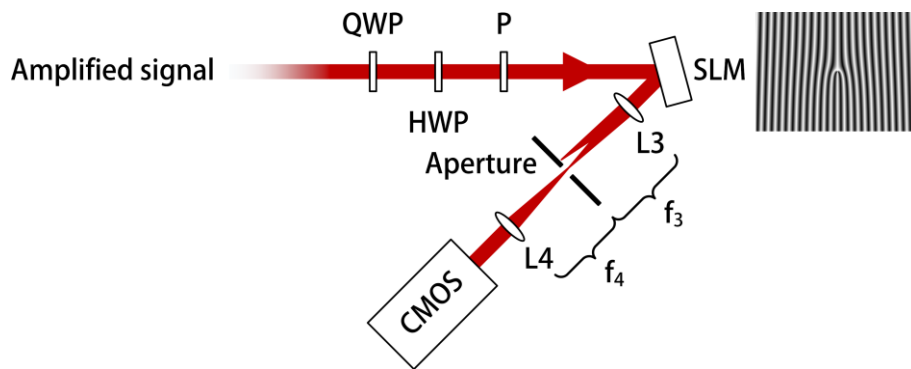

Figure 5.3: Schematic of the setup for mode purity measurement. A sample image of the forked SLM pattern of $l = -2$ is shown to the right of the SLM.

The output signal is also sent to a mode decomposition setup, shown in Figure 5.3, for purity characterization. A quarter waveplate (QWP), a half waveplate (HWP) and a polarizer first convert the output beam into linear polarization aligned to the preferred polarization direction of a SLM (SLM-100, Santec, also used in section 4.3). A series of holograms that incorporate the azimuthal phase distributions of OAMs with charge from $l = -4$ to $+4$ superimposed on the phase pattern of a blazed grating are displayed on the SLM. The additional grating serves to separate the modulated beam from specular reflection. These holograms are referred to as the forked patterns. They apply an extra phase term to the incident beam and the diffracted beam from the SLM has a wavefront with azimuthal phase altered by the amount corresponding to the displayed hologram. For instance, an incident OAM beam with charge $l = +2$ will have its azimuthal phase cancelled out if it is modulated by the hologram with the azimuthal phase pattern of charge $l = -2$, or partly compensated if the hologram has a phase pattern of $l = -1$. The far-field profile of the first order diffraction, which is essentially the Fourier transform of the field leaving the SLM [5], is imaged by a telescope comprising two lenses (L3, convex, $f_3 = 100$ mm and L4, plano-convex, $f_4 = 75$ mm) to a Si CMOS camera (DCC1545M, Thorlabs). The camera is placed at the focal plane of L4. The on-axis intensity of the far-field profile is thus proportional to the square of the integral of the SLM-modulated beam and is zero if the azimuthal phase change of the incident beam is not fully compensated. The

contributions to the on-axis intensity of fibre modes are proportional to their modal power, though with different constants of proportionality because of differences in the radial dependence of the modes [6]. OAMMs with non-zero charge numbers have donut-shaped distributions with one or several rings which correspond to the radial order. The phase alternates between rings, which leads to cancellation in the diffracted on-axis intensity for modes with higher radial order. For OAMMs of the lowest radial order and a non-zero charge, there is only one ring. Therefore, the difference in the radial distribution of modes with different charges can be assumed to be small, and the constants of proportionality between the on-axis intensity and the modal power are similar, at least for the OAMMs with relatively small azimuthal charge, such as from $l = +4$ to -4. The fundamental mode has a different field profile from the donut shaped OAMMs and has an estimated constant of proportionality which is ~80% of that of our target OAMM. This is estimated from the two-dimensional integral of the mode without azimuthal phase. For equal amount of power in the fundamental mode and in the target OAMM, the integral of the fundamental mode is 80% of the target OAMM. The fibre modes with radial order larger than one supported by the RGF are HE_{12}, TE_{02}, TM_{02} and HE_{22}. Of these, HE_{22} can form OAMM$\pm_{1,2}$. However, these modes with higher radial order will either have charge $l = 0$ or 1 and are expected to have small amounts of power, as suggested by our experimental results shown below. Therefore, we neglect the impact of power in fibre modes with radial order larger than one and determine the relative modal power and the mode purity of the target OAMM under the assumption that the power in a charge is dominated by the power in a single OAMM, with the same constant of proportionality to the on-axis intensity.
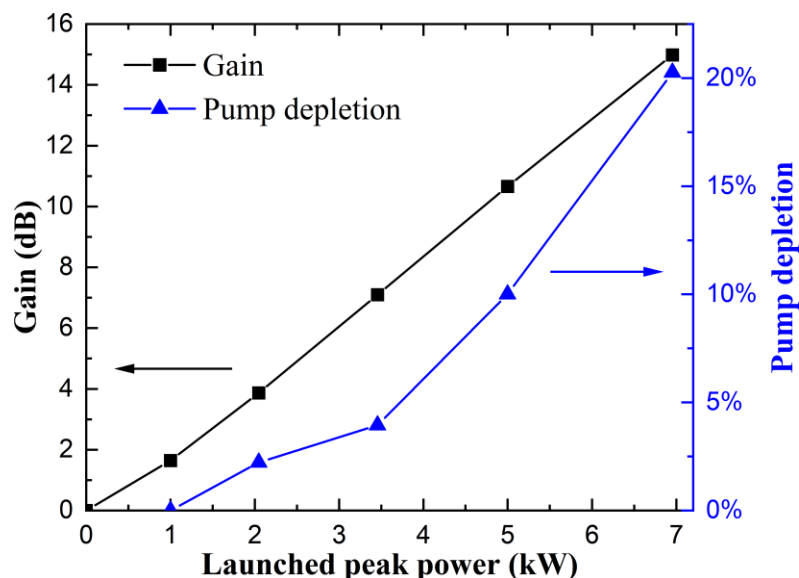
5.2.2   Results and analysis

Figure 5.4: Measured average power gain of the signal (left scale) and the pump depletion (right scale) versus launched pump peak power.

The average power gain and the pump depletion versus launched pump peak power are plotted in Figure 5.4. The Raman gain is calculated as the ratio between the average power of the transmitted signal with and without pumping. The pump peak power is calculated from the average pump power, the pulse repetition frequency, and the FWHM pulse width of ~55 ns. The energy between the pulses is considered small as the pulse energy at maximum pump power is less than the saturation energy of the YDF which is ~800 µJ. The pump depletion is the difference between transmitted pump average power with and without Raman seeding over the unseeded transmitted pump average power, which is different from the weighted pump depletion evaluated in Chapter 4. The pump depletion when unseeded is ignored as the unseeded Stokes has an average power of only 7.2 mW at maximum pump power. The maximum gain is 15 dB, with a pump of 1.53 W average power, 6.95 kW of peak power and 382 µJ of pulse energy. At this gain, the signal is boosted to 68.5 µJ of pulse energy and 4.5 kW of peak power, from 1.6 µJ pulse energy and 60 W peak power. The pump to signal conversion efficiency is 17.9%, and the average pump depletion is 20% at maximum gain. The Raman gain grows almost linearly to the maximum gain despite the pump depletion, which suggests that the depletion occurs mostly near the output end of the RGF and reduces the Raman gain in only a short piece of fibre. The gain slope is ~2.15 dB/kW and corresponds to a Raman gain coefficient of 48.7 fm/W with a core area of 1964 µm^2. This value agrees well with the expected value for unpolarized pump in silica fibres [7].
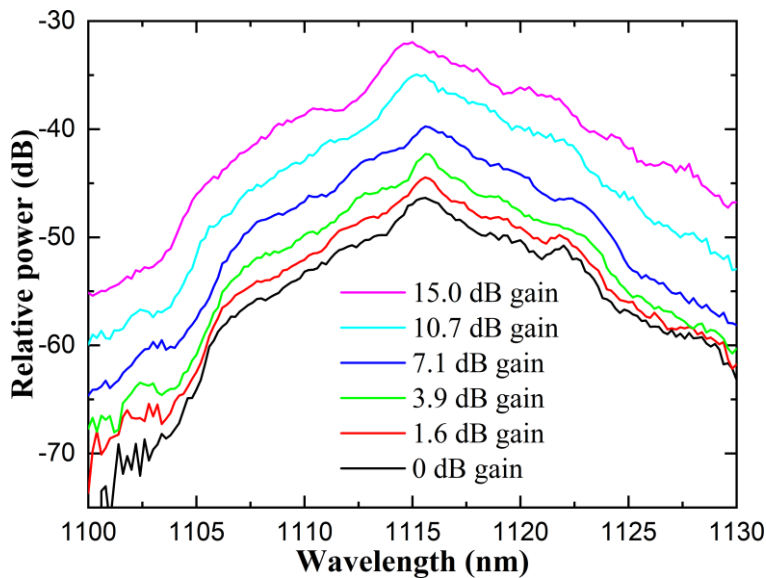
Figure 5.5: Measured optical spectra of the output signal at different gain levels. Resolution 0.2 nm.

The measured optical spectral of the transmitted signal are plotted in Figure 5.5, where 0 dB gain corresponds to the transmitted signal without pumping. The 3 dB linewidth of the signal at 15 dB gain is ~4.8 nm, compared to the ~3.9 nm linewidth of the signal at 0 dB. The spectral broadening is a result of the broad linewidth (~10 nm) and fluctuations in the intensity of the pump beam [8]. Therefore, the coherence of the signal beam is less than 100 µm, i.e., a few times 10^{-5} of the optical path length of the RGF, and thus the signal modes exiting the RGF are considered incoherent except

for the degenerate ones. Although outside the plotted wavelength range, the measured spectrum at maximum gain shows negligible power corresponding to the 2nd order Stokes.

Figure 5.6: Measured temporal traces of the incident pump (red curve) and signal (black curve) as well as the amplified signal at 15 dB gain (orange curve).

Figure 5.6 shows the temporal shape of the incident signal and the amplified signal with 15 dB gain in difference scales. The incident pump pulse at this gain level is also plotted. These pulses have similar shapes to the corresponding ones shown in section 4.2. The amplified signal pulse has a FWHM pulse duration of 14.9 ns, which is less than the width of 19.5 ns of the unamplified signal. The pulse shap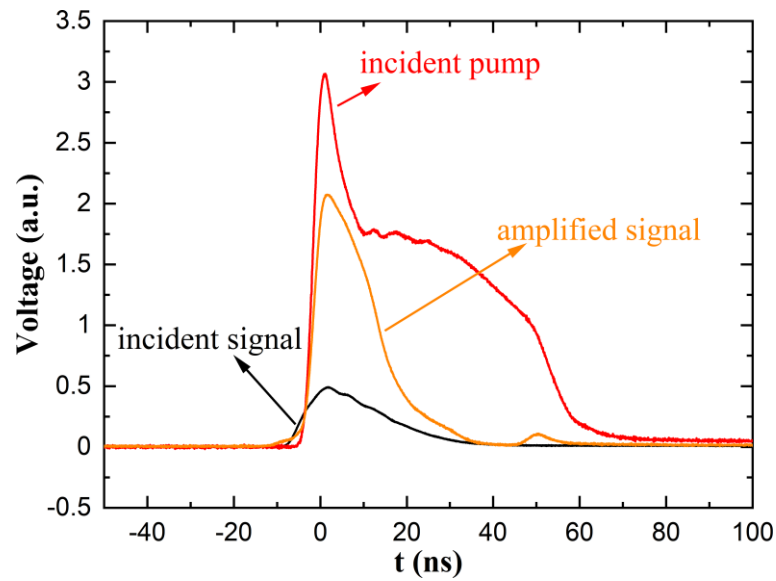e is also altered, with a sharper rising edge. This is due to the ~5 ns narrow peak in the leading edge of the pump pulse which has much higher instantaneous power and provides higher instantaneous Raman gain. A minor peak with amplitude ~5% of the main peak is observed ~48 ns after the main peak. Since the time difference equals the roundtrip propagation time of the signal pulse in the RGF, the minor peak is attributed to the signal power that has been doubly Fresnel-reflected from the perpendicularly cleaved fibre facets and amplified through three single passes through the fibre (one of which was in the backward direction, following a first Fresnel reflection). As mentioned in section 4.3, such reflections may cause detrimental oscillations, especially if the pump pulse is longer than the roundtrip propagation time in the fibre. We estimate the total backward signal output power to 10%-20% of the forward power. The measured temporal traces are visually stable with minor broadening, and the pump and signal peak values drift only by ~5% long-term. The drifts are mainly caused by the unstable master oscillator and the SRS process in the Ge-doped Raman seeder.
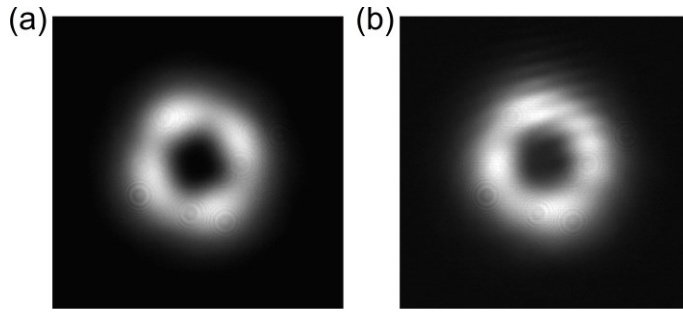
Figure 5.7: Intensity profiles of the transmitted signal at 0 dB gain (a) and at 15 dB gain (b). The images are in linear scale and normalized to the maximum intensity for better visibility.

The intensity profiles of the transmitted signal without pumping and with 15 dB gain, measured from the 1st order diffraction of the SLM with hologram corresponding to $l = 0$, are shown in Figure 5.7. The profiles are similar except for extra fringes in the amplified signal. These fringes are caused by the variable reflective attenuator in front of the camera for the amplified signal beam and do not affect the mode decomposition results.

In the mode purity characterization, the output signal beam is converted from circular polarization to linear polarization by a QWP, and then has its polarization orientation rotated to the working direction of the SLM by a HWP. A polarizer filters out power in other polarizations. The filtered beam is visually stable in both the short term and long term, indicating a stable polarization of the incident beam. Given the different polarization states associated with the OAMMs, the power in other polarizations may come from birefringence in the fibre induced by bending that couples the signal mode into SOa OAMMs formed by HE modes but in opposite charge, into SOaa OAMMs formed by EH modes in the same charge, or into charge 0 modes. We have measured the ratio of power in the dominant polarization over the total power to ~94% for the unamplified signal by measuring the power in both directions of the polarization after converting the beam back to linear polarization. This indicates high degree of preservation of the circular polarization of the signal beam and low linear birefringence in our RGF [9]. Furthermore, by using unpolarized pump, the Raman amplification is expected to be polarization independent and not degrade the polarization purity significantly. Therefore, we disregard the power in other polarizations in our mode purity assessment.
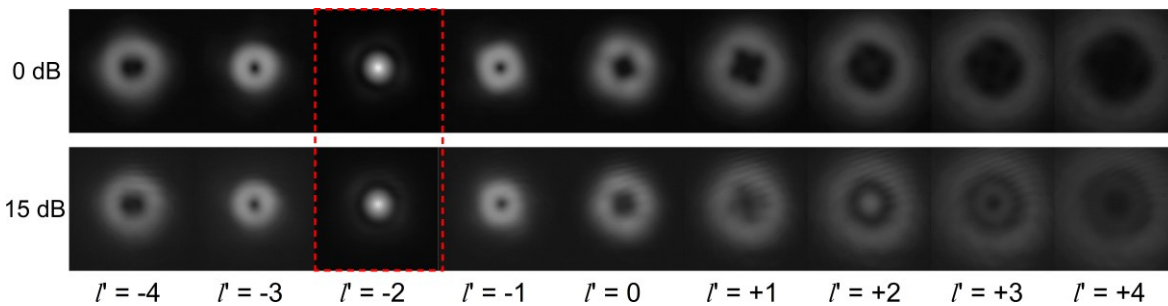

Figure 5.8: Images of the decomposed signal beam with holograms corresponding to OAMM with different charges. Bottom row shows the images for amplified signal at 15 dB gain. Brightness and contrast of the images are adjusted for better visibility.

Decomposed signal beams at 0 dB and 15 dB gain, captured at the focal plane of the imaging lens L4, are shown in Figure 5.8. The different intensity profiles are observed when the holograms on the SLM are swept from azimuthal phase pattern corresponding to OAMM with charge $l' = $ -4 to +4. The associated on-axis intensity is hence proportional to the modal power in OAMM with charge $l = $ +4 to -4. Therefore, the purity of each mode is given by the ratio of its corresponding on-axis intensity over the sum of the on-axis intensities for all the modes.
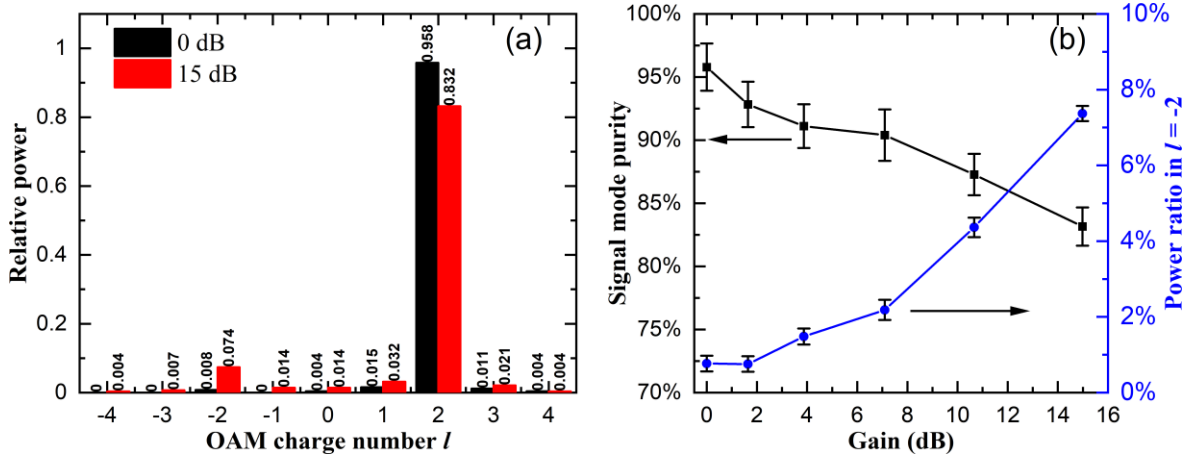

Figure 5.9: (a) Fraction of power in the output signal versus charges from -4 to +4 for 0 dB and 15 dB gain. (b) Mode purity of $l = $ +2 OAMM and the fraction of power in $l = $ -2 versus the Raman gain.

The signal beam incident to the RGF has a measured purity of the target OAMM of ~97.4%. The purity becomes ~95.8% for the transmitted signal at 0 dB gain and then drops to 83.2% at 15 dB gain. The small size of the purity degradation after fibre propagation indicates that the RGF is capable of preserving the target OAMM. The relatively higher purity drop after amplification therefore could be a result of mode-selective gain saturation, increased mode coupling in the fibre and / or degraded OAM launch alignment. The breakdown of the signal modal content at both 0 dB and 15 dB gain is plotted in Figure 5.9(a). At 0 dB gain, the unwanted power is mostly in the neighbouring charge $l = 1$ and 3, each having 1~2% total power. The power in the opposite charge $l = $ -2 is ~0.8%. At 15 dB gain, there is an increase in power in all the unwanted modes, with significant power in the opposite charge $l = $ -2 which accounts for 50% of the overall purity degradation. The evolution of signal mode purity as well the ratio of power in $l = $ -2 at different gain levels are plotted in Figure 5.9(b). Here, the estimated ratio of power has an uncertainty of ~±2% for the target charge and ~±0.2% for the other charges due to the 8-bit digitization of the camera. Overall, the mode purity drops almost linearly with the increase in logarithmic gain. However, at ~1.6 dB gain, the purity quickly drops by ~3% where there is negligible pump depletion and almost no extra power in the opposite charge -2. At higher gain, the power in $l = $ -2 starts to pick up and eventually represents ~50% of the overall purity degradation at maximum gain. This is not explained by pump depletion induced mode-selective gain saturation, as the intensity distributions of OAMMs with $|l| = 2$ are identical and the opposite charge is not less affected by the pump depletion. Furthermore, despite low pump depletion, the depleted pump profile would favour the fundamental mode as its overlap with the target OAMM

is low. However, the modal content for $l = 0$ after amplification sees only minor increase. This indicates that mode-selective gain saturation does not significantly reduce the mode purity. Another possible reason is drifted signal mode launch such as tilt and offset of the incident beam that causes an overall increase in power in unwanted modes, especially in the OAMMs with neighbouring charges, as the pump power increases. However, in this case, most power is expected to be transferred to $l = 0$, 1 or 3 modes, which is different from the results shown in Figure 5.9(a). A third possible reason is coupling from SOa OAMM with $l = +2$ into SOaa OAMM with $l = -2$. From a vector mode picture, such coupling occurs between the quasi-degenerate HE and EH modes. Additionally, coupling between OAMMs with the opposite charge can be a result of the dephasing between the degenerate even and odd HE or EH modes that form these OAMMs. In this case, coupling between the polarizations with the opposite handedness is also expected. Since we have concluded the polarization purity is high and disregarded the power in other polarizations, the extra power in charge $l = -2$ is most likely a result of coupling into EH_{11} modes that form the SOaa OAMMs with $s = +1$. In our RGF, the effective index splitting between the HE_{31} and EH_{11} mode pairs that form $|l| = 2$ OAMMs (i.e., the splitting between the SOa and SOaa OAMM), is $\sim 6 \times 10^{-7}$, which is considerably smaller than the index splitting of $\sim 10^{-4}$ often considered required for stable mode propagation [9]. The beat length becomes ~ 1115 nm / $6 \times 10^{-7} = 1.9$ m. Therefore, fibre imperfections and bends are highly likely to couple power into $l = -2$ OAMM. Although it is reported that OAMMs are more resistant to coupling into their degenerate counterparts with opposite charges than the vector modes that form the OAMM, as it involves changing the OAM by $|2l|$ [10], such coupling may still occur for OAMMs with low l. Nevertheless, we believe further investigation is needed to clarify if the excessive power in $l = -2$ is a result of coupling into the quasi-degenerate OAMM. Contrarily, coupling into OAMMs with the nearest neighbour charges is expected to be small, as the effective index separation is considerably larger than the 10^{-4} criterion for stable propagation. For instance, the index separation between the vector modes that form $|l| = 2$ and 1, or $|l| = 2$ and 3, are $\sim 7.3 \times 10^{-4}$ and $\sim 8.9 \times 10^{-4}$, respectively. This is supported in Figure 5.9. Likewise, the coupling into the higher radial order OAMMs is expected to be much less as the effective index separation from the target OAMM is even higher ($\sim 1.4 \times 10^{-3}$).

Increasing the pump peak power to 8.7 kW improves the Raman gain to ~ 18 dB in terms of average power and the pump depletion to $\sim 30\%$. However, at this gain level, the unseeded Stokes power grows quickly to almost 11% of the seeded Stokes and the signal mode purity degrades substantially. Here, the seeded target mode gets amplified while the unwanted modes that are unseeded also receive considerable amount of power via unseeded SRS. In addition, the Fresnel reflections from the perpendicularly cleaved fibre facets exacerbate the purity degradation from unseeded SRS. From the analysis in section 4.3, the pump pulse duration of ~ 50 ns is slightly larger than the signal roundtrip propagation time of ~ 48 ns and may lead to substantial parasitic oscillations when the single pass gain exceeds 14 dB. As a result, the signal reflected from the output end will, when it exits the signal launch end of the fibre, have similar or higher total gain (i.e., after reflection losses have been

subtracted) as the forward signal. A similar effect occurs for the double reflected signal pulse, which thus can see higher total gain than the single-pass gain. Accounting for the temporal shape of the pump pulse, the trailing part has only ~50% instantaneous power of the peak and thus the actual time-averaged gain for the reflected signal is reduced. Nevertheless, this can still cause rapid growth of unseeded doubly reflected SRS in unwanted modes. To resolve this issue, fibre endcaps may help by minimizing the feedback from facets. Alternatively, pump pulses with shorter duration can be used to reduce the gain for the reflected signal, as the case in section 4.3 and 4.4.

In conclusion we have experimentally demonstrated Raman amplification of a single OAMM of $l = +2$, $s = +1$ in a 5-m commercial step-index passive fibre with up to 15 dB average power gain with multimode pumping. The purity of the target OAMM is well preserved throughout amplification, dropping from 95.8% at 0 dB gain to 83.2% at 15 dB gain. The degradation of mode purity of the amplified signal is mainly attributed to coupling into the OAMM with the opposite charge. The pump to signal conversion efficiency is ~17.9% with an estimated brightness enhancement of 8 dB. To the best of my knowledge, this is the first demonstration of FRA for OAMMs with high gain, high peak power, and high purity. It extends the usage of FRA for HOMs to a new regime and showcases the great potential for power scaling optical beams carrying OAM with high purity and flexibility.

5.3   Fibre Raman amplifier for $l = 15$ OAMM in a large core step-index fibre

Fibre OAMMs with higher charge numbers have seen a growing interest recently in several applications including mode-division multiplexing [11-13]. Rare-earth doped power amplifiers for such high charge OAMMs or the vector modes that form them have been proposed or demonstrated in either ring core fibres [14, 15] or photonic crystal fibres [16]. However, precise control of the active dopants in the designated region is challenging and such doping can introduce extra perturbations in the fibre. In addition, most of the proposed amplifiers require a donut-shaped pump intensity profile to match the refractive index profile of the fibre, which demands extra work and can also limit the available pump power. It is also possible to cladding pump the OAMMs. However, cross-sectional shaping of the inner cladding which breaks the circular symmetry of the cladding and enhances pump absorption may induce distortions to the structure of the ring-shaped core and cause ellipticity [17]. Therefore, the pump absorption can be weak.

Alternatively, step-index FRAs can be used for these high charge OAMMs. So far, FRAs have been demonstrated as a viable approach for power scaling of HOMs in multimode step-index fibres with excellent mode purity. These HOMs include high order Bessel modes as well as OAMMs that can be described as pairs of degenerate modes. The preservation of signal mode purity is attributed to the non-local gain saturation of Raman scattering, the large effective index splitting between modes that are otherwise likely to couple (e.g., modes with neighbouring mode index), and the gain media with

good refractive index control that also reduces mode coupling. For Bessel HOMs, ignoring possible polarization degeneracy and in the absence of accidental degeneracy, the target mode is non-degenerate. Therefore, in the analysis, all modes can be considered non-degenerate and coupling between the degenerate modes can be ignored as it does not directly affect the purity of the target mode. This makes it possible to reduce the mode-coupling between the target mode and other modes by increasing the mode spacing. Contrarily, in the absence of circular birefringence, an OAMM is always degenerate with its conjugate. It is also quasi-degenerate with the mode of opposite SAM. Thus, coupling between the degenerate or quasi-degenerate modes can impair the mode purity, as is shown in section 5.2 where the purity degradation is mainly attributed to coupling into the quasi-degenerate modes. In this regard, OAMMs with higher charge numbers are favoured as they are reported to be more stable against coupling into the conjugate mode [9, 10]. This points to the possibility of better mode purity preservation.

In this section, I discuss our experimental results of Raman amplification of linearly polarized first radial order OAMM with charge 15 in a 30-m fibre with a core of 50-µm diameter and 0.227 NA. The average power gain reaches 9.2 dB with signal mode purity of ~78.4%. This is to the best of my knowledge the first demonstration of Raman amplification of an OAMM with such high charge in a large core fibre.
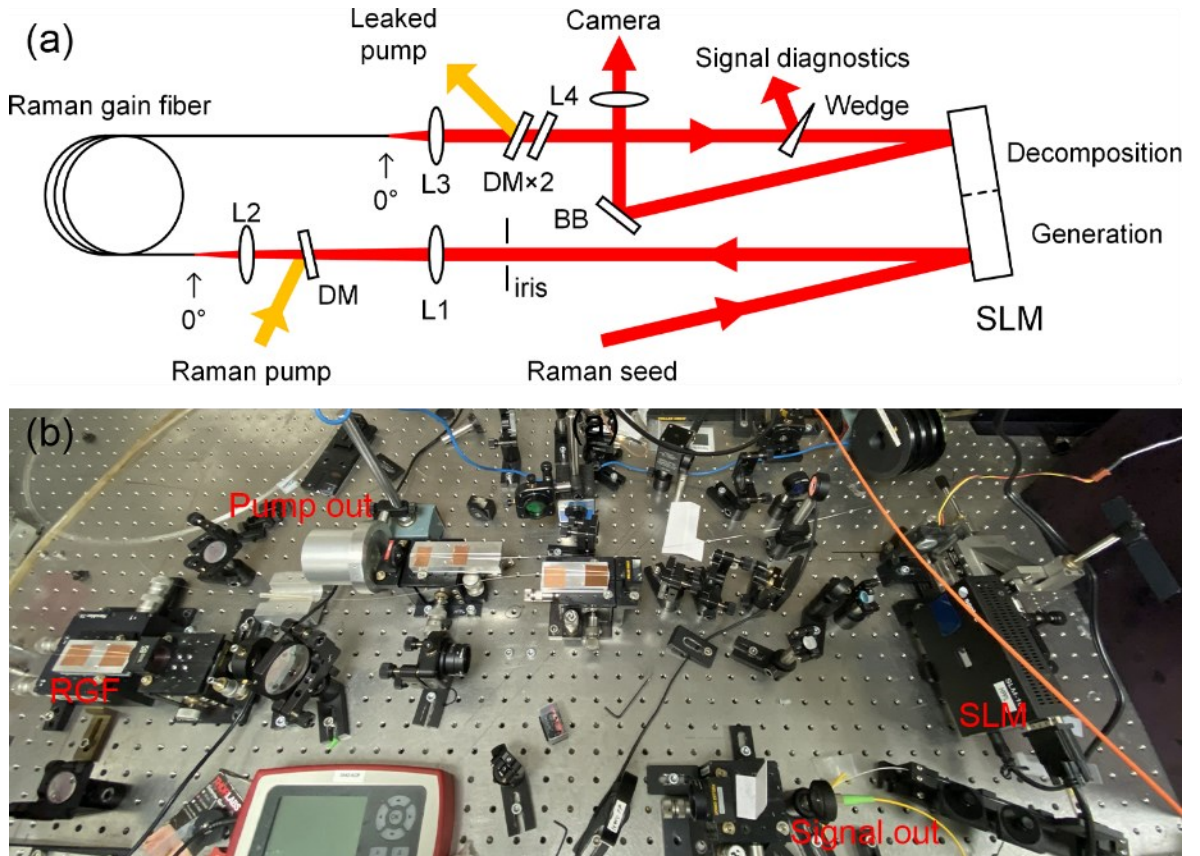
5.3.1　Experimental setup

Figure 5.10: (a) Schematic of the experimental setup for charge 15 OAMM Raman amplification. (b) Picture of part of the setup. The RGF and the camera are not shown.

The schematic of the experimental setup is shown in Figure 5.10. The Raman seed source is similar to the one introduced in section 4.4 except for a different triggering configuration (see Figure 5.11). The drivers for the 1060-nm DL and the 1121-nm DL are not controlled by a DDG but by the aforementioned AFG and AWG, respectively. The AWG also controls the diode driver for the 1060-nm DL in the Raman pump source. The emitted Raman seed comprises 1121-nm 2 ns pulses at 20-kHz repetition rate and is collimated by a plano-convex lens (f = 100 mm, not shown) and are linearly polarized with a polarization orientation aligned to the working axis of the SLM by a fibre PC (same as in section 4.4, not shown). The SLM is used in section 4.3 and 4.4 and is now partitioned into two horizontal halves to support both the generation of the target OAMM and the decomposition of the incident beam through optical correlation. An iris blocks unwanted orders of diffraction from the SLM. A pair of aspheric lenses (L1, f = 200 mm and L2, f = 8 mm) are used to launch the generated OAM beam into the core of the RGF. The Raman pump source is also introduced in detail in section 4.3.1 (see Figure 4.9) and emits 1061 nm 4.5 ns pulses at 20-kHz repetition rate. The pump beam is collimated by an aspheric lens (f = 11 mm, not shown) and combined with the seed beam by a DM. L2 also launches the pump into the core of the RGF. The RGF is a 30-m step-index fibre with a pure silica core of 50-μm diameter and 0.227 NA. The fibre is the same type as the 10-m fibre used in section 4.3. The fibre is coiled with ~50 cm diameter and have both ends perpendicularly cleaved to

minimize distortions to the signal beam. The background loss of the RGF at ~1 μm wavelength is ~1 dB/km and is ignored for a length of 30 m. Pump pulses with up to 4.56 kW of peak power and 18.3 μJ of pulse energy are launched into the core. Note that the pump launch is aligned for the highest measured Raman gain for the signal at each pump level. This is expected to improve the excitation of pump modes with good spatial overlap with the donut shaped signal. The temporal overlap between the pump and signal is adjusted via the controls of the diode drivers of the seed and pump sources, as described in section 4.3. The RGF output is first collimated by an aspheric lens (L3, f = 11 mm) and separated into pump and signal arms by two consecutive DMs. The reflected transmitted pump beam and the signal beam that is reflected by a wedge prism are sent to their respective diagnostics, which include a thermal power meter for the pump, a Ge power sensor for the signal, two 12.5 GHz InGaAs detectors (ET-3500) connected to a 6-GHz oscilloscope (Infiniium 54855A, Agilent) and an OSA (AQ6317B, Ando). The transmitted signal continues to the beam decomposition which is discussed in detail later.
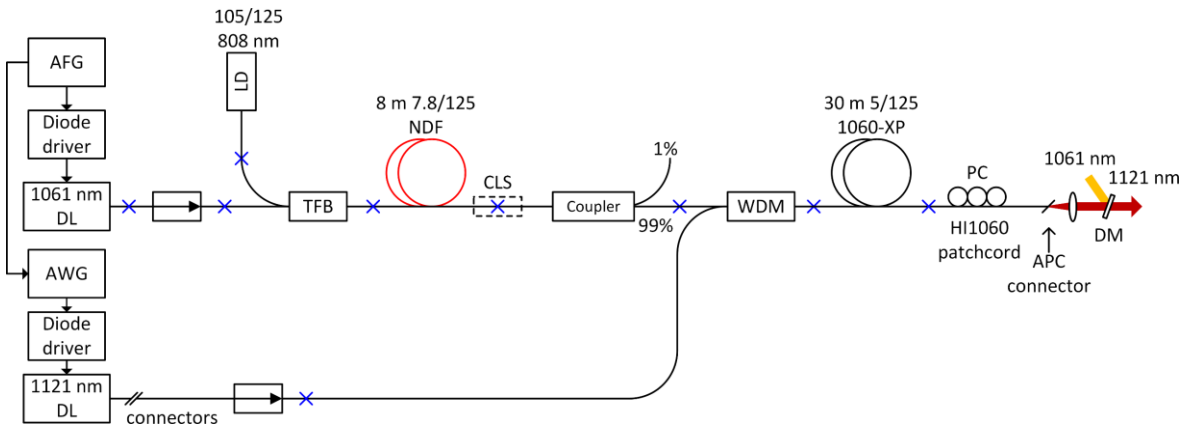

Figure 5.11: Setup for the Raman seed with modified pulse controls. Updated from the one in section 4.4.

The RGF has a V-number of 32.2 at 1121 nm and supports first radial order OAMM with charge number up to $l = 21$. I have attempted launching OAMM with various charge numbers and the modes with $l > 10$ can propagate stably without significant distortions in the 30-m RGF. The signal OAMM has an azimuthal charge number of 15 and radial order of 1. This mode is selected as a compromise between the stability of the mode and the resolution of the SLM. In a multimode fibre, the coupling between two modes under perturbations is expected to be suppressed if the effective index separation between them is large [18]. For OAMMs with azimuthal charge number of $l \neq 0$, coupling between the degenerate conjugate modes requires an additional change of OAM of $|2l|$. As the charge number increases, such coupling becomes harder [9, 10]. In addition, the index separation between the quasi-degenerate HE/EH modes that form the SOa and SOaa OAMM with the same azimuthal charge increases with the charge number, as shown in Figure 5.12(a). Compared to the value of charge 2 OAMM in section 5.2 which is 6×10^{-7}, the index separation for $l = 15$ is almost one order of magnitude higher, 4.4×10^{-6} (beat length 1121 nm / 4.4×10^{-6} = 25 cm). Although such index separation is still much smaller than the 10^{-4} criteria for stable propagation, the coupling between the

HE and EH modes is expected to be reduced. The effective index separation between OAMM with neighbouring charges also increases as the charge number increases. For $l = 15$, the index separations from $l = 14$ and $l = 16$ are 6.9×10^{-4} and 7.2×10^{-4}, respectively. Therefore, higher charge OAMMs are generally expected to be more stable. However, the index separation between the OAMM and its nearest neighbour mode does not show a clear trend versus the charge number. This is expected, given the "quasi-random" nature of the precise values of the modal effective indices in a highly MM fibre. Thus, Figure 5.12(b) shows the OAMM with charge 15 to have higher effective index separation compared to its neighbouring OAMMs, but note that I have not investigated how sensitive this is to deviations in the RIP. Another concern is the limited resolution of the SLM. OAMMs with higher charge number have much fewer pixels per unit phase change, which can severely degrade the purity of the converted beam. We have experimentally tested OAMM with other charges and $l = 15$ yields best results in terms of generated mode purity. Note that we launch a linearly polarized OAM beam into the RGF. As a result, from a vector mode perspective, both SOa and SOaa OAMM which are circularly polarized with opposite handedness, are expected to be excited in the fibre. Therefore, the target OAMM used in the experiment comprises quasi-degenerate mode pairs. However, coupling between them will only affect the state of polarization, but not the charge. The target OAMM can then be understood as a scalar OAMM for which the coupling of the SOa and SOaa will not degrade the purity.
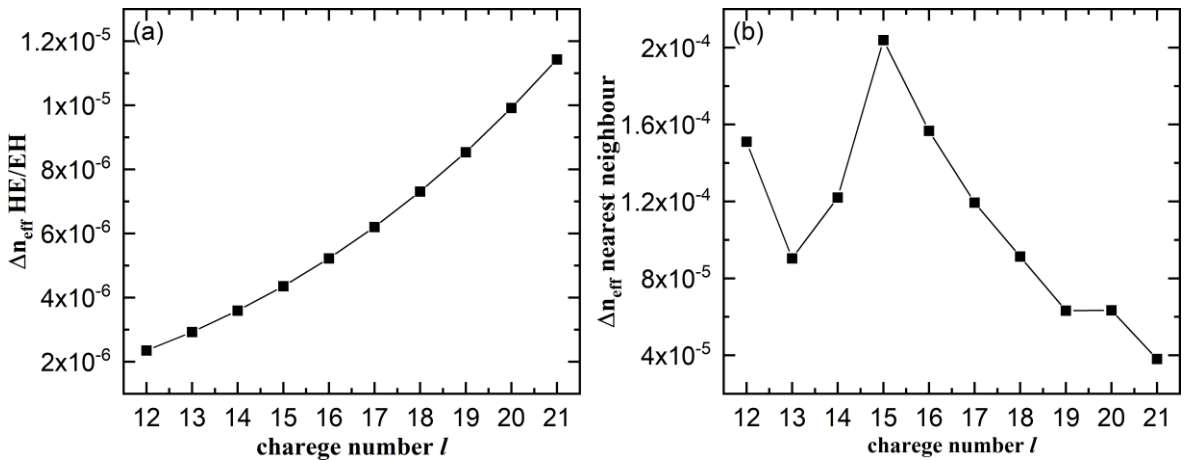
Figure 5.12: (a) Effective index separation between the quasi-degenerate HE and EH modes versus charge number l. (b) Effective index separation between the OAMM and its nearest neighbour mode versus charge number.

Since the forked pattern used in section 5.2 can yield a hologram with poor phase resolution in the centre if the charge number is high, the holograms for generating and decomposing the OAMM (shown in Figure 5.13) now incorporate both the amplitude and phase information of the free-space LG beams corresponding to the different OAMMs for optical correlation [19]. Since the SLM only modulates linearly polarized light, the holograms for the SOa and SOaa OAMMs of a specific charge and radial order are assumed to be the same.

Figure 5.13: Sample of the greyscale pattern displayed on the SLM with the region for OAMM generation and decomposition labelled.

The SLM includes amplitude information by encoding it to a phase function with Arrizon's algorithm [20]. For any complex field $s(x,y)$ with amplitude function $a(x,y)$ and phase function $\theta(x,y)$, it can be represented using a phase modulation function $\Psi(a,\theta)$ which is given by
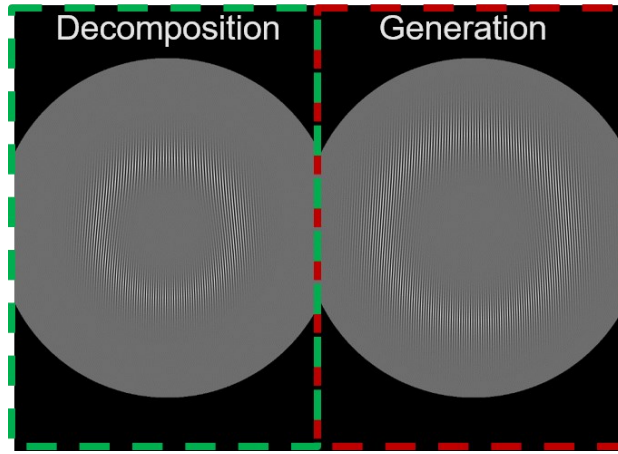
$$s(x,y) = a(x,y)\exp(i\theta(x,y)) \tag{5.1}$$

$$\Psi(a,\theta) = f(a)\sin(\theta) \tag{5.2}$$

where $f(a)$ is determined in a later step. When an incident beam with electric field U is phase modulated with the hologram function $\Psi(a,\theta)$, the reflected beam becomes $U\exp(if(a)\sin(\theta))$ and can be expanded as a Fourier series,

$$U\exp(if(a)\sin(\theta)) = U\sum_{-\infty}^{\infty} J_m\big[f(a)\big]\exp(im\theta) \tag{5.3}$$

where J_m is the Bessel function of the first kind with order m. The first order component therefore is identical to the phase structure of the complex field $s(x,y)$. The factor $f(a)$ in equation (5.2) is now determined by solving the relation

$$J_1\big[f(a)\big] = Aa, \tag{5.4}$$

where A is a constant and is determined to ~0.582 for the holograms we use. To separate the first order component, a grating is added to the phase structure and the first order diffraction is our target OAMM.

In this experiment, the Raman seed incident to the SLM is collimated by a 100-mm focal length lens with a clear aperture of 25 mm diameter. The beam is then clipped by an iris with an opening diameter of ~8 mm. If unclipped, the incident beam has a diameter of approximately 24 mm and the intensity deviation across the central region of 8 mm diameter is ~10% of the maximum value. Therefore, the

incident beam that overlaps with the hologram for the OAM beam generation can be approximated with a top-hat distribution. The hologram is thus the field of the target OAMM encoded with Arrizon's algorithm and can be easily implemented. However, over 95% of the Raman seed power is clipped by the iris or lost during the conversion process, and ~50% of the power incident to the RGF is launched into the core, leaving the total launched power only ~2.5% of the Raman seed power. This is not ideal for power scaling but note that there are other more efficient ways than clipping to convert the Gaussian beam to a top-hat beam. Alternatively, the phase pattern displayed on the SLM can be modified to match an incident Gaussian beam. However, these methods have not been attempted yet.
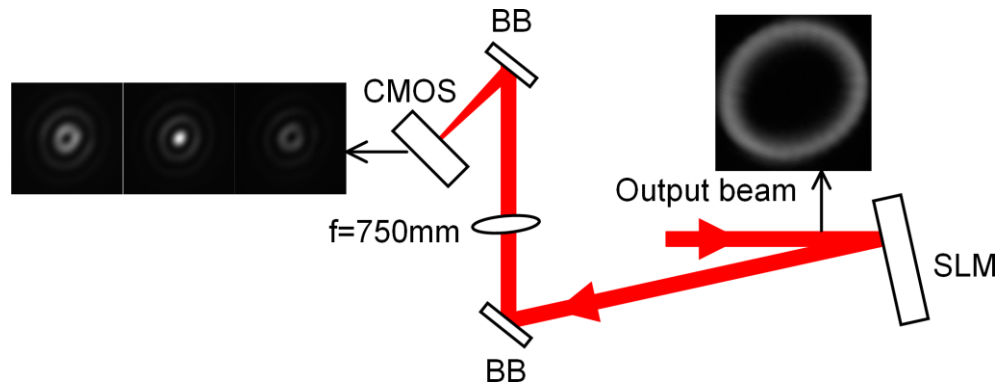

Figure 5.14: Setup for mode decomposition of the output signal beam. The images show examples of the output beam (right) and the decomposed beam (left). BB – broadband mirror.

The setup for modal decomposition is shown in Figure 5.14. The fibre output U can be represented by a superposition of OAMMs (which are normalized) in the fibre with corresponding weights W:

$$U = \sum_{l,m} W_{l,m} \text{OAMM}_{l,m} . \tag{5.5}$$

The weight of a mode can be calculated by optically correlating the incident beam with its complex conjugate $\text{OAMM}_{l,m}^{*}$:

$$W_{l,m} = \iint U \cdot \text{OAMM}_{l,m}^{*} r dr d\phi . \tag{5.6}$$

The purity of our signal mode is therefore given by the ratio between the squared weight of the target mode and the sum of the squared weights of all the modes that are swept on the SLM. Here, the SLM displays phase patterns that encode the amplitude and phase structures of a series of OAMM. A Fourier lens collects the first order diffraction of the modulated beam and performs the integral operation and the on-axis intensity at the Fourier plane of the lens gives the intensity weight. The intensity value is measured by a Si CMOS camera. More than 50 OAMMs with different azimuthal and radial orders, excluding the charge 0 ones, are supported in this fibre. However, the coupling to most of these modes is expected to be low. Therefore, it is reasonable to only consider OAMMs that the target mode is most likely to couple power into, including those with neighbouring and opposite

charges. Decomposing into OAMMs with radial order larger than one is also not implemented here for simplicity and left for future investigations. Nevertheless, the modal decomposition results are reasonable approximations, given the low coupling expected into excluded modes.
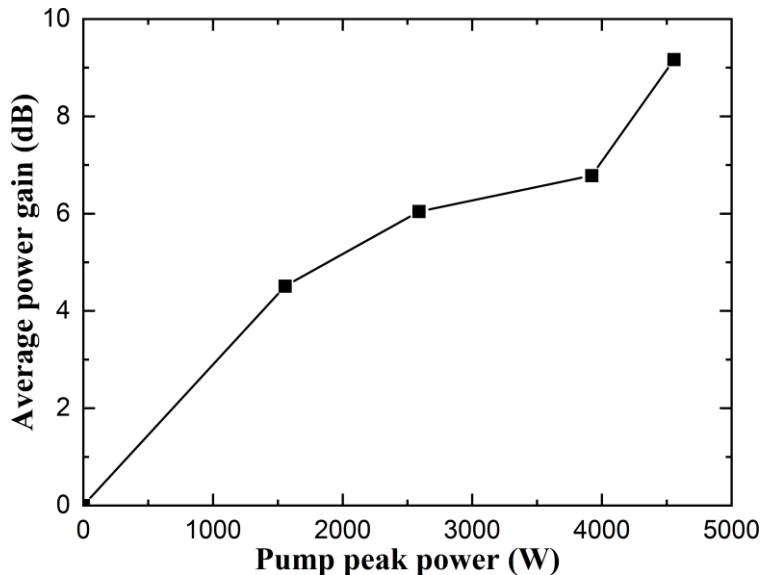
5.3.2 Results and analysis

Figure 5.15: Measured average power gain versus launched pump peak power. Gain calculated with subtraction of the pump that leaks into the signal diagnostics.

The average power gain versus the launched pump peak power is shown in Figure 5.15. The Raman gain is calculated as the ratio of measured average power of the transmitted signal with and without pumping after subtracting the pump power that leaks into the signal diagnostics. The background losses in the RGF are neglected. A maximum of 9.2 dB average power gain is reached, where the transmitted signal has a peak power of 5.41 W and pulse energy of 9.2 nJ after subtracting the leaked pump. At this gain, the launched pump peak power is 4.56 kW with 18.3 μJ of pump pulse energy. As the intensity distribution of the pump beam varies, the pump launch is adjusted for maximum measured signal output power at different gain levels. This seems to be the most likely reason why the gain is not growing linearly with launched pump peak power. I have also repeated the experiment without tuning the pump launch during amplification. The growth of gain is almost linear but overall less than the results presented here. Note that the pump and signal frequency shift in this experiment is ~15.1 THz (1061 nm to 1121 nm). In silica, the Raman gain coefficient for this frequency shift is therefore reduced to ~66% of the peak value of 50 fm/W for an unpolarized pump at 1061 nm. Using the reduced gain coefficient of 33 fm/W, the effective area at each gain level is calculated to be in the range of 1483 to 2486 μm^2. An effective area that is larger than the fibre core area of 1963 μm^2 indicates non-ideal overlap between the pump beam and the signal OAMM.
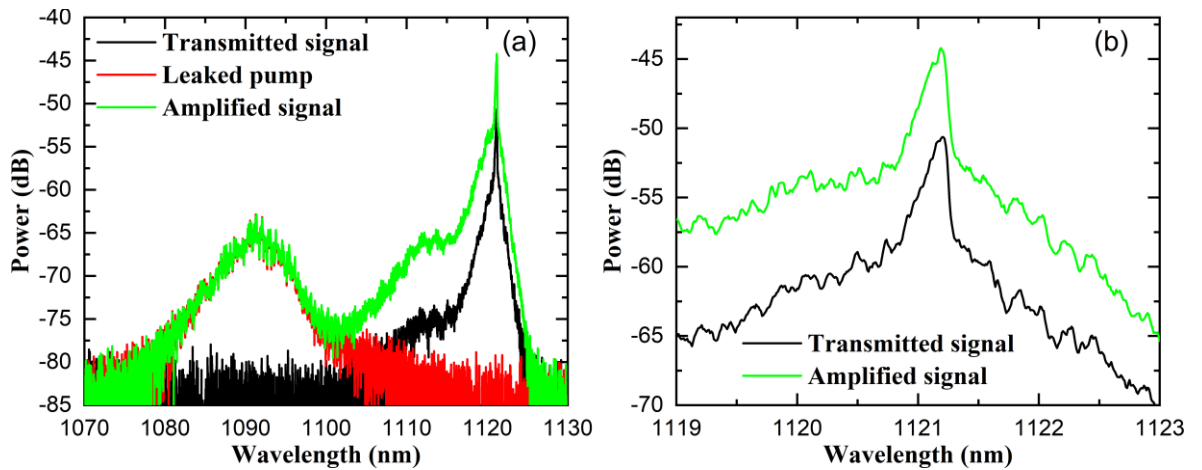
Figure 5.16: (a) Optical spectra of the transmitted signal at 0 dB gain (black), at 9.2 dB gain (green), and the transmitted light with pumping but no Raman seed (red). (b) Zoomed-in spectra of the transmitted signal with and without amplification. Measured with OSA resolution of 0.05 nm.

The measured spectra of the output signal at 0 dB gain (no pumping) and at 9.2 dB gain are shown in Figure 5.16(a). Zoomed-in spectra at around 1121 nm are shown in Figure 5.16(b). A peak at ~1090 nm that is ~20 dB lower than the signal peak is visible in the spectrum for the amplified signal. The peak also shows up at the same pump level but with the Raman seed blocked. This is the leaked longer wavelength component of the Raman pump light through the two DMs which have transmission edges at ~1090 nm. Since the amplified signal has a low average power of ~250 µW, the leaked pump of ~70 µW cannot be neglected and needs to be subtracted. Such pump leakage can also be seen in the measured temporal trace of the amplified signal, as shown in Figure 5.17. The amplified signal has a pulse duration of 1.7 ns which is similar to the unamplified pulse with 1.8 ns duration, while the duration of the transmitted pump is 4.5 ns. There is a small peak 9 ns behind the main peak with ~10% of the max amplitude in both the transmitted and amplified signal traces. The delay between the peaks corresponds to a roundtrip propagation over 1.3 m of free space or through 0.9 m of fibre, which is much shorter than the fibre length. Therefore, the extra peak is not explained by the reflection at the fibre ends and requires further clarification.
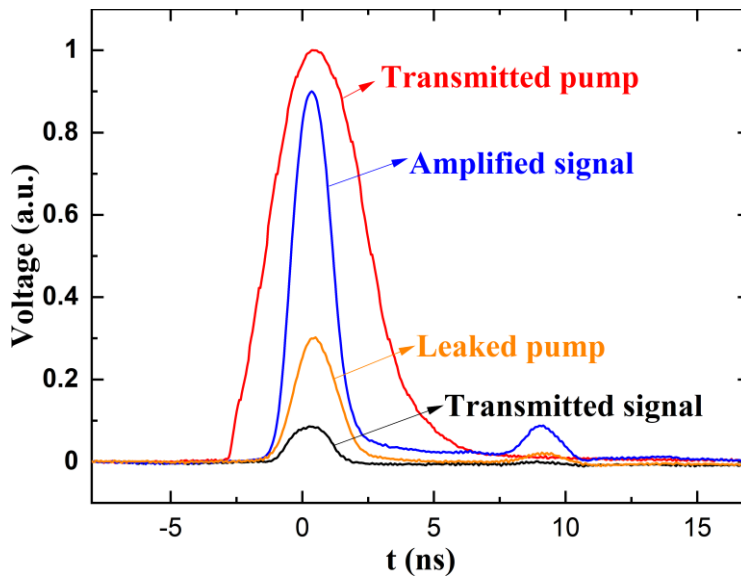
Figure 5.17: Temporal traces of the transmitted signal pulse without pumping (black curve), at 9.2 dB gain (blue curve) and the leaked pump pulse (orange curve). Launched pump pulse at 9.2 dB gain level is also plotted (red curve) with a different scale.

The measured intensity profiles of the transmitted signal at 0 dB and at 9.2 dB with subtraction of leaked pump are shown in Figure 5.18. The intensities are in linear scale and normalized to their maximum value for better visibility. Note that the rings for both beams are not perfectly circular. I tentatively attribute this to the aberrations in our optical setup, believed to be mostly from the off-axis illumination of the SLM. Such distortions are also observed in the decomposed beams and resemble the intensity distributions of OAM beams after a tilted lens [21]. Therefore, I partially compensate for the distortions by slightly tilting the 750-mm Fourier transforming lens in front of the camera in the modal decomposition setup.
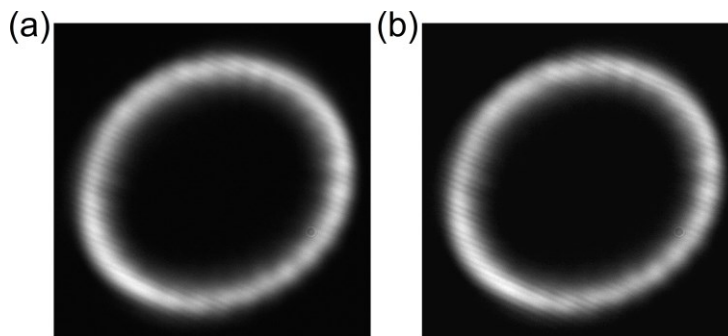
Figure 5.18: Intensity profiles of the transmitted signal beam at 0 dB (a) and 9.2 dB (b) gain. Images are normalized to maximum value and in linear scale.

Figure 5.19 shows the central region of ~2 mm×2 mm of the decomposed beam when the holograms corresponding to the field structure of OAMMs with charge l' from -11 to -19 and from 13 to 17 are displayed on the SLM in sequence. Background subtraction is also applied here. The brightness and contrast of the images is adjusted to enhance the visibility. For some charges, the displayed intensities are almost zero and hence the images are pitch black.
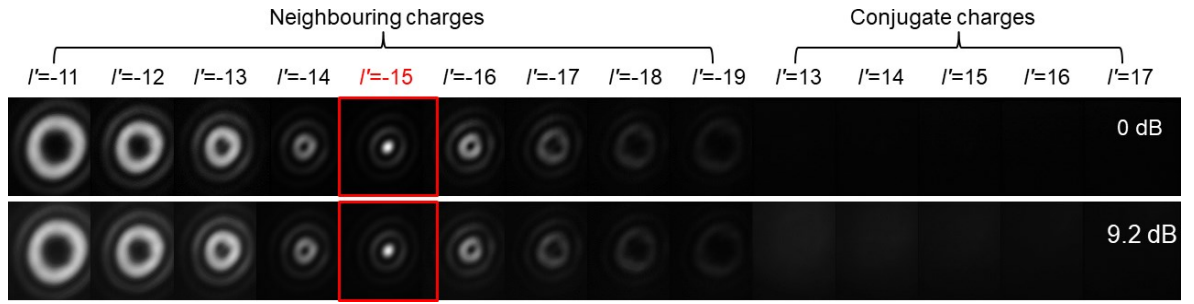
Figure 5.19: Signal beam decomposed into the selected neighbouring charges and conjugate charges at 0 dB and 9.2 dB (bottom row) gain.

The modal content of each mode in the transmitted and amplified signal, calculated as the ratio of its corresponding on-axis intensity to the sum of the on-axis intensities of all the modes, are shown in Figure 5.20. A back-to-back measurement shows that the beam incident to the RGF has a purity of ~98% for $l = 15$. The purity then drops to 84.3% for the transmitted signal beam without pumping and further decreases to 78.4% for the amplified signal at 9.2 dB gain with background subtraction.
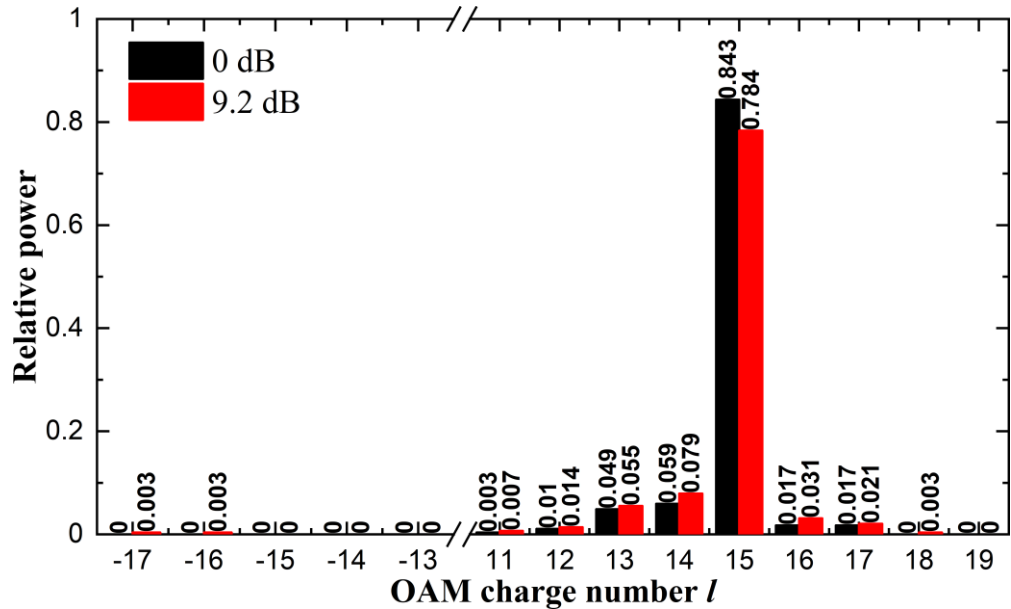
Figure 5.20: Fraction of power of the transmitted signal in different charges for 0 dB and 9.2 dB gain.

From Figure 5.20 we can see that when there is no pumping, power couples into the neighbour charges, mostly to $l = 14$. The power in $l = 16$ and $l = 17$ are almost the same. However, for the lower neighbouring charges, the parasitic power reduces as the charge separation from the target $l = 15$ increases. As the index separations between $l = 15$ and the neighbouring charges are almost 10^{-3}, coupling between these modes seems unlikely, especially in a circular pure silica core fibre with low perturbations. Instead, we tentatively attribute this to the imperfect OAMM excitation, namely the mismatch between the field distributions of the incident OAM beam and the OAMM in the fibre. In addition, the aberrations in the setup that causes the transmitted signal to be slightly elliptical may well have introduced distortions to the excited modes. For the amplified signal, the power in the unwanted modes follows a similar trend to the unamplified beam except for a slightly increased

power in $l = 16$. Unlike the previously reported results with lower charge OAMMs in section 5.2, the power in the conjugate charges is almost zero for the transmitted signal whether amplified or not. This is expected as the OAM charge difference is now much higher, and thus require an azimuthal perturbation of high order for direct coupling. Such perturbations are weak compared to lower-order perturbations. Gradual coupling via intermediate charges facilitated by perturbations of lower azimuthal orders is possible, but will also be weak.

In conclusion, we have experimentally demonstrated stable propagation and Raman amplification of an unpolarized (scalar) $l = 15$ OAMM at 1121 nm in a large core step-index fibre. The amplified signal only sees minor purity degradation from 84.3% to 78.4%. The fibre supports around $V^2/4 = 253$ scalar modes, so the power evaluated in the target mode is ~23 dB above the average power in all modes, and nearly 30 dB above the average power in non-targeted modes. With further optimizations to the mode excitation and the pumping wavelength, higher purity and higher Raman gain are expected. The results demonstrate great potential of FRAs for power scaling high charge OAMMs with excellent mode purity.

5.4 Summary

In this chapter I first reported a pulsed FRA for a charge 2 vector OAMM in a 5-m step-index fibre with a core of 25-μm diameter and 0.12 NA. A maximum of 15 dB average power gain is achieved, and the amplified signal reaches 4.5 kW of peak power and 68.5 μJ of pulse energy with multimode pumping of 6.95 kW peak power. There is no pump depletion induced gain roll-off and the pump to signal conversion efficiency reaches 17.9% at maximum gain. The conversion efficiency is limited by the achievable Raman gain before strong unseeded Stokes emerges. A brightness enhancement of ~8 dB from the launched pump to signal is estimated at 15 dB gain. The purity of the target OAMM in the transmitted signal is measured to 95.8% at 0 dB gain and 83.2% at 15 dB gain. The purity degradation is mainly attributed to the coupling between the target OAMM and its opposite charge as a result of their small effective index separation and difference in OAM. Then, a pulsed FRA for a charge 15 first radial order scalar OAMM in a 30-m step-index fibre with a pure silica core of 50-μm diameter and 0.23 NA is reported. With appropriate background subtraction, the amplified signal has a peak power of 5.41 W and pulse energy of 9.2 nJ with 9.2 dB average power gain. The transmitted signal has a target mode purity of 84.3% without amplification and 78.4% with 9.2 dB gain. The conversion efficiency from the pump to signal is not estimated here as the measured pump depletion is negligible, and is expected to be low due to the limited spatial overlap between the pump and signal. Contrary to the previous results, most of the purity degradation are introduced in the mode excitation process, and the dominant parasitic modes are the OAMMs with neighbouring lower charges ($l = 13$ and 14). Amplification induced purity drop is minor. By going to OAMMs with higher azimuthal orders, the coupling between the opposite charges is suppressed. The resistance to fibre bending is also greatly improved with only minor decrease in mode purity when the bending

radius of curvature is reduced to ~15 cm. Pressing and twisting the fibre still inflict degradation of mode purity, but with less effect on the charge-15 OAMM than on the charge-2 OAMM. In both amplifiers, the output power and the purity of the amplified signal remain stable in the short term and fluctuates by only a few percent in the long term as a result of the drifts in the alignment of the optics. Although our preliminary results are with a single high azimuthal order OAMM of the first radial order and relatively low in power, high power Raman amplification of a single or multiple OAMMs of either the first or higher radial order with high purity preservation can be possible in large core step-index solid core fibres. Also, multimode pump sources can be readily utilized to allow for brightness enhancement. The results of the $l = 2$ OAMM amplification support this. Therefore, FRAs for OAMMs with step-index fibres are a versatile alternative to the RE-amplifiers in ring-core fibres, especially in terms of power scaling and brightness enhancement with OAMMs.

5.5   References

[1]   D. V. Vysotsky, and A. P. Napartovich, "Mode competition in steady-state optical waveguide amplifiers," J. Exp. Theor. Phys. **108**, 547 (2009).

[2]   S. Stepanov, "Dynamic population gratings in rare-earth-doped optical fibres," J. Phys. D: Appl. Phys **41**, 224002 (2008).

[3]   M. Beresna, M. Gecevičius, P. G. Kazansky, and T. Gertus, "Radially polarized optical vortex converter created by femtosecond laser nanostructuring of glass," Appl. Phys. Lett. **98**, 201101 (2011).

[4]   P. C. Gregg, "*Optical angular momentum in air core fibers,*" PhD dissertation (Boston University, 2017).

[5]   J. W. Goodman, *Introduction to Fourier Optics* (W. H. Freeman, 2005).

[6]   B. M. Heffernan, R. D. Niederriter, M. E. Siemens, and J. T. Gopinath, "Tunable higher-order orbital angular momentum using polarization-maintaining fiber," Opt. Lett. **42**, 2683 (2017).

[7]   G. P. Agrawal, *Nonlinear Fiber Optics* (Elsevier Science & Technology, 2006).

[8]   S. A. Babin, D. V. Churkin, A. E. Ismagulov, S. I. Kablukov, and E. V. Podivilov, "Spectral broadening in Raman fiber lasers," Opt. Lett. **31**, 3007 (2006).

[9]   P. Gregg, P. Kristensen, and S. Ramachandran, "Conservation of orbital angular momentum in air-core optical fibers," Optica **2**, 267 (2015).

[10]   Z. Ma, and S. Ramachandran, "Propagation stability in optical fibers: role of path memory and angular momentum," Nanophotonics **10**, 209 (2020).

[11]   N. Bozinovic, Y. Yue, Y. Ren, M. Tur, P. Kristensen, H. Huang, A. E. Willner, and S. Ramachandran, "Terabit-scale orbital angular momentum mode division multiplexing in fibers," Science **340**, 1545 (2013).

[12]   J. Wang, J.-Y. Yang, I. M. Fazal, N. Ahmed, Y. Yan, H. Huang, Y. Ren, Y. Yue, S. Dolinar, M. Tur, and A. E. Willner, "Terabit free-space data transmission employing orbital angular momentum multiplexing," Nat. Photonics **6**, 488 (2012).

[13]   L. Zhu, G. Zhu, A. Wang, L. Wang, J. Ai, S. Chen, C. Du, J. Liu, S. Yu, and J. Wang, "18 km low-crosstalk OAM + WDM transmission with 224 individual channels enabled by a ring-core fiber with large high-order mode group separation," Opt. Lett. **43**, 1890 (2018).

[14]   J. Ma, F. Xia, S. Chen, S. Li, and J. Wang, "Amplification of 18 OAM modes in a ring-core erbium-doped fiber with low differential modal gain," Opt. Express **27**, 38087 (2019).

[15]   Q. Kang, P. Gregg, Y. Jung, E. L. Lim, S.-u. Alam, S. Ramachandran, and D. J. Richardson, "Amplification of 12 OAM Modes in an air-core erbium doped fiber," Opt. Express **23**, 28341 (2015).

[16]   Y. Deng, H. Zhang, H. Li, X. Tang, L. Xi, W. Zhang, and X. Zhang, "Erbium-doped amplification in circular photonic crystal fiber supporting orbital angular momentum modes," Appl. Opt. **56**, 1748 (2017).

[17]   Y. Jung, Q. Kang, R. Sidharthan, D. Ho, S. Yoo, P. Gregg, S. Ramachandran, S. Alam, and D. J. Richardson, "Optical orbital angular momentum amplifier based on an air-hole erbium-doped fiber," J. Lightwave Technol. **35**, 430 (2017).

[18]   A. Bjarklev, "Microdeformation losses of single-mode fibers with step-index profiles," J. Lightwave Technol. **4**, 341 (1986).

[19]   S. Pachava, A. Dixit, and B. Srinivasan, "Modal decomposition of Laguerre Gaussian beams with different radial orders using optical correlation technique," Opt. Express **27**, 13182 (2019).

[20]   V. Arrizón, U. Ruiz, R. Carrada, and L. A. González, "Pixelated phase computer holograms for the accurate encoding of scalar complex fields," J. Opt. Soc. Am. A **24**, 3500 (2007).

[21]   P. Vaity, J. Banerji, and R. P. Singh, "Measuring the topological charge of an optical vortex by using a tilted convex lens," Phys. Lett. A **377**, 1154 (2013).

Chapter 6   Summary and future work

6.1   Summary

This thesis presents my work on Raman amplification of HOMs and OAMMs in step-index fibres with multimode pumping. The research on single mode or multimode FRAs has been well established with the focus on wavelength agile power scaling in regimes like high power applications or telecommunications. The concept of using a particular HOM, either Bessel-like LP_{0m} modes or OAMMs, rather than the fundamental LP_{01} mode in a multimode fibre amplifier is more recent. Despite the plausible performance of the RE-doped fibre amplifiers for these HOMs, the idea of utilizing Raman gain for their power scaling and brightness enhancement remains largely unexplored. My work therefore focuses on the demonstration of the feasibility and advantages of FRAs for HOMs, especially on the mode purity preservation under gain compression.

I first present our investigations on the impact of gain saturation on the mode purity in FRAs and YDFAs via simulations. In the incoherent simulations, which is the case of FRAs presented in this thesis and most high power fibre amplifiers with multimode pumping, the FRA outperforms the YDFA in mode purity under gain saturation. This is a result of the much higher gain in the parasitic modes than in the target signal mode in the YDFA. In the coherent simulations, mode competition effects, where the strong modes suppress the co-polarized weak modes as they interfere, partly compensate for the purity degradation in YDFA. A dominant mode can suppress the growth of a weaker mode which is spatially coherent and has high intensity overlap with the dominant mode. As a result, the mode purity preservation of YDFA under gain saturation can outperform the FRAs in some cases. In practical fibre amplifiers where the modes are partly coherent, the performance is determined by the relative strength of the gain saturation effect between the incoherent modes and the competition effect between the coherent modes. For the amplifiers for OAMM however, the conjugate charges are always spatially coherent and perfectly overlapping with each other. The local gain saturation of Yb can therefore help to reduce the growth of the parasitic conjugate mode.

In Chapter 4, I demonstrate FRAs for Bessel HOM in large core fibres with multimode pumping in both pulsed and QCW regime. Firstly, an 18-dB average power Raman gain of LP_{08} mode in a 9-m step-index silica fibre with a core of 50 μm diameter and 0.2 NA is demonstrated with multimode pumping from a pulsed YDFA. The signal mode is preserved throughout the amplification with a maximum weighted pump depletion of 36.7% and the pump to signal brightness enhancement is estimated to ~14 dB. Then the results with an updated amplifier configuration aimed to resolve the shortcomings of the first FRA are presented. With an optimized multimode YDF MOPA based Raman pump source, in 10-m of step-index fibre with a pure silica core of 50 μm diameter and 0.23 NA, 25 dB Raman amplification of LP_{05} mode is achieved with 27% weighted pump depletion and

13 dB pump to signal brightness enhancement. Further optimization to the pulse shape and spectral linewidth of the Raman seed source enables over 23 dB Raman amplification of LP_{06} mode in a 335-m long 70-μm core diameter step index fibre. The signal mode is well preserved with a weighted pump depletion of 59% and suffers only moderate degradation with 77% weighted depletion. The pump to signal brightness enhancement is estimated to over 16 dB. The results support the usage of Raman amplification with pumps with even lower brightness including diode lasers by scaling the length of the gain fibre. Therefore, we attempt Raman amplification of a single LP_{06} mode in a ~870 m long step-index fibre with a pure silica core of 50 μm diameter and 0.23 NA with five spectrally combined QCW diode lasers. The maximum Raman gain is ~6 dB with no sign of degradation to the signal mode. Despite the relatively low Raman gain, the successful demonstration of stable HOM propagation in a large core step-index fibre with length of hundreds of meters and Raman amplification with spectrally combined diode laser pumping points towards significant brightness enhancement with direct diode laser pumped FRAs for HOM.

The experiments on Raman amplification of OAMMs in multimode step index fibres are introduced in Chapter 5. With multimode pumping from a pulsed YDFA, up to 15 dB average power gain of a $l = 2$ OAMM is achieved in 5-m of commercial few-mode step-index fibre with a core of 25-μm diameter and 0.12 NA. The purity of the launched OAMM receives only minor drop from 95.8% at 0 dB gain to 83.2% at 15 dB gain, which is mainly a result of coupling into the conjugate charge $l = -2$. Since the coupling between the conjugate charges are expected to decrease for OAMMs with higher charges, we attempt Raman amplification of a charge 15 OAMM of the first radial order in a 30-m step-index fibre with a pure silica core of 50 μm diameter and 0.23 NA. The maximum average power Raman gain after background subtraction is 9.2 dB. The signal mode purity is well maintained from 84.3% at 0 dB gain to 78.4% at 9.2 dB gain, with negligible power coupled into the conjugate charges. The purity drop is expected to arise from imperfect mode excitation and the aberrations in the setup and can be resolved with further optimizations. For the charge-2 OAMM, the FRA improve the brightness from pump to signal by ~8 dB. For the charge-15 OAMM, its power is nearly 23 dB higher than the average power in all the signal modes. These results demonstrate the capability of power scaling the OAMMs with Raman gain in highly multimode step-index fibres with good mode purity preservation and verify the improved stability of high charge OAMMs in large core step-index fibres.

6.2   Future work

The FRAs have been demonstrated as an attractive alternative to the RE-doped fibre amplifiers in power scaling and brightness enhancement with the HOMs, with most of the results in the pulsed regime owing to the high pump brightness requirement of the Raman gain. The preliminary results of QCW Raman amplification with spectrally combined diode laser pumping point towards imminent optimizations in the fibre length and Raman seed power to enhance the Raman gain and pump to

signal conversion. In the long term, improvements in the brightness of diode lasers allow higher gain per unit length of the gain fibre and may fully unlock the potential of power scaling of HOMs with FRAs. Additionally, the use of Raman gain fibres with enhanced Raman gain coefficient can improve the conversion efficiency of the amplifier and alleviate the brightness requirement of the pump source. The adoption of these fibres which are usually doped with germanium has been ubiquitous in high power fibre Raman amplifiers and lasers, at the expense of higher background loss. However, a practical concern is that the refractive index profiles of these fibres are difficult to control and excessive transverse and longitudinal fluctuations in the index profiles are usually inevitable. Distortions and scattering to the signal HOM have been observed in our attempts to excite and propagate clean and stable HOMs in germanium doped fibres. Advances in fibre fabrication techniques may resolve this issue in the long term. In the pulsed regime, the achievable gain is limited by the higher order Stokes. Since the gain is well below the threshold gain of 16 nepers, we have predicted that a spectrally purer Raman seed source is less affected. Optimizations to the pulse shape of the pump and signal pulse also help to suppress the higher order Stokes and improve the pump-to-signal conversion.

A more interesting direction is perhaps the fibre Raman laser operating with a single HOM. Er-doped fibre lasers operating with both the fundamental mode and the Bessel HOM at the same time have been reported [1, 2], in which the HOMs are converted by fibre gratings and guided in the inner cladding in addition to the fundamental mode in the smaller core. However, the intensity profile of the output beam is heavily distorted as a result of fibre perturbations. Similar configurations can be adopted by the FRA which utilizes gain fibres with much less perturbations. Alternatively, it may be possible to form a cavity with free-space feedback, although such cavities have not yet been fully explored and are not necessarily simple adaptations from the free-space resonators for Bessel beams [3, 4].

For the OAMMs, FRAs with large core step index fibres can be an attractive alternative to the RE-doped amplifiers with ring-core or air-core fibres thanks to their simple fibre design and pumping configuration. However, the impact of gain competition between the spatially coherent degenerate modes on the mode purity in RE-doped fibre amplifiers remains to be clarified. Further investigations are also required to ensure optimum excitations of the OAMMs and minimize coupling into the unwanted modes either in the neighbouring charges or the conjugate charges. It is also worthwhile to explore the performance of FRAs for high charge OAMMs of radial order higher than one and the amplification of several OAMMs simultaneously with multimode pumping.

Finally, it is attractive to convert the FRAs for HOMs into all-fibre configurations. There are fibre components for both the Bessel HOMs and the OAMMs that converts the fundamental mode into the target modes with high conversion efficiency. Raman gain fibres with matching parameters are also within the scope of in-house fabrication. The complexity of free-space launching can therefore

be avoided, and the environmental fluctuations can be greatly reduced, which allows the FRAs to become more industry-friendly.

6.3   References

[1]   S. Suzuki, A. Schülzgen, and N. Peyghambarian, "Single-mode fiber laser based on core-cladding mode conversion," Opt. Lett. **33**, 351 (2008).

[2]   D. Sáez-Rodriguez, J. L. Cruz, A. Díez, and M. V. Andrés, "Fiber laser with combined feedback of core and cladding modes assisted by an intracavity long-period grating," Opt. Lett. **36**, 1839 (2011).

[3]   A. N. Khilo, E. G. Katranji, and A. A. Ryzhevich, "Axicon-based Bessel resonator: analytical description and experiment," J. Opt. Soc. Am. A **18**, 1986 (2001).

[4]   C. L. Tsangaris, G. H. C. New, and J. Rogel-Salazar, "Unstable Bessel beam resonator," Opt. Commun. **223**, 233 (2003).

Appendix A List of publications

A.1 Journal publications

<u>**S. Zhu**</u>, Y. Feng, P. Barua, and J. Nilsson, "Efficient low-brightness-pumped Raman amplification of a single high-order Bessel mode in 335-m of 70-µm-diameter silica-core step-index fiber," Opt. Lett. **45**, 6018 (2020).

Y. Feng, P. G. Rojas Hernández, <u>**S. Zhu**</u>, J. Wang, Y. Feng, H. Lin, O. Nilsson, J. sun, and J. Nilsson, "Pump absorption, laser amplification, and effective length in double-clad ytterbium-doped fibers with small area ratio," Opt. Express **27**, 26821 (2019).

S. Pidishety, <u>**S. Zhu**</u>, Y. Feng, B. Srinivasan, and J. Nilsson, "Raman amplification of optical beam carrying orbital angular momentum in a multimode step-index fiber," Opt. Lett. **44**, 1658 (2019).

<u>**S. Zhu**</u>, S. Pidishety, Y. Feng, S. Hong, J. Demas, R. Sidharthan, S. Yoo, S. Ramachandran, B. Srinivasan, and J. Nilsson, "Multimode-pumped Raman amplification of a higher order mode in a large mode area fiber," Opt. Express **26**, 23295 (2018).

Y. Feng, B. M. Zhang, J. Zhao, <u>**S. Zhu**</u>, J. H. V. Price, and J. Nilsson, "Absorption Measurement Errors in Single-Mode Fibers Resulting from Re-Emission of Radiation," IEEE J. Quantum Electron. **53**, (2017).

A.2 Conference publications

<u>**S. Zhu**</u>, Y. Feng, and J. Nilsson, "Raman Amplification of a Single Higher-Order Mode in a 335-m-Long Fiber with a 70-µm-Diameter Step-Index Core," Laser Congress 2020 (ASSL), paper ATh1A.7

<u>**S. Zhu**</u>, S. Pachava, S. Pidishety, Y. Feng, B. Srinivasan, and J. Nilsson, "Raman Amplification of Charge-15 Orbital Angular Momentum Mode in a Large Core Step Index Fiber," Conference on Lasers and Electro-Optics 2020, paper SM1P.2.

Y. Feng, C. A. Codemard, P. Barua, H. Lin, <u>**S. Zhu**</u>, Y. Feng, S. Pidishety, S. Hong, J. K. Sahu, and J. Nilsson, "Time Response Characteristics of Photodarkening-Induced Loss in Yb-Doped Fiber Amplifier," in 2019 Conference on Lasers and Electro-Optics Europe and European Quantum Electronics Conference, OSA Technical Digest (Optical Society of America, 2019), paper cj_2_2.

Ł. Dziechciarczyk, Z. Huang, G. Demetriou, D. Cheng, S. Pidishety, Y. Feng, Y. Feng, G. Wang, H. Lin, <u>**S. Zhu**</u>, D. Lin, T. W. Hawkins, L. Dong, A. Kemp, J. Nilsson, and V. Savitski, "9 W average power, 150 kHz repetition rate diamond Raman laser at 1519 nm, pumped by a Yb fibre amplifier,"

in 2019 Conference on Lasers and Electro-Optics Europe and European Quantum Electronics Conference, OSA Technical Digest (Optical Society of America, 2019), paper ca_11_2.

S. Zhu, S. Pidishety, and J. Nilsson, "15-dB Raman Amplification of an Optical Orbital Angular Momentum Mode in a Step-Index Fiber," Laser Congress 2018 (ASSL), paper AW2A.4.

Y. Feng, **S. Zhu**, S. Hong, H. Lin, P. Barua, J. Sahu, and J. Nilsson, "Spatially Gain-Tailored Fiber Raman Laser Cladding-Pumped by Multimode Disk Laser at 1030 nm," Conference on Lasers and Electro-Optics 2018, paper JTh2A.109.

Z. Huang, S. Pidishety, T. W. Hawkins, Y. Feng, Y. Feng, **S. Zhu**, L. Dong, and J. Nilsson, "Low-birefringence 120 W Yb fiber amplifier producing linearly polarized pulses with 69-GHz linewidth at 1083 nm," in Laser Congress 2018 (ASSL), OSA Technical Digest (Optical Society of America, 2018), paper ATu1A.1.

S. Pidishety, **S. Zhu**, P. G. Kazansky, J. Nilsson, and B. Srinivasan, "Amplification of Orbital Angular Momentum Beam in a Fiber Raman Amplifier," Laser Congress 2017 (ASSL, LAC), paper JTh2A.6.

S. Zhu, S. Pidishety, Y. Feng, J. Demas, S. Ramachandran, B. Srinivasan, and J. Nilsson, "Multimode Raman Pumping for Power-Scaling of Large Area Higher Order Modes in Fiber Amplifiers," Laser Congress 2017 (ASSL, LAC), paper ATh4A.4.

B. M. Zhang, J. Zhao, Y. Feng, **S. Zhu**, J. H. V. Price, and J. Nilsson, "Fiber absorption measurement errors resulting from re-emission of radiation," Advanced Solid State Lasers 2015, paper AM5A.20.